PITHA 00/10

Juli 2000

The LEP Energy Spectrometer

Jan Prochnow

thesis-2000-026
15/07/2000

III. Physikalisches Institut, Technische Hochschule Aachen
52056 Aachen, Germany

PHYSIKALISCHE INSTITUTE
RWTH AACHEN
52056 AACHEN, GERMANY

The LEP Energy Spectrometer

von

Jan Prochnow

Diplomarbeit in Physik

vorgelegt der

Fakultät für Mathematik, Informatik und Naturwissenschaften
der Rheinisch-Westfälischen Technischen Hochschule Aachen

im
Mai 2000

angefertigt im

III. Physikalischen Institut A

bei

Prof. Dr. A. Böhm

Abstract

The energy of the circulating particles in the LEP storage ring is predicted by a model based on nuclear magnetic resonance (NMR) probes measuring the bending magnetic field. This model is calibrated by the method of resonant depolarisation. Since the latter technique is limited in energy range an independent method to confirm the NMR based model is applied. The spectrometer has been installed to determine the beam energy with a relative accuracy of 1×10^{-4}. It consists of a precisely calibrated bending magnet flanked by six beam position monitors. The beam energy is determined by measuring the deflection angle of the particles and the integrated bending field. In the 1999 LEP operation period the spectrometer was commissioned and the first energy measurements in the regime of $90\,\mathrm{GeV}$ were performed. A relative scatter of 1.5×10^{-4} was observed with no systematic deviation from the energy model. The scatter is expected to be reduced in the 2000 LEP run by minimising several systematic effects of the measurement procedure.

Die Energie der im LEP Speicherring zirkulierenden Teilchen wird aus der Messung des Ablenkfeldes mit Hilfe von Kernspinresonanz (KSR) Instrumenten bestimmt. Dieses KSR Modell wird durch die Methode der Resonanten Depolarisation kalibriert. Da Letztere nur einen Teil des LEP Energiebereichs abdeckt, wurde das Spektrometer als eine unabhängige Methode zur Überprüfung des Modells entwickelt. Es soll die Energie der Teilchen mit einer relativen Genauigkeit von 1×10^{-4} bestimmen. Das Spektrometer besteht aus einem exakt kalibriertem Ablenkmagneten und drei Strahl Positions Monitoren auf jeder Seite. Die Energie des Strahls wird aus der Messung des Ablenkwinkels der Teilchen und dem integralen Magnetfeld bestimmt. Während der LEP Operationsperiode 1999 wurde das Spektrometer in Betrieb genommen und die ersten Energiemessungen im Bereich von $90\,\mathrm{GeV}$ durchgeführt. Es wurde eine relative Streuung der Energien von 1.5×10^{-4} ohne systematische Abweichungen vom KSR Modell beobachtet. Durch die Minimierung systematischer Effekte bei der Messung wird eine Verringerung der Streuung während der LEP Operationsperiode 2000 erwartet.

Contents

Chapter 1

Preface

The contents of this thesis are based on the work I carried out as a diploma student between January 1999 and February 2000 in the LEP beam instrumentation group at CERN in Geneva. During my visit I participated in the energy calibration team and was involved in the final assembly of the LEP energy spectrometer. The subject of the thesis is based on the commissioning and data analysis of the spectrometer. I was supervised by Prof. Dr. A. Böhm at my home university (RWTH Aachen) and Dr. B. Dehning at CERN.

The *Large Electron Positron collider* (LEP) is presently used in the W-Boson energy region. To determine important physical parameters, the electron and positron beam energy should be known to a relative accuracy of 1×10^{-4}. At LEP I the high accuracy method of resonant depolarisation (RDP), based on determination of the electron spin precession frequency, was adopted. RDP was frequently performed and the results were interpolated in time, using a model based on nuclear magnetic resonant (NMR) probes measuring the bending field. As the level of transverse polarisation at LEP beyond beam energies of $60\,\mathrm{GeV}$ (LEP II) is lower than the minimum required by the RDP method, the NMR model is used for the energy estimation beyond $60\,\mathrm{GeV}$. This requires besides the interpolation in time an extrapolation in energy. The validity of the extrapolation is tested by measurements of the total bending field. Uncertainties arise from parts of the bending field which cannot be measured and might not be sampled correctly. To determine systematic errors of this measurement procedure an independent method based on the accurate knowledge of the field of one bending magnet, and the determination of the beam deflection angle was adopted. This LEP spectrometer determines the ratio between the LEP operating energy and an energy in the range accessible to RDP.

This project was suggested in September 1997. The first three beam position monitors (one “arm”) were installed for the 1998 LEP run, followed by a series of measurements on the field properties of the analysing magnet. In the beginning of 1999 the remaining parts were installed and, during the following run, the spectrometer was commissioned. The data analysis is still in progress.

1.1 The Synchrotron Storage Ring LEP

LEP is an e^+e^- storage ring with a circumference of 27 km [4]. In 1976 a study group was formed at CERN to investigate the feasibility of such a complex machine and in 1981 a final design was completed. The target for the beam energy of LEP I was to reach 60 GeV, with the option of increasing it up to 100 GeV for LEP II by adding super-conducting radio frequency accelerating cavities to the standard copper ones.
LEP is installed in a tunnel which lies on a plane tilted between 50 and 150 m underground, with an inclination of $1.42\,\%$ to the horizontal. This configuration was chosen in order to support the machine on a stable stratum of material. The beam trajectory is designed to have eight straight sections of about 600 m each and eight arcs of about 2800 m length, with an overall radius of 3096 m.
Four detectors were installed to measure the particles created by the e^+e^- collisions.
The first injection into the LEP collider took place on 14^{th} July 1989 and one month later the first collisions were observed. On the 20^{th} September the experiments acquired their first data.

In 1999, LEP was able to achieve a centre of mass energy of 202 GeV and the four detectors collected a record integrated luminosity of $228\,\mathrm{pb}^{-1}$ each.

1.2 Physics at LEP

Ignoring higher order corrections, the standard model [1] needs three input parameters to obtain predictive power: g (coupling of the SU(3) Boson W^1, W^2, W^3 to left handed fermions), $g\prime$ (coupling of the SU(1) Boson B to fermions) and $<\phi_o>$. However, only combinations of those parameters can be accessed by experiment. A common choice of values to specify the theory is $\alpha_{EM}(M_Z^2)$, G_F and M_Z. Measurements of these values provide the opportunity to predict other combinations of fundamental constants [3]:

$$M_W \;=\; \frac{1}{2} g <\phi_o> \quad and \quad sin^2\Theta_W \;=\; \frac{g^2}{g^2+g\prime^2}\,. \tag{1.1}$$

Those predictions are used in combination with other direct measurements as a test of the standard model and to study radiative corrections. Taking the top quark mass into account, the standard model predicts the W mass with an error of 26 MeV. Therefore the goal of LEP II is to measure M_W with a similar experimental error.

A precise measurement of the W mass is an important check of the standard model. Furthermore, comparison with radiative corrections gives information on the mass of the Higgs boson or potentially on the masses of yet undiscovered particles.

In June 1996 the LEP centre-of-mass energy reached the kinematic threshold for W-pair production (161 GeV). The mass of the W boson can be reconstructed from the four-momenta of the decay particles. Fig. 1.1 shows the invariant mass distribution for a W-pair decaying into two quarks, a lepton and a neutrino [2]. The advantage of e^+e^- compared to hadron colliders for these events is the precisely known centre-of-mass energy. Thus, strict energy and momentum conservation constraints can be applied to the event reconstruction, which results in a higher precision of the reconstructed W mass.

The broad and the narrow distribution in Fig. 1.1 correspond to the invariant mass of the W pair before and after application of a kinematic fit, a measure which is applied to the reconstructed particles.

Their measured momenta are modified in magnitude and direction within the experimental error until the constraints of momentum and energy conservation are the best fulfilled. To extract the W boson mass, the invariant mass distribution of Monte Carlo events is fitted to the distribution of data events.

The application of energy conservation presupposes the knowledge of the beam energy; in particular, uncertainties on the beam energy δE_{beam} result in errors δM_W on the W-mass estimation:

$$\frac{\delta M_W}{M_W} \approx \frac{\delta E_{beam}}{E_{beam}} \tag{1.2}$$

Furthermore the absolute beam energy sets the overall energy scale in the estimation of the W mass.

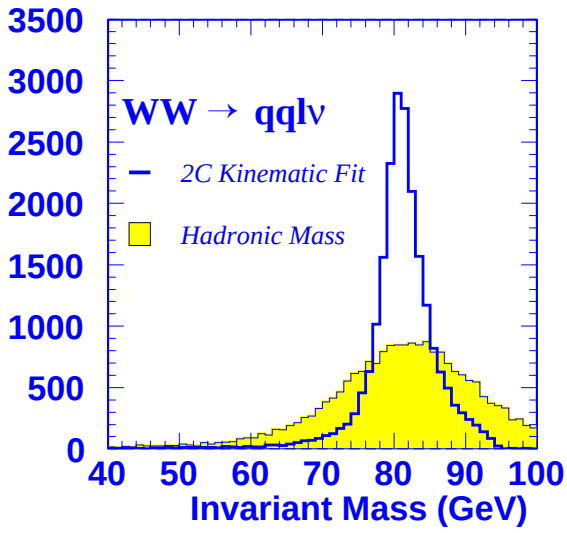

Figure 1.1: Estimation of the W Mass using a kinematic fit.

Chapter 2

Fundamental Concepts

2.1 Beam Energy

The beam energy E is related to the particle momentum p by the relativistic relation:

$$E^2 = (pc)^2 + (mc^2)^2 \,, \tag{2.1}$$

where m is the mass of the particles and c the speed of light.
For the ultra relativistic particles in LEP the approximation $pc \gg m_e c^2$ is valid:

$$E = pc \,. \tag{2.2}$$

As the Lorentz force provides the bending centripetal acceleration, the momentum $p(s)$ can be related to the local bending field $B(s)$ and local bending radius $\rho(s)$ as follows:

$$p(s) \;=\; qB(s)\rho(s) \tag{2.3}$$

where s is the curvilinear coordinate along the beam direction.
One condition for a closed orbit[1] is that the integral of the beam deflection $1/\rho$ along the path of the particles L is equal to $2\,\pi$:

$$\int_0^L \frac{qB(s)}{p(s)}\, ds \;=\; 2\pi \,. \tag{2.4}$$

Furthermore the revolution time must be a multiple of the accelerating voltage period. This means the orbit length L divided by the particle velocity (βc) must be equal to the wavelength of the accelerating frequency λ_{rf} divided by the speed of light c times an integer, called the harmonic number h (for LEP $h = 31320$):

$$L \;=\; \beta h \lambda_{rf} \;\simeq\; h\lambda_{rf} \,. \tag{2.5}$$

The momentum of the particle beam is determined directly by the transverse magnetic field $B(s)$ (Eq. 2.4) and the RF wavelength λ_{rf} (Eq. 2.5). The transverse magnetic field is in principle created by dipole magnets, but quadrupole as well as sextupole magnets have a vertical field component depending on the beam position. Thus, they contribute as well to the bending field if the beam passes through them off centre. Therefore a change of the orbit length L or the circumference of the accelerator C leads to a change in the magnetic field experienced in the quadrupole and

[1] The closed orbit is the self-consistent solution of the equation of motion with periodic constraints and represents the equilibrium path of the particles in a storage ring.

sextupole magnets, which according to Eq. 2.3 alters the particle momentum. Eq. 2.5 implies that a change in L can only be achieved by changing λ_{rf}. Variations of C can for example be caused by the earth tides [5]. The correlation between the lengths and the momentum variations is defined as the momentum compaction factor:

$$\alpha_c := (\frac{\Delta C/C}{\Delta p/p})_{|B=const.,\ L=const.} \tag{2.6}$$

To estimate the relative dependence of the momentum on the circumference C or orbit length L the ansatz:

$$p = q\rho_o B \left(\frac{C}{C_o}\right)^{\frac{1}{\alpha_c}} \tag{2.7}$$

is made using Eq. 2.5. The subscript o denotes the value for the nominal orbit[2]. The momentum compaction factor α_c can be evaluated from the Dispersion function $D(s)$ and the bending radius ρ [6].
The total differential of Eq. 2.7 is:

$$\frac{dp}{p} = \frac{1}{\alpha_c}\frac{dC}{C} + \frac{dB}{B}\ . \tag{2.8}$$

A variation of the particle momentum dp could be caused by a change in circumference dC of the machine or by a variation of the accelerating frequency df_{rf} which causes a change in orbit length L. Both changes result in an off centre beam in the quadrupoles, creating additional bending fields. For LEP the momentum compaction factor α_c is of the order of 10^{-4} (depending on the excitation of the quadrupole magnets). Therefore even small changes in the circumference or the accelerating frequency cause large momentum variations.

Since the particles lose energy in the bending sections and gain it in the radio frequency cavities, the beam energy is a function of the position in the ring. In Fig. 2.1 the residual ΔE to the mean energy is plotted against the position in the ring, showing the so-called energy sawtooth. To relate the mean beam energy measured by the RDP to the local beam energies at the interaction points of the experiments it is necessary to calculate the sawtooth. Therefore the energy loss due to radiation of synchrotron light in the arcs and the measured accelerating voltage have to be taken into account.

The energy sawtooth results in an orbit sawtooth, as according to Eq. A.6 the deflection angle in the dipoles is inversely proportional to the particle energy. This effect is described by the dispersion function $D(s)$. Particles with a momentum deviation Δp do not travel on the nominal momentum orbit, but at a radial position Δx to this orbit (dispersion orbit). The optic parameter dispersion $D(s)$ describes the ratio between the absolute distance to the nominal orbit and the relative momentum deviation for every position s around the ring:

$$\Delta x(s) \ = \ D(s)\ \frac{\Delta p(s)}{p}\ . \tag{2.9}$$

With Eq. 6.1 this results in:

$$\Delta x(s) \ = \ -\ D(s)\ \frac{1}{\alpha_c}\ \frac{\Delta f_{rf}}{f_{rf}}\ . \tag{2.10}$$

A displacement of the beam is caused by changes of the accelerating frequency Δf_{rf}.

[2]The nominal orbit is the closed orbit for an ideal machine without any alignment errors.

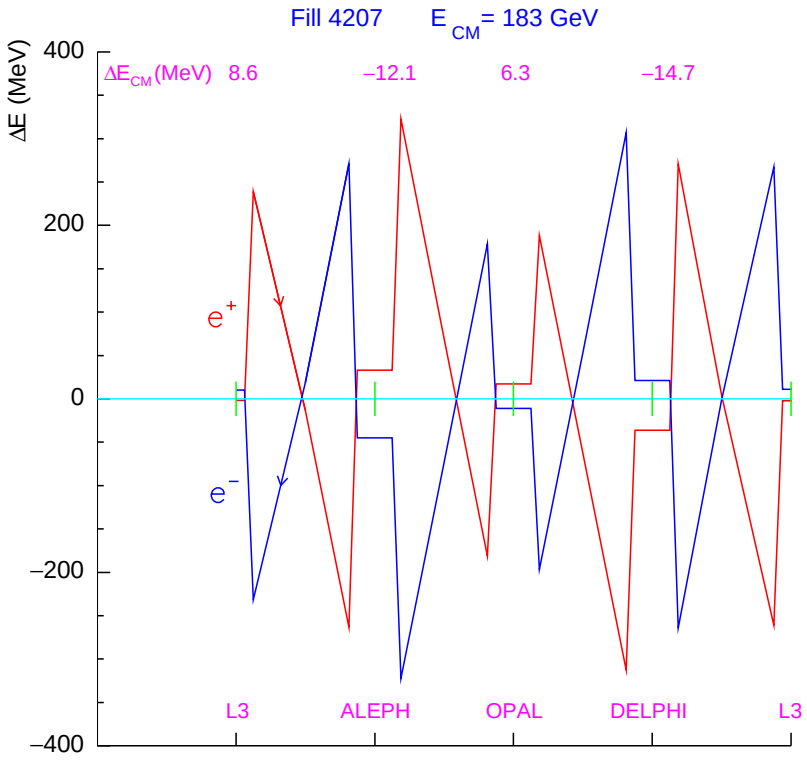

Figure 2.1: The energy deviation from the mean beam energy plotted against the position around the ring.

2.2 The Spectrometer

The concept of the spectrometer is based on the measurement of the bending angle of a particle beam passing through a magnetic dipole field. The beam energy is proportional to the integrated magnetic field and inversely proportional to the bend angle (see Appendix A):

$$E_{beam} = c\, q\, \frac{\int_{magnet} B\, dl}{\Theta}\ , \tag{2.11}$$

where c is the speed of light and q the charge of the particles.
The analysing magnet is part of the bending structure of LEP and thus its field increases during the acceleration of the particles in such a way that the bend angle Θ is almost constant. The angle is estimated by measuring the beam trajectories on both sides of the analysing magnet in the field free "arms" of the spectrometer using six capacitive beam position monitors (BPM).
The integrated magnetic field is derived from four nuclear magnetic resonance (NMR) probes placed inside the central field region of the analysing magnet. The calibration between the integrated field and the local field measurement of the NMRs was established during a mapping campaign (Sec. 5.1.1).

The spectrometer measures the changes in the beam energy during particle acceleration by determining the change of both the integrated field and the bend angle.
The principle of operation of the spectrometer is to estimate the beam energy with resonant depolarisation (RDP) (see Chap. 3.1.1) in the range between 41 and 60 GeV, then accelerate the beams and measure the increase of the energy with the spectrometer. This procedure of measuring only

the increase of the energy with the spectrometer reduces several systematic errors (see Sec. 6.3). The resulting energy is compared with the estimation of the energy based on the NMR model (Sec. 3.1.2) to determine any systematic differences.
The estimate of the low energy point (41 – 60 GeV) could instead be carried out using the energy model, which describes the energy in this regime with an uncertainty of 3 MeV [19]. The energy calibration with polarisation would then be replaced by the energy estimate of the model based on NMR probes. This procedure could be executed automatically and would take around 60 minutes, but the error on the low energy "point" would increase from 2 MeV (i.e. error on polarisation calibration) to 3 MeV.
Although the spectrometer is taking data throughout the run for commissioning, it is not meant to measure the energy during normal operation, as the machine is not sufficiently stable. In particular, regular variations of the accelerating frequency change the energy, the orbit position (Eq. 2.8) and the beam size (Sec. 6.2.1).
The spectrometer can be tested for energies between 41 and 60 GeV, as the absolute beam energy is well known in this regime. These procedures are sketched schematically in Fig. 2.2, where the beam energy is plotted against time. The difference between the magnetic field based energy determination procedure and the spectrometer is that the first is calibrated with the energy step between 41 and 60 GeV, whereas the latter allows an absolute comparison of the energies.

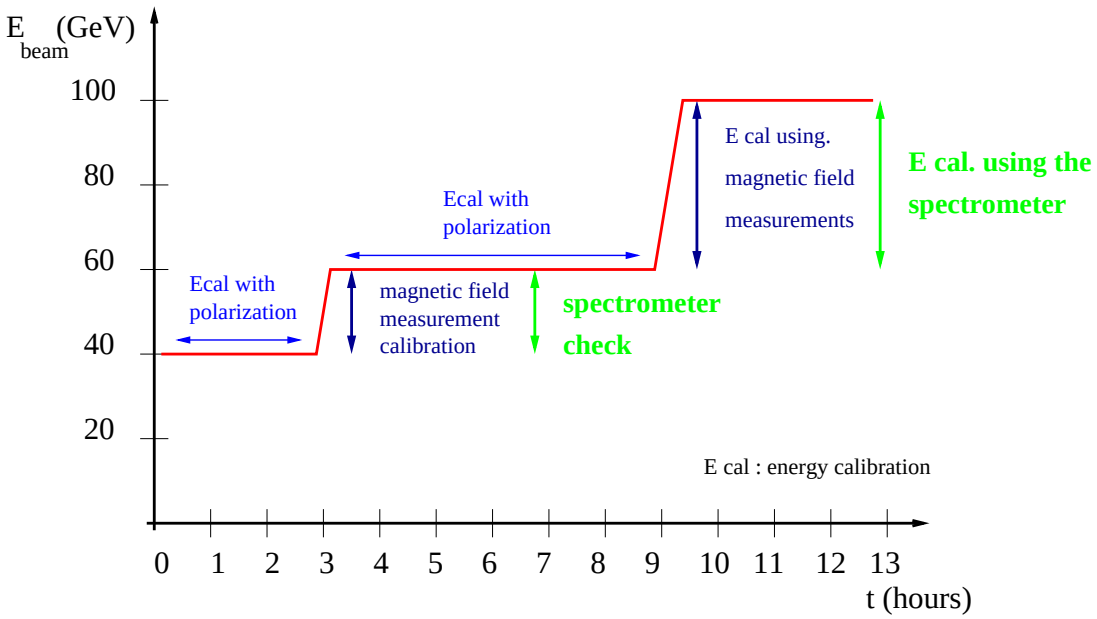

Figure 2.2: The procedure of the beam energy calibration at LEP.

2.2.1 Setup

In Fig. 2.3 the setup of the spectrometer is sketched as it was installed for the 1999 LEP run. The dipole magnet lies in the centre of the two arms and is equipped with six beam position monitors (BPM). Six BPMs instead of the minimum required three are used to measure the beam deflection angle. This is done for reasons of redundancy and also to enable calibration of the BPMs, as explained in Sec. 5.2. The BPMs are mounted on individual limestone blocks to reduce vibrations

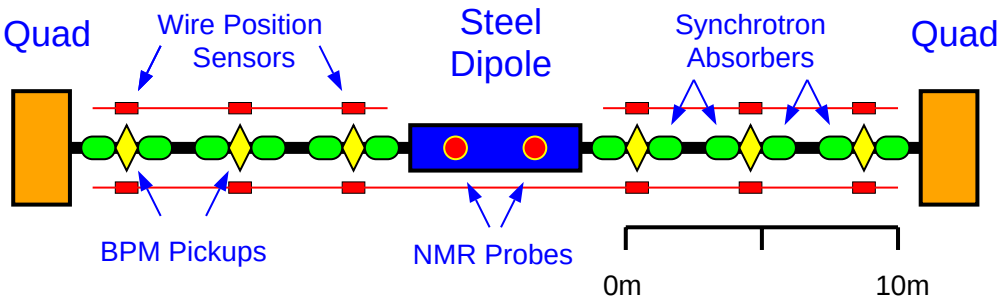

Figure 2.3: The layout of the Spectrometer.

and to make the measurements independent of each other (see Fig. 2.4). For avoiding unnoticed movements of the whole BPM blocks with respect to each other a system of wires with wire position sensors (WPS) attached to both sides of the BPMs was installed. The sensors determine movements of the BPMs with respect to the wire and thus with respect to each other. The position of the wire mounting is measured by WPS which are attached to the supporting limestone block. The LEP tunnel is a high radiation area (≈ 0.5 kW/m), so that the pick up electrodes of the BPMs have to be shielded against the synchrotron light and the photo-electrons it produces. This was achieved by using copper absorbers, which are elliptical tubes with an aperture smaller than that of the BPMs. As shown in Fig. 2.5, these absorbers are thermally and mechanically insulated from the monitors by bellows. Copper was chosen for the absorbers because of its high absorption coefficient for synchrotron light photons. To cope with the high energy deposition, which causes thermal variations, the BPMs are temperature regulated with an individual water cooling circuit. The location of the spectrometer in the transitions between arc and straight sections 425 m from IP3 has the following advantages:

- Sufficient field free drift space on both sides of a dipole magnet.
- Relatively short cable length to the location of the electronics in the pit.
- Almost equal beam energy of both particle beams.
- The disturbing effect of the so-called TGV current [20] is small in this region.

2.2.2 Tolerances and Requirements

The aim of the spectrometer is to determine the energy change from polarisation energies (41 – 60 GeV) to "physics" energies (≈ 100 GeV) with a relative accuracy of $\Delta E/E = 10^{-4}$; i.e. 10 MeV uncertainty for a beam energy of 100 GeV. As shown in Appendix D the errors on the angle and on the field are uncorrelated. The requirements can thus be derived from Eq. 2.11:

$$\left(\frac{\Delta E}{E}\right)^2 = \left(\frac{\Delta \int Bdl}{\int Bdl}\right)^2 + \left(\frac{\Delta \Theta}{\Theta}\right)^2 . \tag{2.12}$$

This means that the quadratic sum of the relative errors on the integrated B field and the angle must be lower than 10^{-4} squared. It was estimated that the error on the integrated magnetic field could be of the order of 3×10^{-5} [21]. This requires a precision on the angle estimation of 9.5×10^{-5}, which corresponds to an accuracy on the beam position measurement of $1\,\mu$m with the given lever

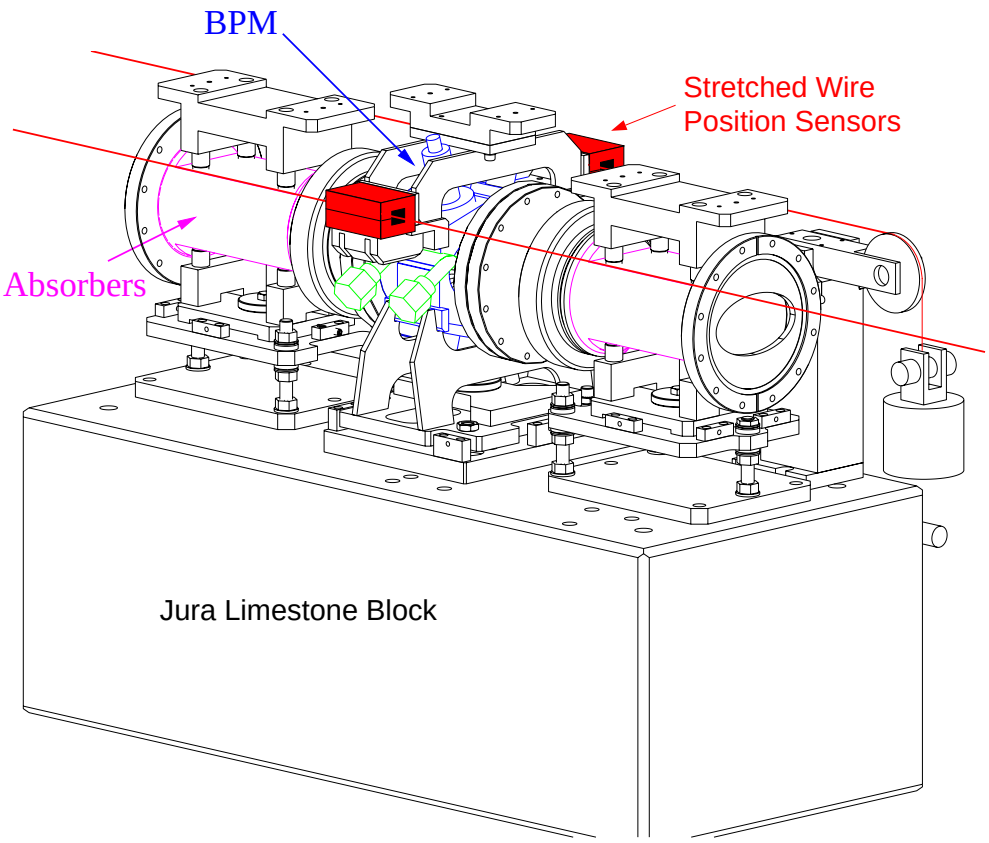

Figure 2.4: One of the six BPM station, consisting of the BPM, the supporting Jura block, the copper absorbers and the alignment wire system.

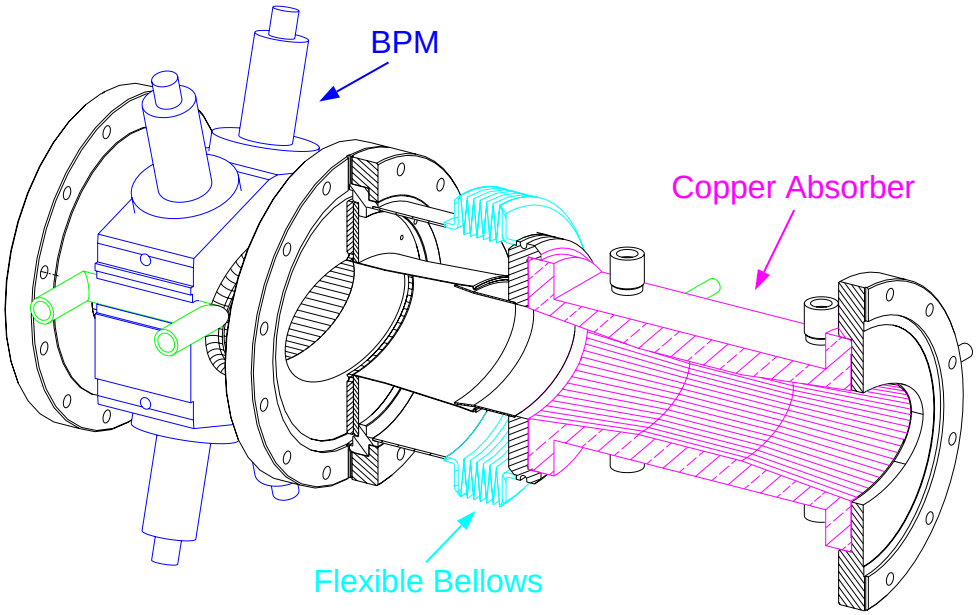

Figure 2.5: A BPM and its synchrotron light absorber.

arm of the spectrometer of twice $8\,\mathrm{m}$.
The beam energy at high energies E^h is determined according to the following equation, based on a known low energy E^l:

$$E^h \;=\; \left(\frac{E^h}{E^l}\right)^{(spectro)} \cdot \left(E^l\right)^{(pol),\,(NMR\ model)} \;, \tag{2.13}$$

where the superscript in brackets indicates whether the measurement was done employing the spectrometer or the polarimeter (NMR model).
Since only the ratio between the energies has to be determined by the spectrometer, the impact of systematic errors is reduced as described in Chapter 6.3.

2.3 Properties of Synchrotron Light

According to the theory of electrodynamics, accelerated charged particles radiate photons [7]. Since, in a storage ring, the particles are bent and thus accelerated towards the centre of the ring, they emit synchrotron light photons tangentially along the orbit in a narrow cone. The opening angle of this cone is:

$$\alpha/2 \;=\; 1/\gamma \quad ; \quad \gamma \;=\; \frac{E_{beam}}{m_e c^2} \;, \tag{2.14}$$

where E_{beam} is the particle or beam energy and m_e the electron mass (at $E_{beam} \;=\; 100\,\mathrm{GeV}$: $\alpha \;=\; 10.2\,\mu rad$).
The total radiated power beam current is given by:

$$P_{tot} \;=\; I_{beam}\,\frac{e}{3\,\epsilon_o}\,\frac{\gamma^4}{\rho} \;, \tag{2.15}$$

where ρ is the bending radius of the ring and I_{beam} the beam current.
The power of the synchrotron light and thus the energy loss rate of the particles scales with beam energy to the fourth power ($\propto\; E_{beam}^4 \cdot I_{beam}/\rho,\; I_{beam}$ being the beam current). In the LEP storage ring the e^+/e^- lose $2.9\,\mathrm{GeV}$ per revolution at $100\,\mathrm{GeV}$ beam energy, which is equivalent to a power deposition of $0.5\,\mathrm{kW}$ per meter along the accelerator, presuming a beam current of $5\,\mathrm{mA}$.

2.3.1 The Spectrum

The power is distributed over the photons according to their energy as follows [8]:

$$\frac{dP_{tot}}{dx} \;=\; P_{tot} \;\cdot\; S(x) \quad where \quad S(x) \;=\; \frac{9\sqrt{3}}{8\pi}\,x\,\int_x^\infty K_{\frac{5}{3}}(t)\,dt \;, \tag{2.16}$$

where $x = E_\gamma/E_c$ and $K_{5/3}(t)$ is the Bessel function of second kind of the order $5/3$. E_c is the so-called critical energy:

$$E_c \;=\; \frac{3}{2}\,\frac{\hbar\,c}{\rho}\,\gamma^3 \;, \tag{2.17}$$

which divides the spectrum into two parts of identical radiation power. Therefore the power per unit beam current is:

$$\frac{dP_{tot}}{dE_\gamma} \;=\; \frac{\sqrt{3}}{6\pi}\,\frac{e}{\hbar^2 c^2 \epsilon_o}\,\frac{E_\gamma \rho}{\gamma^2}\,\int_{\frac{E_\gamma}{E_c}}^\infty K_{\frac{5}{3}}(t)\,dt \;. \tag{2.18}$$

Dividing this equation by the energy of one photon E_γ and the circumference $2\pi\rho$ one obtains the number of photons per photon energy emitted per length of trajectory:

$$\frac{dN_\gamma}{dE_\gamma} \;=\; \frac{\sqrt{3}}{12\pi^2}\,\frac{e}{\hbar^2 c^2 \epsilon_o}\,\frac{1}{\gamma^2}\,\int_{\frac{E_\gamma}{E_c}}^{\infty} K_{\frac{5}{3}}(t)\;dt\;. \tag{2.19}$$

For $K_{5/3}(t)$ the following recurrence relation is valid:

$$K_{\frac{5}{3}}(x) \;=\; \frac{4}{3x}\,K_{\frac{2}{3}}(x) \;+\; K_{\frac{1}{3}}(x)\;. \tag{2.20}$$

Note : In the following calculations a typical beam current of 5 mA is assumed.

Therefore Eq. 2.19 results in :

$$\frac{dN_\gamma}{dE_\gamma} \;=\; \frac{5.5\;\times\;10^{13}}{(E_{beam}\,[GeV])^2\;(eV\,s\,m)}\,\int_x^{\infty}\left(\frac{4}{3t}\,K_{\frac{2}{3}}(t)\;+\;K_{\frac{1}{3}}(t)\right)\,dt\;, \tag{2.21}$$

where:

$$x = \frac{1.4\;\cdot\;E_\gamma\,[eV]}{(E_{beam}\,[GeV])^3}\;, \tag{2.22}$$

as the bending radius of the LEP dipole magnets is $\rho \;=\; 3096.175$ m [4].

The spectrum was computed by a FORTRAN program according to Eq. 2.21 and Eq. 2.22. The two Bessel functions $K_{2/3}$ and $K_{1/3}$ are available in the CERN program library MATHLIB (C340). The integration was done by the routine D103 from the same library, where the upper integration limit is the value of x, for which the integrand is lower that 10^{-10} of the value of the integral. The relative accuracy quoted for the integration routine is 10^{-11} [10]. The resulting spectrum emitted by LEP at 45 and 94 GeV beam energy is plotted in Fig. 2.7 (left plot). The upper photon energy limit is 1 MeV for a beam energy of 45 GeV and 10 MeV for 94 GeV beam energy. The integration over all energies results in a total number of photons of $1.7\;\times\;10^{14}\,(s\,cm^2)^{-1}$, which agrees with [11].

Depending on their energy, the photons have a certain probability for penetrating the vacuum chamber or being absorbed. The vacuum chamber consists of 8 mm of aluminium and 10 mm of lead shielding. The photons hit the vacuum chamber under a small angle ϵ ($\approx\;5.8$ mrad). To estimate the average length d the photons travel in the wall of the chamber, the following assumption was made: The incident photons get deflected via Compton scattering and this first process determines the angle, under which the photons pass the vacuum chamber wall. The synchrotron radiation is very strongly polarised in the plane of motion [7]; here $100\,\%$ polarisation is assumed. As sketched in Fig. 2.6 the incident photons set up oscillations of the target electron in the direction of the electric field $\vec{E}$. For the subsequent dipole radiation of the scattered photon, the angular distribution $\omega(\phi)$ is given by [7]:

$$\omega(\phi)\;\propto\;\sin^2\phi\;, \tag{2.23}$$

where ϕ is the angle between the dipole axis $\vec{n}$ and the direction of the emitted photon. The average angle according to Eq. 2.23 is:

$$\bar{\phi} \;=\; \frac{\int_0^{\frac{\pi}{2}}\;\phi\,\omega(\phi)\,d\phi}{\int_0^{\frac{\pi}{2}}\;\omega(\phi)\,d\phi} \;=\; \frac{\pi^2+4}{4\pi}\;. \tag{2.24}$$

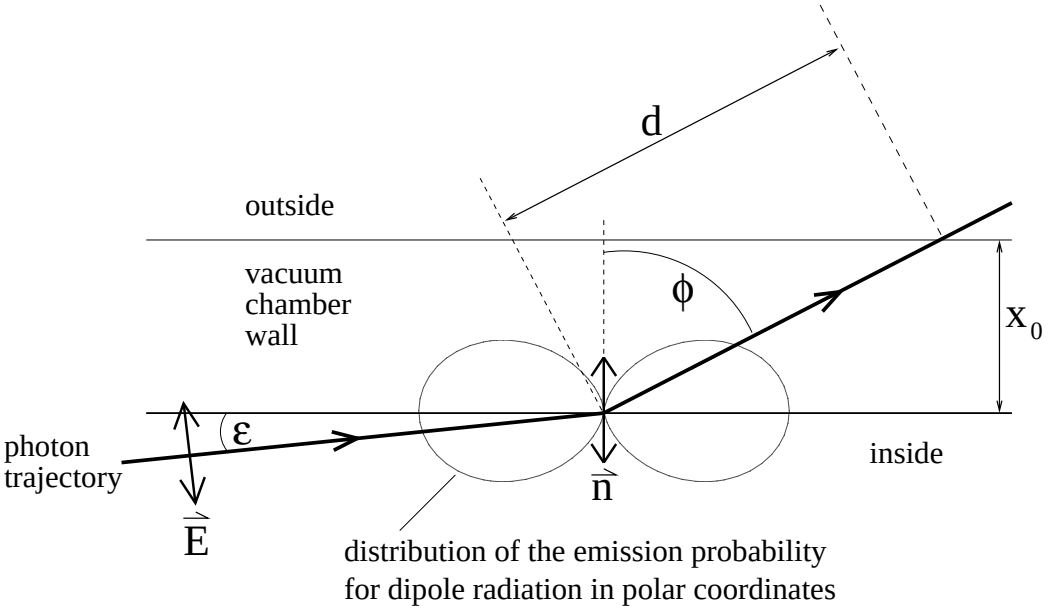

Figure 2.6: Compton scattering of an incident photon. The sketch is in the plane of motion.

Thus the photons penetrate the vacuum chamber wall with a mean angle of $\bar{\phi} = 63^{o}$. Therefore the mean distance d the photons travel inside the vacuum chamber wall is given by the following equation:

$$d \;=\; \frac{x_0}{\sin\left(\frac{\pi}{2} - \bar{\phi}\right)} \;=\; 2.2 \;\cdot\; x_0 \tag{2.25}$$

where x_0 is the wall thickness.
A beam of photons with an incident intensity I_i, penetrating a layer of material with mass thickness x and density ρ, emerges with intensity I_f given by the relation:

$$\frac{I_f}{I_i} \;=\; e^{-\frac{\mu}{\rho}x} \;. \tag{2.26}$$

The so-called mass attenuation coefficient μ/ρ as a function of energy for aluminium and lead was taken from a table [12]. The mass thickness x is defined as the mass per unit area, and is obtained by multiplying the thickness l with the mass density ρ.
According to Eq. 2.26 the differential number of photons penetrating the vacuum pipe can be calculated as follows:

$$\left(\frac{dN_\gamma}{dE_\gamma}\right)_f \;=\; \left(\frac{dN_\gamma}{dE_\gamma}\right)_i \;\cdot\; T \quad ; \quad T = \prod_{i=Al,\;Pb} e^{-(\frac{\mu}{\rho})_i x_i} \;. \tag{2.27}$$

The transmission coefficient T of the vacuum chamber is plotted in Fig. 2.8. This plot shows that the beam pipe absorbs almost all photons with an energy below 300 keV and reduces the number of photons beyond that energy by roughly $70 - 80\%$. These considerations result in a modification of the spectrum, which is plotted in Fig. 2.7 (right). The aluminium and lead of the vacuum chamber cut off the low energy part of the spectrum.

In this photon energy range and for the atomic number of the atoms in air (Z(N) = 7, Z(O) = 8) Compton scattering is the dominant process, followed by the photo electric effect [13].

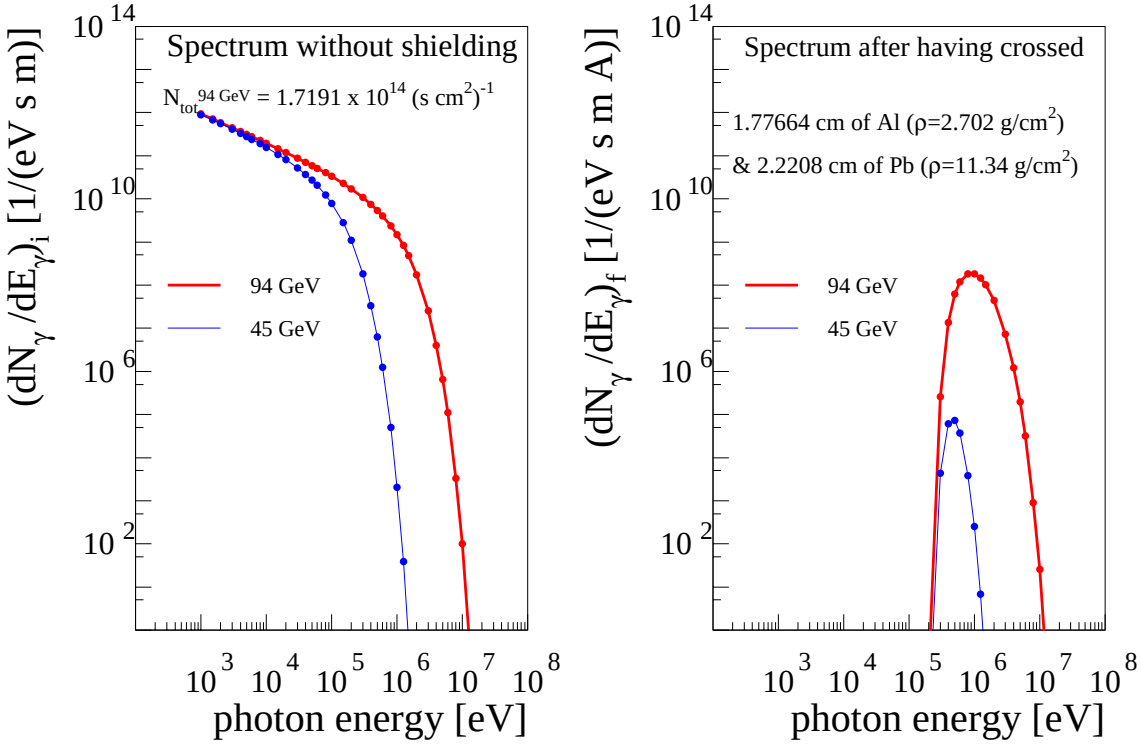

Figure 2.7: Left: The differential number of photons produced by a beam with a current of 5 mA and an energy of 45 respectively 94 GeV versus photon energy. Right: The spectrum of the photons which penetrate the beam pipe and the shielding.

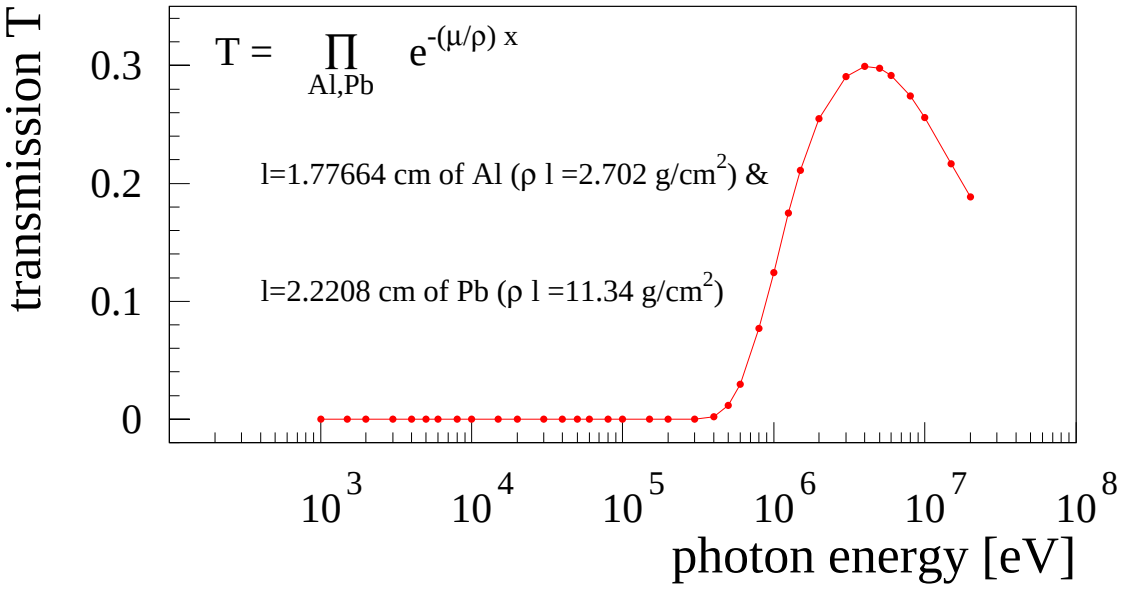

Figure 2.8: The transmission of the vacuum pipe for photons as a function of their energy.

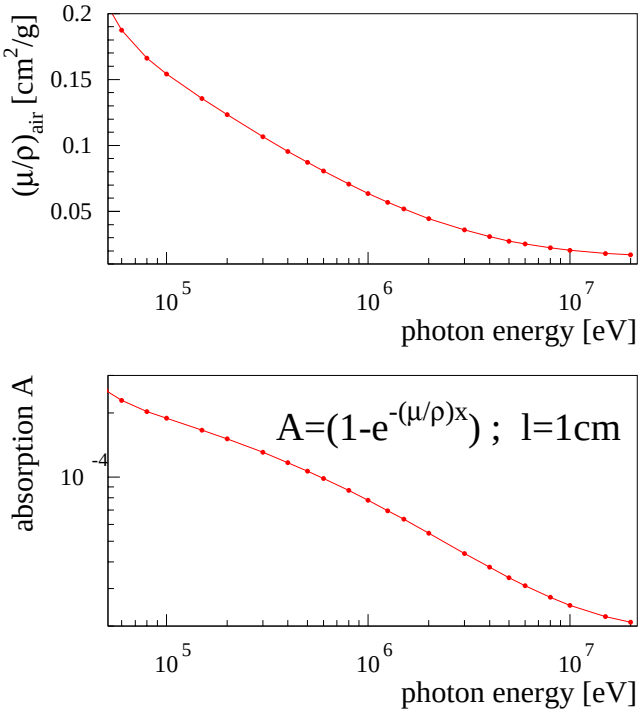

Figure 2.9: Top: Mass attenuation coefficient for photons in air versus photon energy. Bottom: Absorption coefficient in 1 cm of air versus photon energy.

The differential number of photons $(dN_\gamma/dE_\gamma)_f$ (see Eq. 2.27) times the absorption coefficient for photons in air results in the number of absorbed photons per incident photon energy. The energy loss E^{loss} per time and length of trajectory of the photons is equal to the number of absorbed photons times their energy. The latter value is approximated by the incident photon energy E_γ:

$$\frac{dE^{loss}}{dE_\gamma} = \left(\frac{dN_\gamma}{dE_\gamma}\right)_f \cdot A \cdot E_\gamma \quad ; \quad A = 1 - e^{-\left(\frac{\mu}{\rho}\right)_{air} x_{air}} , \tag{2.28}$$

where $(\mu/\rho)_{air}$ is the mass attenuation coefficient for air and x_{air} the mass thickness for 1 cm of air.
Fig. 2.9 shows the mass attenuation coefficient (top plot) and the absorption coefficient A for 1 cm of air (bottom plot) versus photon energy.

Integration of Eq. 2.28 over all photon energies results in the total power deposition of the synchrotron light in air per length of beam trajectory and per length of penetrated air: $E^{loss}_{94\,GeV} = 1.9 \times 10^{14}\,\mathrm{eV/(s\,cm^2)}$. As the function dE^{loss}/dE_γ which is plotted in Fig. 2.10 consists of a limited number of points, a sum was applied:

$$E^{loss} = \sum_i \left(\frac{dE^{loss}}{dE_\gamma}\right)^{(i)} \cdot (\Delta E_\gamma)^{(i)} . \tag{2.29}$$

$(\Delta E_\gamma)^{(i)}$ is estimated by the difference between the mean of the corresponding energy value and the adjacent values:

$$(\Delta E_\gamma)^{(i)} = \frac{E_\gamma^{(i)} + E_\gamma^{(i+1)}}{2} - \frac{E_\gamma^{(i)} - E_\gamma^{(i-1)}}{2} . \tag{2.30}$$

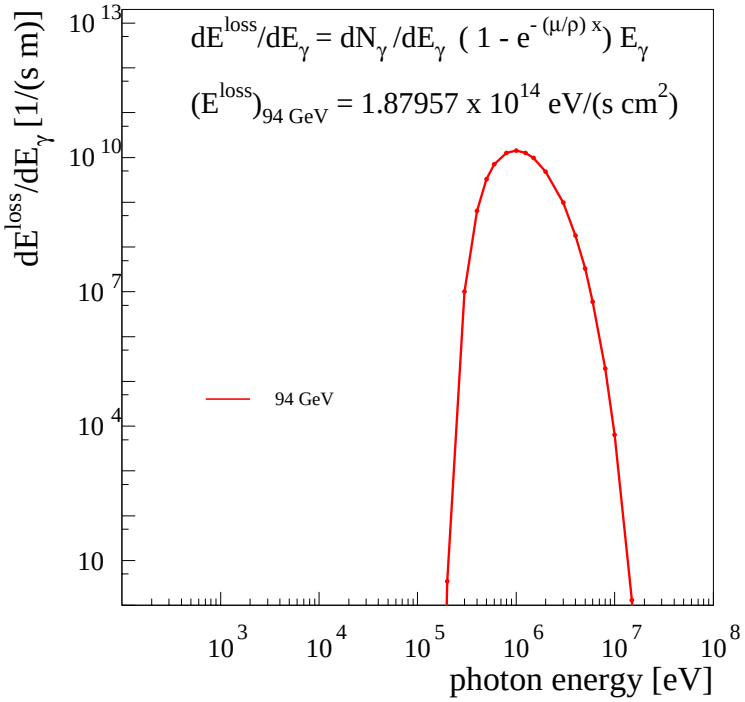

Figure 2.10: Energy loss per time and length along the trajectory against photon energy.

The power is assumed to be homogeneously distributed in a hollow cylinder with a length and wall thickness of $1\,$cm. To calculate the power density per volume, the result of the summation in Eq. 2.29 has to be divided by the circumference of the cylinder. To enable comparison with the results of Sec. 2.3.3, a radius of the cylinder of $5\,$cm is assumed, which results in a power deposition per volume of $E^{loss} = 6.0 \times 10^{12}\,\mathrm{eV/(s\,cm^3)}$.
To ionise an atom, the minimum required energy is its ionisation energy E_{ion}. As there are other mechanisms causing energy loss without creating ion pairs, the average energy lost by the incident particle per ion pair formed (so-called W-value) is always substantially greater than the ionisation energy (air: $E_{ion}(O) = 13.6\,\mathrm{eV/ion}$, $E_{ion}(N) = 14.5\,\mathrm{eV/ion}$ [12]; $W(air) = 33.8\,\mathrm{eV/ion}$ [17]). The W-value is in principle dependent on the type of radiation and its energy, however empirical observations show that it is not a strong function of either [17]. The number of ion pairs formed per volume and time can be obtained by dividing the total energy loss rate E^{loss} by the W-value of air: $N_{ion\ pairs} = 1.8 \times 10^{11}\,(\mathrm{s\,cm^3})^{-1}$; to translate this rate into a flux density, the absolute number of air molecules n_0 (Loschmidt's number) has to be taken into account:

$$n_0 = 2.69 \times 10^{19}\,cm^{-3}\,, \tag{2.31}$$

valid for an ideal gas at $0\,^o$C and nominal atmospheric pressure [18].
The resulting increase of the flux density is $6.7 \times 10^{-9}\,\mathrm{s^{-1}}$. Competing effects to this ion pair production are the recombination of the ions and the effect of an air flow in the tunnel blowing the ions away. To estimate an equilibrium concentration, those effects would have to be quantified.

2.3.2 Radiation Chemistry

Air consists mainly of N_2 (75.5 %) and O_2 (23.1 %). These molecules become ionised by the synchrotron radiation [14] :

$$O_2 \rightarrow O_2^+ + e \quad and \quad N_2 \rightarrow N_2^+ + e\,. \tag{2.32}$$

The N_2^+ will primarily exchange charges with oxygen molecules or be neutralised:

$$N_2^+ + O_2 \rightarrow N_2 + O_2^+ \quad or \quad N_2^+ + e \rightarrow N + N\,. \tag{2.33}$$

The O_2^+ ions are neutralised rapidly by creation of two reactive oxygen atoms:

$$O_2^+ + e \rightarrow O + O\,. \tag{2.34}$$

The high radiation yield [15] for the formation of ozone is explained by a further production of oxygen atoms via the processes:

$$N + O_2 \rightarrow NO + O \quad or \quad N + NO \rightarrow N_2 + O\,. \tag{2.35}$$

The final reaction for the oxygen atoms produced in the reactions 2.34 and 2.35 is then:

$$O + 2\,O_2 \rightarrow O_3 + O_2\,. \tag{2.36}$$

After a sufficient density of ozone and nitric oxide from reaction 2.35 and 2.36 is built up, they start to react with each other as follows:

$$NO + O_3 \rightarrow NO_2 + O_2\,. \tag{2.37}$$

Furthermore nitric dioxide is produced to a lesser extend in the reaction

$$2\,NO + O_2 \rightarrow 2\,NO_2\,. \tag{2.38}$$

The composition of the air is changed by the radiation present. For a beam current of 5 mA at an energy of 100 GeV the expected concentration of O_3 was estimated to be 6×10^{-10} and that of NO_2 to be 3×10^{-10} [14].

2.3.3 Measured Number of Ion Pairs

The basic unit of gamma-ray exposure is defined in terms of the charge dQ of either sign produced within a volume of air of mass dm. The exposure X is given by dQ/dm.
Measurements have shown that the absorbed dose in air corresponding to a gamma-ray exposure of $X_o = 1$ C/kg amounts to $D_o = 33.8$ J/kg$= 33.8$ Gy [17].
The radiation dose D at the spectrometer was measured by a chain of dosimeters wrapped around the beam pipe near the analysing magnet of the spectrometer. The left plot in Fig. 2.11 shows the numbering of the dosimeters. Fig. 2.11 (right) shows the absolute dose versus dosimeter number which was collected during 293.95 hours of high energy beam time. Thus the dose per unit time varies between 16 and 440 mGy/s around the beam pipe. The corresponding exposure is:

$$X = \frac{X_o}{D_o}\,D\,, \tag{2.39}$$

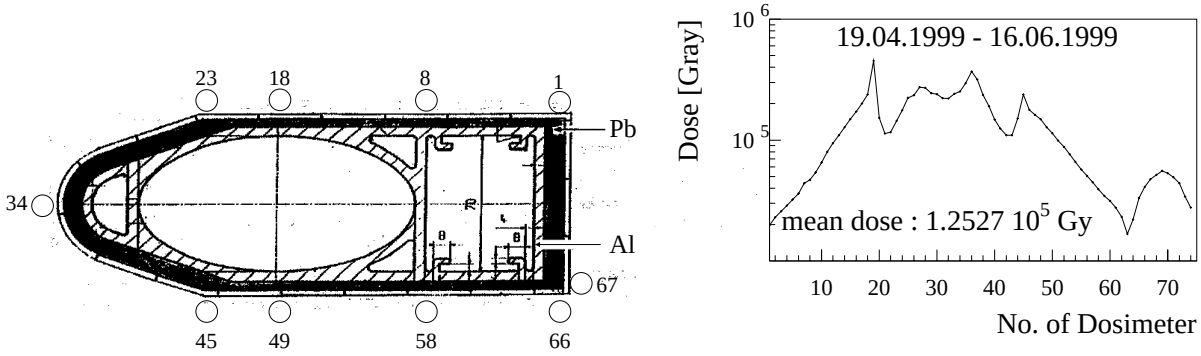

Figure 2.11: Left: The cross section of the LEP beam pipe with the position of the dosimeter. Right: The dose received in the period between 19.4.1999 – 16.06.1999 plotted against dosimeter number.

from which the number of ion pairs per volume and per time can be calculated:

$$N_{ion\ pairs} = \frac{X\,\rho_{air}}{2\,e} = \frac{X_o\,\rho_{air}\,D}{2\,D_o\,e}\,. \tag{2.40}$$

With the mass density $\rho_{air} = 1.205 \times 10^{-6}\,\mathrm{kg/cm^3}$ [12] and the electron charge magnitude e this results in a number of produced ion pairs between 1.8×10^9 and $4.9 \times 10^{10}\,(\mathrm{s\ cm^3})^{-1}$ with a mean value of $1.3 \times 10^{10}\,(\mathrm{s\ cm^3})^{-1}$.
The resulting mean ion pair concentration increase per time was calculated using Loschmidt's number to $4.8 \times 10^{-10}\,\mathrm{s^{-1}}$.

The discrepancy between this value and the results of Sec. 2.3.1 ($6.7 \times 10^{-9}\,\mathrm{s^{-1}}$) could be explained by the approximation implied in Eq. 2.28, where the actual energy of the photons after having crossed the vacuum chamber is identified with the incident photon energy. The actual energy of the photons in the air volume is smaller than their incident energy due to Compton scattering, so that the number of created ion pairs is overestimated.

Chapter 3

Energy Calibration at LEP

3.1 Techniques to estimate the Beam Energy

With the resonant depolarisation (RDP) method the mean beam energy can be estimated with high accuracy. To apply this method several accelerator parameters need settings other than those used during operation with colliding beams. Therefore it is not possible to perform continuous energy calibration parasitically during normal operation. The RDP method is limited to a maximum beam energy of $60\,\text{GeV}$. To have a continuous estimate of the beam energy with a high relative accuracy the magnetic bending field is sampled at several locations (described in Sec. 3.1.2). The systematic error of this method has been estimated in the past by using a different magnetic field based measurement method, the flux loop.

3.1.1 The Resonant Depolarisation Method

The RDP method is based on the measurement of the spin revolution frequency of the circulating particles.

The Spin Revolution

The spin is an internal degree of freedom. Its eigenstates are the solutions of the Dirac equation, where a spin operator describes the quantum mechanical phenomena. The Correspondence Principle of quantum mechanics states that the expectation value of quantum operators follows equivalent rules to a classical variable; therefore the spin can be treated as a classical vector $\vec{S}$. The Spin $\vec{S}$ of the electrons and positrons is linked to a magnetic moment $\vec{\mu}$:

$$\vec{\mu} = \frac{ge}{2m_e}\,\vec{S}\,, \tag{3.1}$$

where m_e is the electron mass, e the particle charge magnitude and g is the gyromagnetic ratio. In a storage ring the spins precess around the direction of the magnetic bending field $\vec{B}$. The fermions have a degree of freedom corresponding to the orientation of the spin with respect to the magnetic field ($\vec{S} \uparrow\uparrow \vec{B}$ or $\vec{S} \uparrow\downarrow \vec{B}$). A priori, both eigenstates have the same probability (unpolarised beam). According to the Sokolov-Ternov effect [22], the probability of a spin flip during emission of a photon (synchrotron light) depends on the initial spin direction parallel or anti-parallel to the bending field. This asymmetry leads to a transverse polarisation of the lepton beam.

The precession frequency is, according to [23]:

$$\omega_S \;=\; \omega_Z \;+\; \omega_{S'}\,, \tag{3.2}$$

where ω_Z is the particle revolution frequency (relativistic cyclotron frequency):

$$\omega_Z \;=\; \frac{eB}{m_e\gamma}\,, \tag{3.3}$$

and $\omega_{S'}$ the spin revolution frequency:

$$\omega_{S'} \;=\; \frac{eB}{m_e}\,\frac{g-2}{2}\,. \tag{3.4}$$

The spin tune ν is the number of precessions during one particle revolution around the ring and is hence equal to the ratio between $\omega_{S'}$ (Eq. 3.4) and ω_Z (Eq. 3.3).

With $\gamma = E_{beam}/(m\,c^2)$ the beam energy can be written as function of the spin tune:

$$E_{beam} \;=\; \frac{2}{g-2}\,m_e c^2\,\nu\,. \tag{3.5}$$

Therefore determination of the spin revolution frequency allows a measurement of the mean beam energy.

The polarisation vector $\vec{P}$ is defined as the average of all spin vectors $\vec{S}$ for a group of particles. The spin tune can only be measured, if the expectation value of $\vec{P}$ is different from zero (polarised beam). At LEP the time for the asymptotic build up of polarisation to $5\,\%$ at 45 GeV beam energy is 17 min. Unfortunately there are many effects which hinder the development of a measurable polarisation value. For example misaligned quadrupole magnets excite the beam every revolution and may cause depolarisation [24].

The Polarimeter

The degree of polarisation is measured by a Compton laser polarimeter: A circularly polarised laser beam is scattered against the electron beam of LEP. The cross section is a function of the polarisation level of both beams. Presuming that the polarisation of the light is constant, the angle of the backscattered photons is a measure of the electron beam polarisation level. To overcome systematic effects the light polarisation state is successively changed from right to left circular[1]. The polarisation level of the electrons is thus proportional to the shift of the distribution detected by a W-Si strip detector.

The spin tune is measured by reducing the polarisation resonantly through application of an oscillating horizontal magnetic RF field to the beam. This field interacts with the magnetic moment and thus rotates the spin slightly around a horizontal axis perpendicular to the beam. If the phase relation between the "kicking" RF field and the spin tune is constant, a coherent depolarisation of the beam results. By scanning the RF frequency in small frequency intervals and observing the polarisation level, the spin tune is directly determined when polarisation level changes are observed.

A minimum polarisation level of $3-5\,\%$ is required to detect unmistakably resonant depolarisations.

As the values of $(g-2)/2$, m_e and c in Eq. 3.5 are very well known and the spin tune ν is measured directly via the RF frequency of the kicker magnet the overall absolute accuracy of this procedure is $2\,\times\,10^{-5}$.

[1] This change is achieved by a rotating $\lambda/2$ and a fixed $\lambda/4$ plate.

Limitation of the Resonant Depolarisation Method

Unfortunately RDP is only feasible up to 60 GeV beam energy, because the level of spin polarisation is too low beyond that energy. In Fig. 3.1 the highest level of polarisation achieved is plotted against beam energy. This is in good agreement with the theory of transverse spin polarisation, which predicts a strong decrease of the polarisation level up to energies of 100 GeV and then an increase for energies beyond 100 GeV [25]. At 92 and 98 GeV measurements were performed twice during the 1999 run and show a polarisation level of $0 \pm 0.5 \times 10^{-3}$.

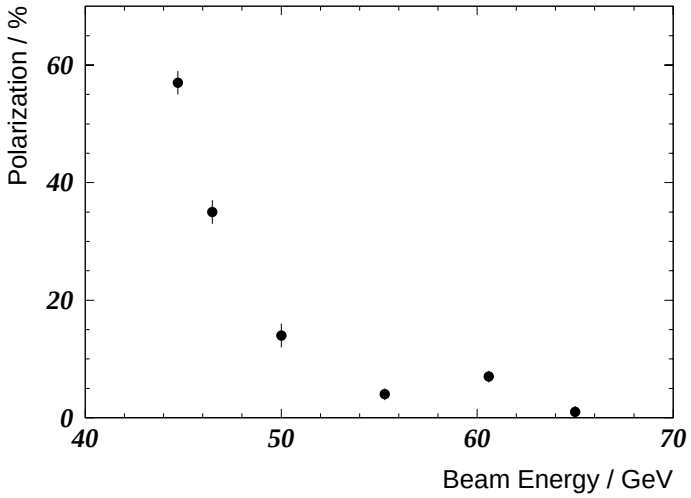

Figure 3.1: The maximum achieved polarisation level in LEP plotted against energy.

3.1.2 Nuclear magnetic Resonance Probes

The energy of a particle E_{beam} with charge e in a storage ring like LEP is proportional to the bending field B integrated along the ring l (see Appendix A):

$$E_{beam} = \frac{ec}{2\pi} \oint_l B ds \, . \tag{3.6}$$

To estimate the beam energy from measurements of the bending field 16 NMR probes determine the local field inside the LEP bending structure with a very high relative accuracy of $\approx 0.1\, ppm$ [26]. Their positions in the central region of the dipole magnets are sketched in Fig. 3.3. The probes are read out continuously. The relation between this local field measurement and the integrated magnetic field, and therefore the beam energy (Eq. 3.6), is assumed to be linear. This correlation can only be tested and parametrised in the energy range of $41 - 60$ GeV, because the NMRs operate only at energies above 41 GeV[2] and RDP is not feasible beyond 60 GeV. In Fig. 3.2 the difference between the energy estimated by the RDP E_{pol} and by the energy model E_{NMR} is plotted against E_{pol}. This residual shows a convex shape ("banana"). The systematic discrepancy of up to 2 MeV has been found to be reproducible over the last three years. The reason for this systematic deviation is not understood. The linearity might furthermore be affected by saturation effects in the end fields of the LEP dipole magnets at high energies, which could not be detected by the NMRs.

[2] A beam energy of 41 GeV corresponds to a bending field of 430 Gauss, which is the lowest field, the NMRs can measure.

The NMR probes suffer heavily from synchrotron radiation damage which makes it necessary to exchange them two or three times during a LEP operation period of five to six months.

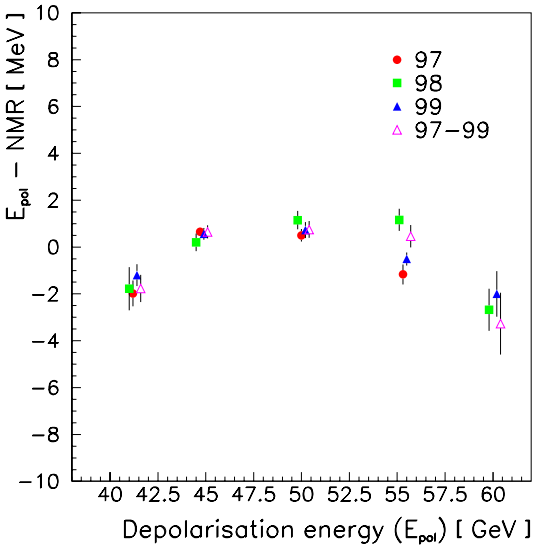

Figure 3.2: Deviation between the energy measurement by RDP and the prediction of the energy model based on the NMR probe measurement for the years 1997 – 1999.

3.1.3 The Flux Loop Measurement Setup

The flux loop consists of a wire loop including 95 % of the bending field. Its position in the dipole magnets is indicated in Fig. 3.3. The voltage U induced on the wire is proportional to the time derivative of the magnetic flux Φ penetrating the area of the loop:

$$U = -\frac{d\Phi}{dt} . \tag{3.7}$$

The magnetic flux is equal to the B-field component penetrating the loop perpendicular to its area multiplied by that area. As the shape of the loop is constant with time, the flux loop determines directly the first derivative of the integrated bending field in the dipole magnets while they are ramped. The integral of the induced voltage U over time is therefore proportional to the absolute change in the integrated field, which according to Eq. 3.6 is proportional to the increase in beam energy. A relative accuracy of several 10^{-4} is achieved. Flux loop experiments are only performed occasionally, without circulating beams in LEP, as they require a fast ramp of the magnets. The NMR probes are read out during these cycles and so a cross check between the linearity of the change in the local field (NMR) and the change of the bending field (flux loop) is performed.

Until 1998, the flux loop was the best available check of the agreement between the NMR readings and the integrated field. The relative discrepancy between these two methods is 2×10^{-4}. Unfortunately the device seems to suffer severely from the high radiation in LEP; for unknown reasons it appeared to work only sporadically in the 1999 run.

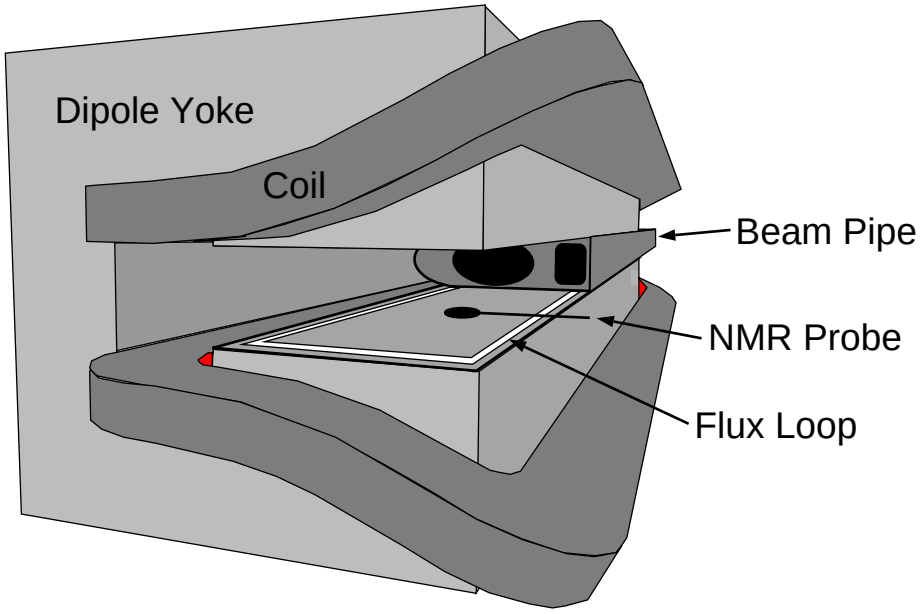

Figure 3.3: Position of the flux loop and the NMR probes in the dipole magnets of LEP

3.1.4 The Synchrotron Tune based Method

The synchrotron tune method is based on the measurement of the energy loss due to synchrotron radiation. As this energy loss increases with the fourth power of the energy, observables sensitive to the energy loss per turn can be used to determine the beam energy. The procedure, first used during the 1999 LEP running period [27], is to measure the Q_s value of the machine as a function of the integrated accelerating voltage.

The textbook formula [6] describing the correlation between beam energy E and accelerating voltage V_{RF} is:

$$Q_s^2 = \left(\frac{\alpha_c h}{2\pi E}\right)\sqrt{e^2 V_{RF}^2 - U_0^2}\ . \tag{3.8}$$

α_c is the momentum compaction factor and U_0 the energy loss due to synchrotron radiation; both are calculated by the simulation program MAD.

To apply the appropriate parametrisation of the Q_s versus V_{RF} dependence several modifications of Eq. 3.8 were made [27]. The top plot in Fig. 3.4 shows the resulting formula fitted to the data and the bottom plot the residual to this fit, which shows no systematic deviation. The actual beam energy results from the fit parameters. The overall error estimation for this method taking systematic and statistical errors into account sums up to 2.3×10^{-4} for energies of $90\,\text{GeV}$.

3.2 Principle of Combining the Measurements

The LEP mean beam energy model is based upon continuous NMR B-field measurements, the NMRs being calibrated against the RDP method. This model takes several effects into account which are not observed by the NMR probes. The mean beam energy is translated into individual energies at the locations of the four experiments by taking the energy loss due to synchrotron light and the voltage of the accelerating cavities into account.

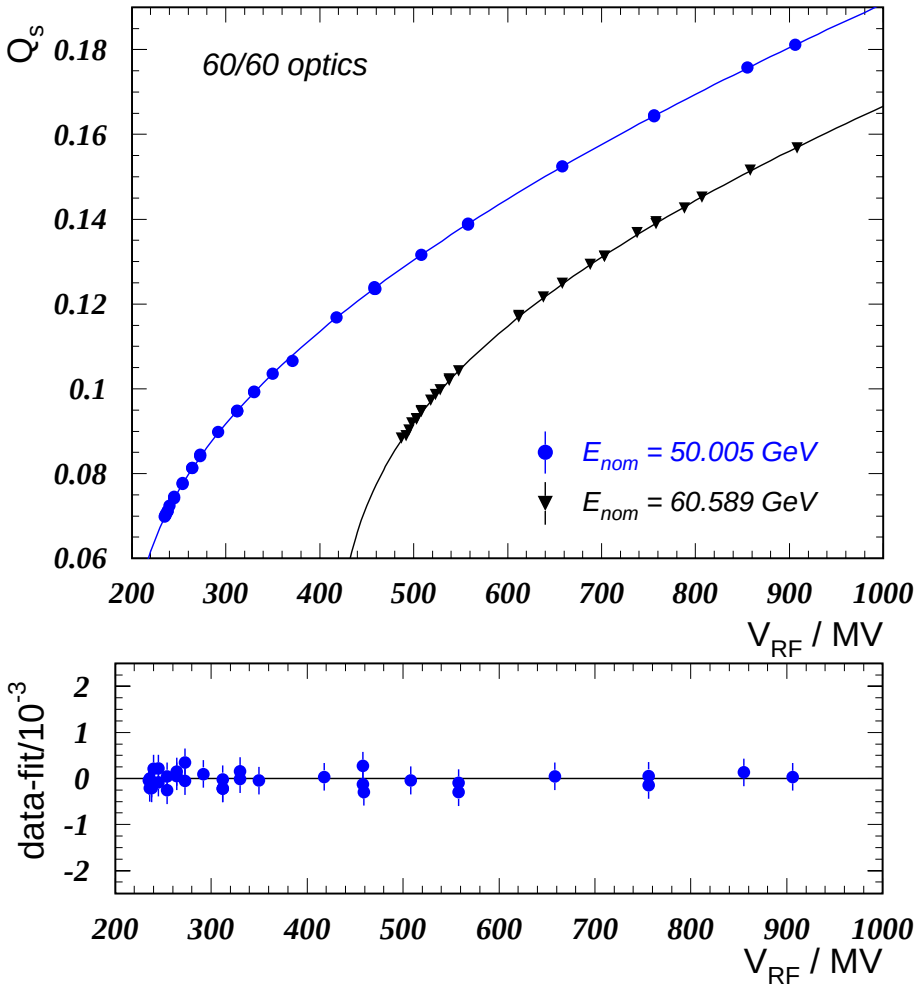

Figure 3.4: Top: Q_s versus total acceleration voltage. The points correspond to measurements, the lines represent the parametrisation. Bottom: The residuals to this fit do not show systematics.

The NMR probes as well as the flux loop take only the dipole magnet field into account and not the other fields of the LEP structure, which cause bending and therefore energy variations. A particle which passes a quadrupole magnet off centre encounters a dipole field and is thus deflected. Since the length of the orbit L is a constant, the particle has to alter its energy in order to fit the distorted machine. Earth tides, ground motions and variations of the RF accelerating frequency affect the orbit length and thus the energy (Eq. 3.6). Orbit correctors contribute as well to the integrated bending field. All these effects are taken into account for performing the calibration of the NMRs with the RDP method, as well as for the estimation of the centre-of-mass energy at the interaction points of the experiments.

3.3 Systematic Errors on the Overall Energy Estimation

Table 3.1 shows the evaluation of errors on the LEP2 beam energy not taking the spectrometer or the Q_s Method into account. Due to a lack of alternative methods, the difference between the energy estimation by the NMR and the flux loop is taken as the systematic error for the extrapolation of the energy. This error dominates the overall energy error. The latter is too large compared with the goal of 10 to 15 MeV. A better estimation and a minimisation of this extrapolation error is the goal of the spectrometer project.

Source	Error [MeV]		Correlation between
	1997	1998	1997 and 1998
Extrapolation from NMR–polarisation:			
NMR rms/$\sqrt{N}$ at physics energy	10	8	100%
Different Epol fills	5	4	0%
Flux-loop test of extrapolation:			
NMR flux-loop difference at physics energy	20	15	75%
Field not measured by flux loop	5	5	100%
Polarisation systematic	1	1	100%
e^+e^- energy difference	2	2	100%
Optics difference	4	6	50%
Corrector effects	3	4	50%
Tide	1	1	100%
Initial dipole energy	2	1	0%
Dipole rise modelling	1	1	100%
IP specific corrections ($\delta E_{CM}/2$):			
RF model	4	4	100%
Dispersion	2	2	100%
Total	25	20	

Table 3.1: Table of errors for 1997 and 1998, including the correlation coefficients between the two years at the beam energy of 92 and 96 GeV respectively.

Chapter 4

Setup of the Spectrometer

4.1 The Spectrometer Magnet

Two standard LEP concrete-steel dipoles were replaced with a double strength, custom made steel dipole (MBI) to be used as the analysing magnet of the spectrometer. The standard dipoles show ageing effects and have an unacceptable temperature dependence. Furthermore the MBI with its 5.75 m length is 5.50 m shorter than the standard dipole magnets. This allows a longer lever arm for the angle measurement. The MBI has a C-shaped core. Its yoke is built from 1.5 mm thick laminations of low carbon steel stacked between two 30 mm thick end plates. Two racetrack shaped coils surround the higher and lower pole of the magnet. To predict its integrated magnetic field at different energies the magnet contains four NMR probes provided by Metrolab [26]. Two probes operate in a range of the magnetic field which corresponds to $20-60$ GeV, the other two between $41-118$ GeV. Changes in the environmental conditions (such as humidity and temperature) can change the magnetic field. Those changes are observed by the probes and lead to a change of the predicted integral field at a given current supplied to the dipole magnet. This is only the case for environmental changes which affect the magnet uniformly. The amount of dissipated heat increases nonlinearly with beam energy, as the relevant effects are the Joule effect from the current I flowing in the magnet coil ($\propto I^2 \propto E_{beam}^2$) and the energy deposition due to synchrotron radiation ($\propto I_{beam} \cdot E_{beam}^4$), where I_{beam} is the beam current.

The core of the magnet is stabilised to $\pm\ 0.5^o$C by a regulated water cooling and heating system.

4.2 Beam Position Monitors

4.2.1 Layout

To determine the trajectories of the beam in the spectrometer, six standard LEP beam orbit monitors (BPM)(see Fig. 4.1) are used. 500 BPMs are installed in LEP, one next to each quadrupole magnet for determination of the orbit location. For this purpose the required accuracy is only $50\,\mu$m. The BPMs used for the spectrometer are equipped with more sophisticated electronics custom designed by Bergoz [28]. They are based on a design for synchrotron light sources, where beam position measurements with sub micron resolution were achieved [29]. Those electronics are sketched in Fig. 4.5 and explained in the following chapter.

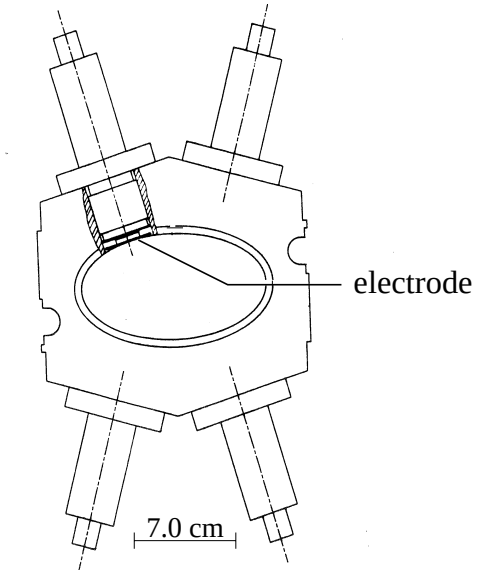

Figure 4.1: Cross section of a LEP beam position monitor.

4.2.2 Principle of Operation

As the charged particles of the beam travel through the beam pipe, they induce a charge on the inner surface of the vacuum chamber. The size of this charge is proportional to the electric field near the surface of the beam pipe [7]. As the magnitude of the electric field $\vec{E}$ is correlated with the distance r from the charge, the size of the induced charge at a given point is a measure of the distance to the beam. The BPMs pick up the induced charge with 4 electrodes arranged around the pipe as shown in Fig. 4.1.
The elliptical beam pipe makes the calculation of the expected beam position from a given signal rather complicated. The field inside a cylindrical conducting beam pipe with radius R containing a line charge $(+q)$ at a distance x from the centre can be constructed: This field is equal to the field produced by two line charges, one $(+q)$ at the position x, the other $(-q)$ at the position R^2/x [30] (see Fig 4.2). The charge S_P induced on the beam pipe at a point P is proportional to the superposition of the two fields produced by the charges $+q$ and $-q$. Thus S_P is proportional to the sum of the field components perpendicular to the conducting surface. According to [31] this approach results in:

$$S_P \propto \frac{q}{R} \, \frac{R^2 - x^2}{R^2 + x^2 - 2Rx\cos\left(\phi - \Theta\right)} \, . \tag{4.1}$$

Θ and ϕ are defined in Fig 4.2.

The BPMs used in the spectrometer have an elliptical cross section (major axis: 131 mm ; minor axis: 70 mm). In this situation, one image charge is not sufficient to fulfil the boundary condition for the electric potential Φ on the conductive surface: $\Phi_{|surface} = constant$. To calculate the induced signal, one has to find the position and size of an infinite number of image charges. Therefore the given arrangement is parametrised in a complex plane and then transformed into another complex plane, in which the arrangement is such that the positions of the image charges can be found. Applying the inverse of the mapping procedure to the position of the image charges, provides their position in the given arrangement.

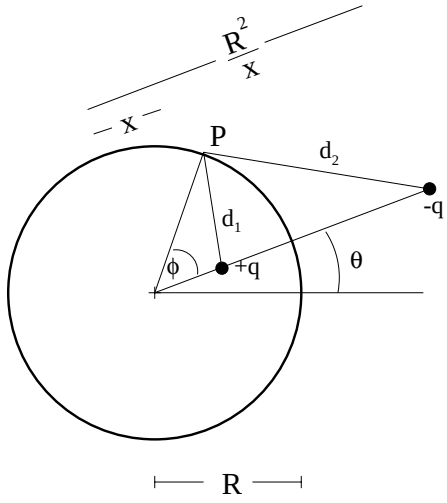

Figure 4.2: Arrangement of an image charge to fulfil the condition that the conducting surface of the pipe is an equipotential for the case of a round beam pipe.

As schematically shown in Fig. 4.3,

$$W = arcsine(\frac{Z}{k}) \tag{4.2}$$

transforms the beam pipe and the charge in the Z plane into a plate capacitor with a charge between the plates in the W-plane. For the latter case the infinite number of image charges can be found presuming that the plates of the capacitor are infinitely large (see Appendix E). This assumption is reasonable, as we are only interested in a centred beam (centre in the ellipse corresponds to the centre of the capacitor). As the beam at the spectrometer has a typical transverse size between

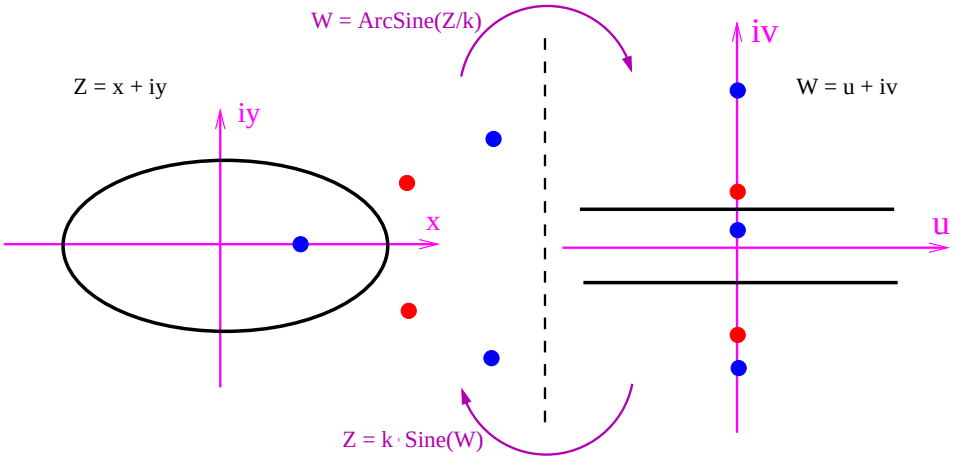

Figure 4.3: Procedure of finding the field inside a pickup introduced by a charge employing conformal mapping.

0.1 and 0.2 mm vertically and between 1 and 2 mm in the horizontal plane, the beam cannot be assumed to be a line charge, but a bunch of line charges with a Gaussian distribution in space.
A FORTRAN routine [32] was compiled to simulate the BPM signals by calculating the magnitude

of the field at the electrodes. The first 20 generations of image charges were taken into account. The result of such a calculation showing only the first generation image charges can be seen in Fig. 4.4. The Gaussian distribution of the line charges was simulated using a random number generator. The program was extremely useful to estimate the effect of the beam size on the position measurement as described later.

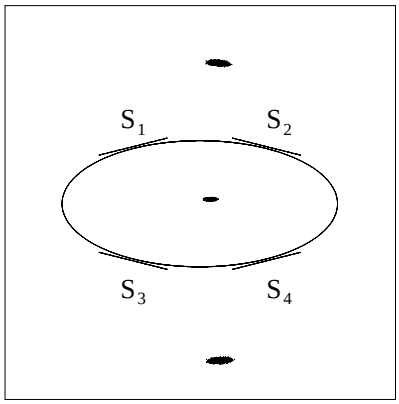

Figure 4.4: Beam inside the LEP vacuum chamber and the first two orders of image charges to reconstruct the output of the BPMs.

The electronics employed for measuring the beam position are sketched in Fig. 4.5. The four electrodes of the BPMs are read out one after the other with a switching frequency of 400 Hz and an integration time of 0.01 sec by means of GaAs switches. In this way it is possible to read out all electrodes with the same amplifier avoiding different biases for different electrodes. The multiplexing of the signals precludes single bunch observation. From the raw button signals S_i the x and y position are calculated as follows:

$$X_{out} \propto \frac{(S_2 - S_3) - (S_1 - S_4)}{(S_1 + S_2 + S_3 + S_4)} , \qquad Y_{out} \propto \frac{(S_2 - S_3) + (S_1 - S_4)}{(S_1 + S_2 + S_3 + S_4)} . \tag{4.3}$$

$(S_2 - S_3)$ corresponds to the component of the beam position along an axis having its origin in the centre of the pick up pointing at button 2. Analogously $(S_1 - S_4)$ corresponds to the component of the position vector directed towards button 1. Thus the difference $(S_2 - S_3) - (S_1 - S_4)$ is proportional to the x-component of the beam position measured from the centre. The signals are divided by the sum of all button signals to be, to first order, insensitive to common signal intensity and gain variations ($S_i \rightarrow cS_i$).
For analysis the signals from the individual electrodes S_i and the automatic gain control (AGC) are available.

The LEP current decreases by $50\,\mu$A per hour during a polarisation measurement, where the beams are not colliding (see Fig. 4.6, top). For comfortable operation it is necessary to have BPM electronics which provide a position measurement which is independent of the beam current. The Bergoz electronics achieve this by the normalisation with the sum of all button signals and by using a technique called automatic gain control (AGC). The latter compensates remaining variations of the position measurement due to beam current changes. The idea is to vary the gain in such a way

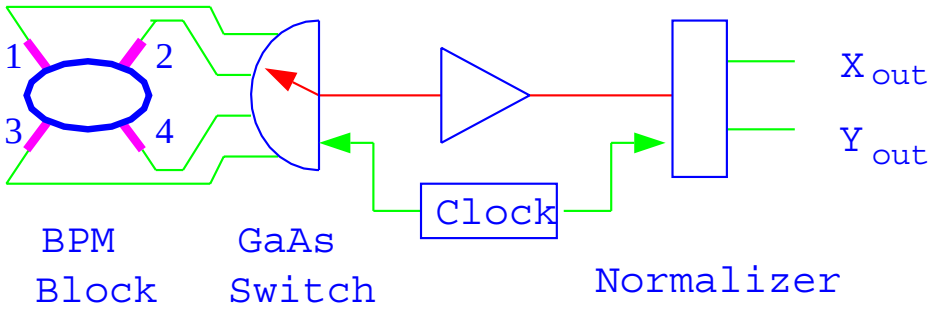

Figure 4.5: Schematic drawing of the beam position monitor electronics.

that the sum of the signals from the four electrodes of one BPM stays constant with time (Fig. 4.6, bottom).

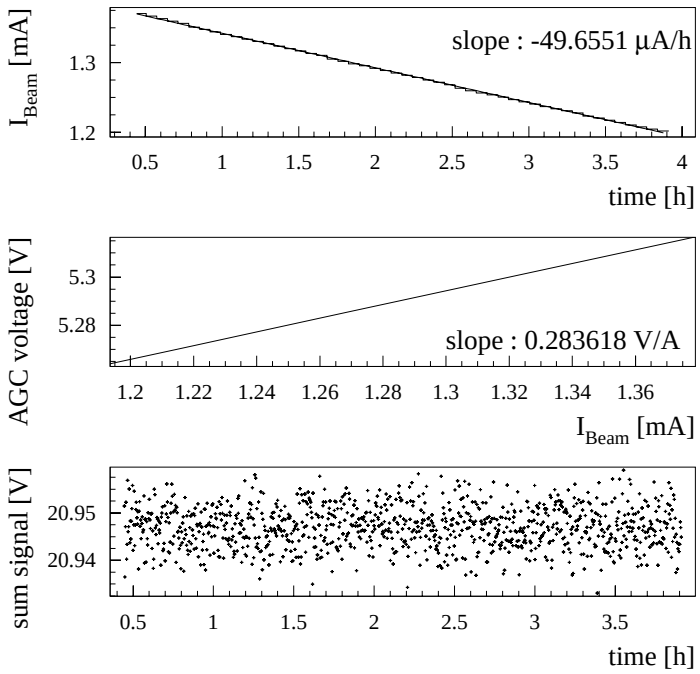

Figure 4.6: Top: LEP beam current during a polarisation fill against time. Middle: AGC signal against beam current for the same period of time. Bottom: Sum of the signals given by the four electrodes of one BPM.

To allow a check of the model which relates the mean beam energy to the local beam energy (see Chapter 8) a separate observations of the two beams are needed. The BPM electronics have the capability to gate out one of the beams. As the spectrometer is positioned $420\,\mathrm{m}$ away from the particle collision point, the positrons pass the spectrometer magnet $2.74\,\mu\mathrm{s}$ earlier than the electrons. The LEP clock triggers a signal with a length of $2.6\,\mu\mathrm{s}$ and a rise time of $150\,\mathrm{ns}$ which may be used to gate out either the electron or positron signal.

4.3 Wire Position System

A wire position system was installed to observe the movements of the BPM mountings with respect to each other. This is necessary because the beam position at the different stations has to be measured with an accuracy better than $1\,\mu$m. For example a temperature change of $1\,^{o}$C over a length of 10 cm causes a displacement of $2\,\mu$m due to the expansion of the aluminium mounts.

4.3.1 Principle of Operation

The principle of the position measurement is based on sensing the capacitance between opposite planar electrodes of the sensor and the wire. This is achieved by measuring the current from the electrodes while an alternating voltage is applied to them. The voltage has an amplitude of $10\,$V peak to peak relative to the grounded conducting wire and a frequency of $4\,$kHz. The capacitance is, to the first order, inversely proportional to the distance in this arrangement. Investigations of the field inside the sensor and the wire position sensor (WPS) response can be found in Appendix E. To obtain the wire position, the analogue signals from opposite plates are subtracted. To ensure that the electrodes measure only the capacitance with respect to the wire, they are surrounded by guardrings, which are supplied by an oscillator in phase with the potential on the electrodes. Since the potential difference between guardring and electrode is zero, the field lines do not bend towards the grounded frame of the sensor head. The electronics of the whole setup are sketched in Fig. 4.7. To avoid an electric current flowing over the wire, they are grounded outside the tunnel at one point. Such a current could be induced for example by the so-called TGV effect [20].

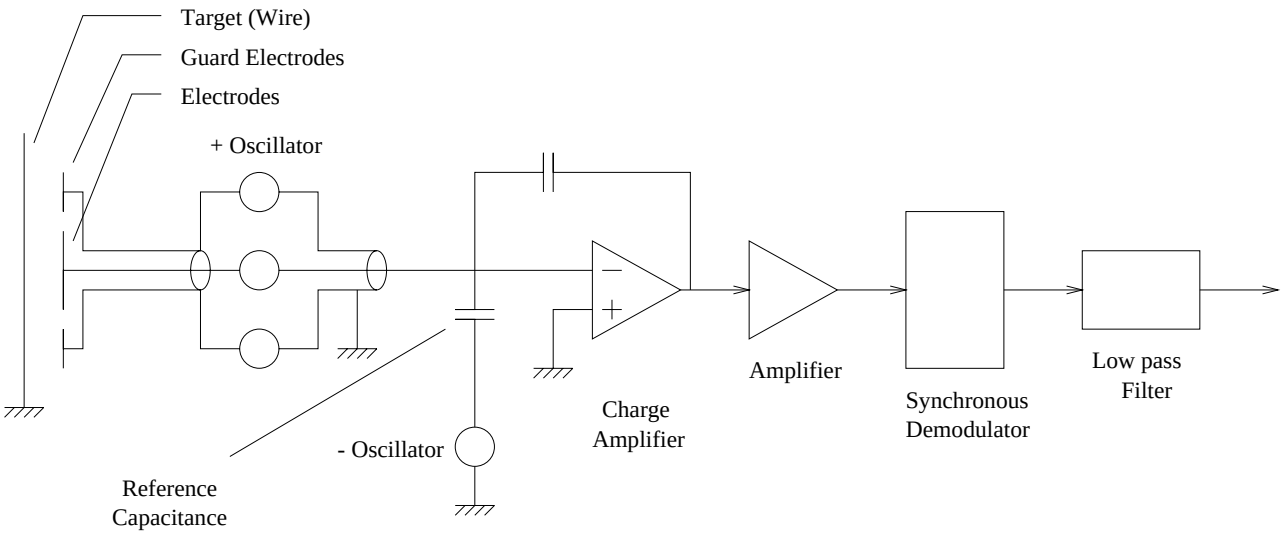

Figure 4.7: Electronic of the WPS.

4.3.2 Layout

The wire position system installed at the spectrometer (see Fig 2.3) uses three wires, which consist of carbon surrounded by kevlar. The wires have a diameter of $0.4\,$mm. The first extends over the whole spectrometer and is intended to observe movements of the arms of the spectrometer with

respect to each other. Two further wires are installed, one on each arm for redundancy and also to distinguish between shifts and expansions of the BPM supports. Expansions have a negligible effect on the beam position measurement, due to the symmetry of the elliptical cross section (Chapter 5.2.2). There are eighteen WPSs installed at the spectrometer: one on either side of each BPM support and one at each mounting point of the wire (so-called reference sensor (WRF)). Those on the BPM supports observe movements of the BPM with respect to the wire and those at the fixing points observe movements of the wire with respect to the supporting limestone block. They are attached to the block by a copper tube, which is stabilised by the BPM water temperature regulation system. The latter observe movements of the mounting and the point where the wire is bent over a pulley and stretched by a weight.

The reference sensors (WRF) are assumed to be fixed and taken as a reference. The movements they detect are identified with real, undesired wire movements with respect to the mounting. They are used to correct the wire position sensor (WPS) readings.

The corrections also depend on the position of the individual WPS along the wire. The size of these corrections can be derived geometrically: Fig. 4.3.2 shows the positions of the wire before (time 1) and after (time 2) a wire movement. The reference sensors register a change in wire position x_i which results in a misreading of the wire position sensors (WPS) of a_i. a_i consists of the offset x_1 and a contribution due to the angle δ between the direction of the axis of the wire before and after the movement. The size of the latter contribution is equal to the tangent of the angle multiplied by the distance of the sensor i to the reference sensor 1. The correction for the long wire can be constructed in an analogous way.

Sag of the Wire

The stretched wires experience a sag due to their finite weight. This effect does not affect the energy estimation as the sag only occurs vertically. To calculate the size of the effect, one has to find a function for the shape of the wire. The ansatz of minimising the potential energy of the wire in the gravitational field results in the following formula [33]:

$$y = \frac{H}{g\,\rho}\left(cosh\frac{\rho\,x\,g}{H} - 1\right)\ , \tag{4.4}$$

where H is the horizontal component of the stretching force F_0. As the vertical component T is small, H is identified with F_0. ρ is the mass of the wire per unit length. Thus the sag f can be calculated for the length of the wire l:

$$f = y\left(x = \frac{l}{2}\right) = \frac{F_0}{g\,\rho}\left(cosh\frac{\rho\,l\,g}{2\,F_0} - 1\right)\ . \tag{4.5}$$

The shape of the wire is sketched in Fig. 4.9. The wires used at the spectrometer have a length of $8\,$m ($26\,$m) and are stretched by a weight of $7\,$kg ($15\,$kg). The weight of the wire is $0.33\ \times 10^{-3}\,$kg/m.
This results in a sag f of $0.38\,$mm for the short and $1.9\,$mm for the long wire. As the weight of the wire and the stretching weight are obviously affected in the same way by homogeneous changes in the gravitational acceleration g (Eq. 4.4 contains only the ratio $(F_0/g)/\rho$), the system is insensitive against overall shifts of g due to effects such as the attraction of the adjacent Jura mountain. The system is only affected by differential changes of g such as those caused by the tides. These effects were analysed in the context of studies for the linear collider CLIC [34] which

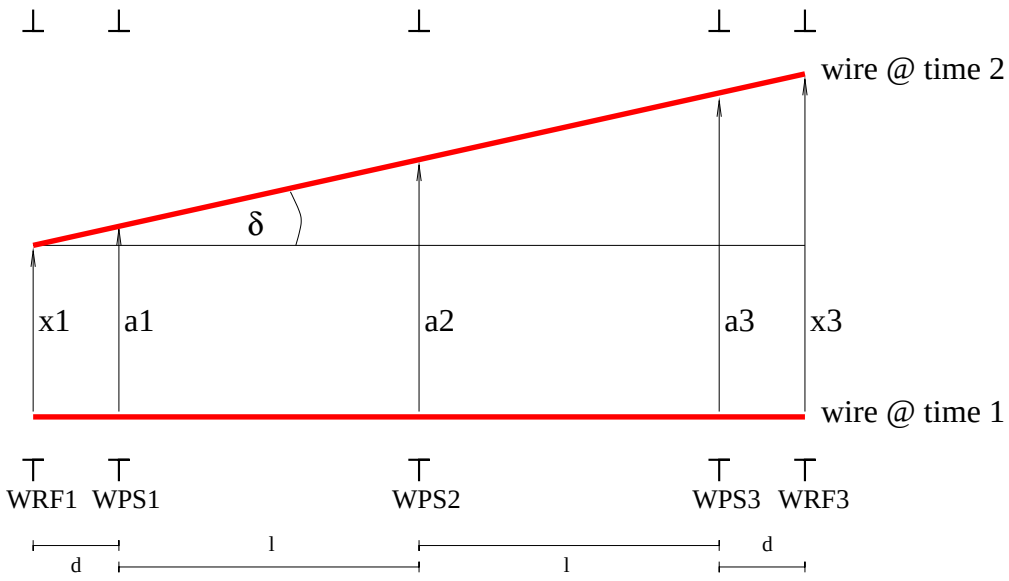

$$\delta = \frac{x_3 - x_1}{2l + 2d}$$

$$\begin{aligned} a_1 &= x_1 + d \tan\delta \\ a_2 &= x_1 + (d + l) \tan\delta \\ a_3 &= x_1 + (d + 2l) \tan\delta \end{aligned}$$

$$wps_i \rightarrow wps_i - a_i$$

Figure 4.8: Principle of correcting all WPS according to the reading of the reference sensors.

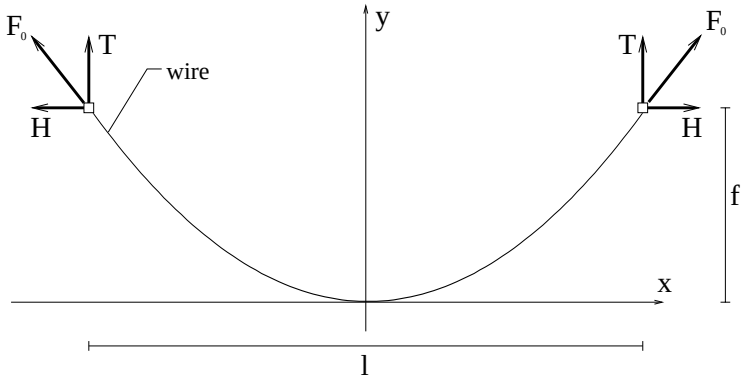

Figure 4.9: A wire which is fixed at two points experiencing a tension F_0.

will use the same wire position system to realise its sophisticated alignment requirements and were found to be negligible.

Variation in Altitude

The tangent to the LEP accelerator at the spectrometer has an inclination of $1.27\,\%$ with respect to the surface of the earth. This tilt results in a difference in altitude over the length of the long wire (26 m) of 330 mm.
According to Newton's law of gravity the acceleration g caused by the earth (mass M) at a distance r (here radius of the earth) from its centre of mass is given by the following equation:

$$g \;=\; G\,\frac{M}{r^2}\;. \tag{4.6}$$

For two distances r and $r+\Delta r$ a difference in the acceleration results:

$$\Delta a \;=\; \frac{GM}{r^2}\,\left(1-\frac{r^2}{(r+\Delta r)^2}\right) \;=\; g\,\left(1-\frac{r^2}{(r+\Delta r)^2}\right)\;. \tag{4.7}$$

g is the gravitational acceleration and r the radius of the earth (6.370×10^6 m). Thus the inclination implements a variation in g of $9.8\;\times\;10^{-7}$ m/s^2. This effect is negligible, especially because it is constant in time.

Wire Oscillation

The airflow in the LEP tunnel excites an oscillation of the wires with their resonant frequencies. The stretching force F_o ($\parallel$ wire (x)) for a bent string (radius R) results in a restoring force F ($\perp$ wire (y)) on a part of the wire dx.
A geometrical approach results in the following expression [35]:

$$F = F_o\frac{dx}{R}\;. \tag{4.8}$$

For a small deflection $1/R$ can be identified with d^2y/dx^2, which results in:

$$\frac{d^2y}{dt^2} = \frac{F_o}{\rho A}\frac{d^2y}{dx^2}\;, \tag{4.9}$$

where ρ is the density of the string and A its cross section.
This equation describes a wave travelling with the speed c:

$$c^2 = F_o/(\rho A) = (\lambda\nu)^2, \tag{4.10}$$

where λ is its wavelength and ν its frequency.
The constraint of $y=0$ at the fixed points ($x=0$ and $x=L$) results in the following discrete frequencies for standing waves:

$$\nu = n\,\nu_o = n\,\frac{1}{2L}\sqrt{\frac{F_o}{\rho A}} \quad ; \quad n=1,2,3,\ldots\;. \tag{4.11}$$

The weight per length of the wire was measured to 0.33×10^{-3} kg/m and the stretching weights are 7 kg for the short (8 m) and 15 kg for the long (26 m) wire, so that the resulting fundamental ν_o is 12.8 Hz for the long and 28.5 Hz for the short wire.

The oscillation frequencies were measured by calculating a fast Fourier transformation (FFT) of the sensor signals. The results for the long and one short wire are plotted in Fig. 4.10. The peaks correspond to the resonant frequencies of the wires, as their amplitude was found to get smaller, the closer the observed sensor is positioned to the wire mounting. In the FFT signal of the long

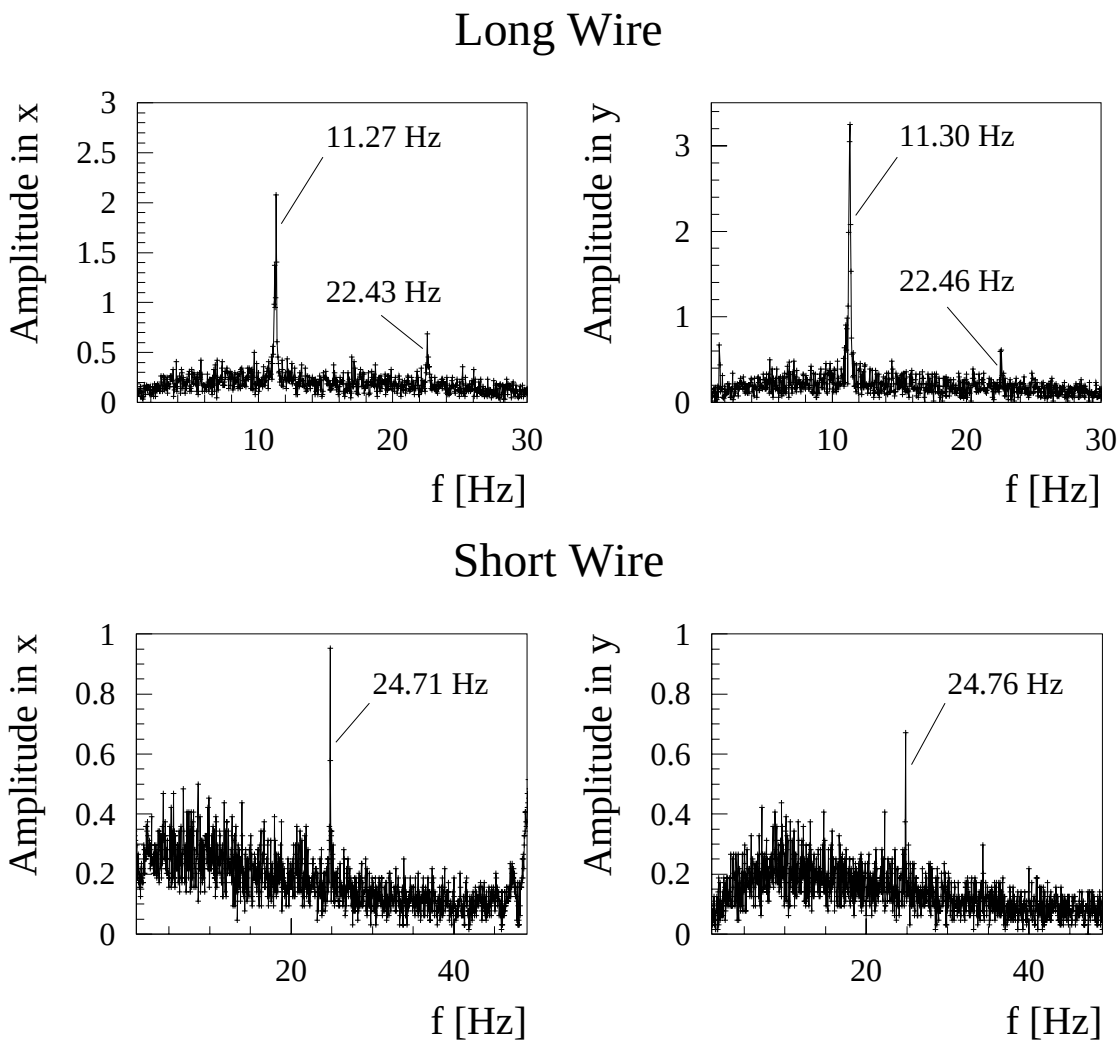

Figure 4.10: FFT of the x (left plots) and y (right plots) signal of a WPS for the long (top plots) and for the short (bottom plots) wire.

wire even the second harmonic ($n = 2$) can be seen, indicating that the oscillation is non harmonic.

The discrepancy between the predicted and measured frequency was found to be 1.5 Hz for the long and 3.8 Hz for the short wire. This difference may originate from the error on the measurements of the wire properties such as length, diameter and density.
The second order mode has, according to Eq. 4.11, twice the frequency of the first harmonic; this was observed within 0.1 Hz.

4.4 Water Temperature Regulation Stations

Besides the standard LEP cooling water circuit there are two stand alone circuits employed at the spectrometer. One temperature regulation circuit is used for the stabilisation of the bending magnet coil and the other for the beam orbit monitor supports. The temperature of the cooling water is increased by a regulated electric heater and decreased by a heat exchanger which is connected to the standard LEP cooling water. To control these processes a temperature sensor is used as a reference. The peak to peak temperature variation was found to reach $0.2\,^{o}$C. For reasons of security an interlock controls the reference temperature sensors and switches to LEP cooling in the case of a failure in the system.

BPM Water Regulation

All 6 BPMs are cooled by one cooling circuit, which is sketched in Fig. 4.11. This setup was chosen to provide an equal pressure, an equal water flow and thus an equal cooling power to all beam position monitor supports.

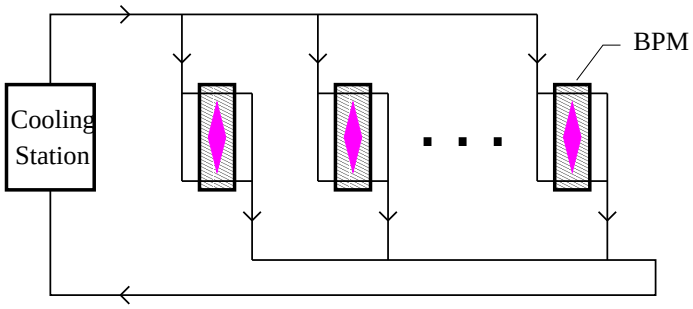

Figure 4.11: Cooling circuit which stabilises the BPMs.

To isolate each BPM from environmental changes, they are surrounded by a box of insulating material. The measures used result in peak to peak temperature variations of $\pm\,0.1\,^{o}$C. The adjacent copper absorbers are stabilised by the LEP cooling water.

4.5 Data Acquisition System

The analogue signals from the spectrometer constituents (6 BPMs, 79 temperature probes, 4 NMR probes and 2 fluxgates) are multiplexed and read out by 4 high accuracy digital Voltmeters (DVM) [36] which achieve a long term accuracy of 5 ppm. The method of multiplexing ensures a systematic error within the given accuracy similar to all channels.
The 12 position signals measured by the BPMs are the most important and are thus fed to a single DVM, which makes it possible to read each signal every 8 sec. To avoid the loss of data taken during these 8 sec, the signals from the BPMs are integrated by low pass filters with a time constant of 10 sec. The data are acquired during the whole operation period of LEP.

Chapter 5

Performance of the Spectrometer Instrumentation

5.1 The Dipole Magnet

The field properties of the analysing magnet were simulated by applying the software package Opera 3D [37] in order to ensure that the desired requirements were feasible [21]. One concern was transverse field homogeneity of $\int Bdl$ to avoid errors due to eventual orbit drifts in LEP. The gradient corresponds, according to the simulation, to a relative variation of 0.4 ppm/mm at 44 GeV and 1.0 ppm/mm at 100 GeV. The field measurements with the mole (Sec. 5.1.1) detected a relative change in the integral field of 4.6×10^{-5} over 1.5 cm of transverse displacement, which corresponds to 3.1 ppm/mm [38]. The difference between the maps corresponding to the two positions was not statistically distributed but had the same systematic behaviour as the absolute B field itself along the magnet. For mechanical stability the MBI was mounted on a steel girder, which was found to hardly contribute to the field as an additional return yoke. The extension of the end field is not well defined, which is why μ-metal shielding was mounted around the beam pipe to define the starting point of the far end field. The end field contribution is almost $10\,\%$ of the total integral of the field.

5.1.1 Mapping of the Analysing Magnet

A series of field maps was performed over six months during the 1998/1999 shutdown. The intention of this mapping campaign was to calibrate the four NMR probes fixed inside the magnet against the integrated B field for different energies between 41 and 105 GeV.
The temperature of the coil and the core were stabilised by a water cooling circuit. This is particularly important, as temperature variations have the following effect on the magnet:

- variation of the iron permeability,
- variation of the gap of the magnet,
- variation of the length of the magnet.

Furthermore, the rotating coil was employed to measure the higher order field components of the analysing magnet. The largest component is a quadrupole, which is negligible according to the measurement with the mole.

The Structure of the magnetic field in the Spectrometer magnet

The inner profile of the dipole field is not homogeneous on a 10^{-4} level (see Fig. 5.1). The periodic

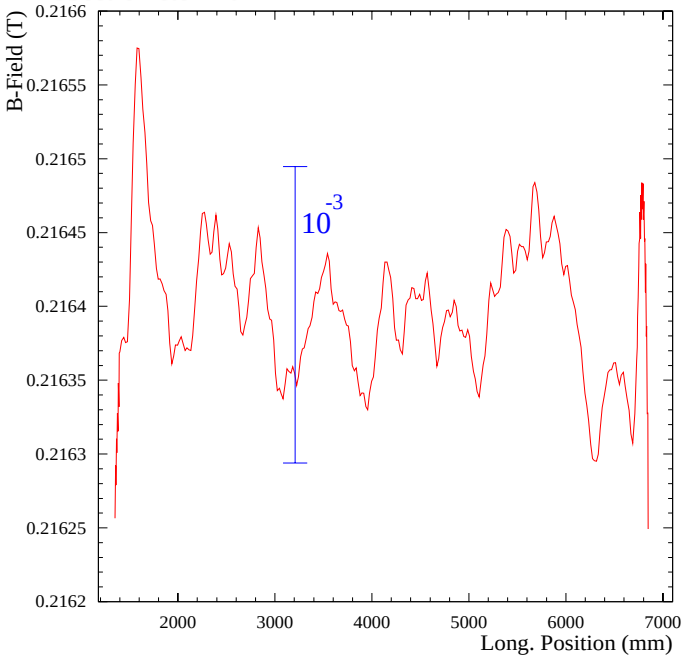

Figure 5.1: The inner magnetic structure of the analysing magnet of the spectrometer.

variations of the field along the magnet are caused by the buildup of the yoke.

The Tools for the Determination of the Integrated Magnetic Field

For measuring homogeneous magnetic fields NMR probes offer the best available absolute accuracy (better than $\pm$ 5 ppm) [26]. However, they cannot cope with the high field gradient at the ends of the magnet. A device sketched in Fig. 5.2 was made to travel inside the vacuum chamber and measure the local field [38]. This capability gave it the nickname "mole". The mole is pulled by a toothed belt driven by a stepping motor. The central field region is measured with two adjacent NMR probes. Two probes were used to achieve redundancy and to measure the transverse field homogeneity. The end field is measured by a coil with about one thousand windings and a surface of about 2.5×1.0 cm. This coil measures the change of the magnetic flux through its surface and thus provides the change in the B field while passing the end field of the magnet. The effective area of the coil was calibrated with NMR probes. The position in the magnet, which must be known to calculate the integrated field, was measured with a laser interferometer. This interferometer was also used for the WPS test stand and is described in Sec. 5.3.2.

The test bench sketched in Fig. 5.3 consists of a marble bench with an optical ruler. The field is measured by an NMR probe and two Hall probes which are mounted on a carbon fibre arm on a translation stage. The mechanics are optimised for position reproducibility ($2\,\mu$m) and stability with respect to temperature variations. In this setup the end field region is measured with the Hall probes, which allow field measurements down to the $1\,\mu$T level. The relative accuracy of the Hall probes is only 4×10^{-4}. Therefore the central field region was measured by more accurate NMR probes.

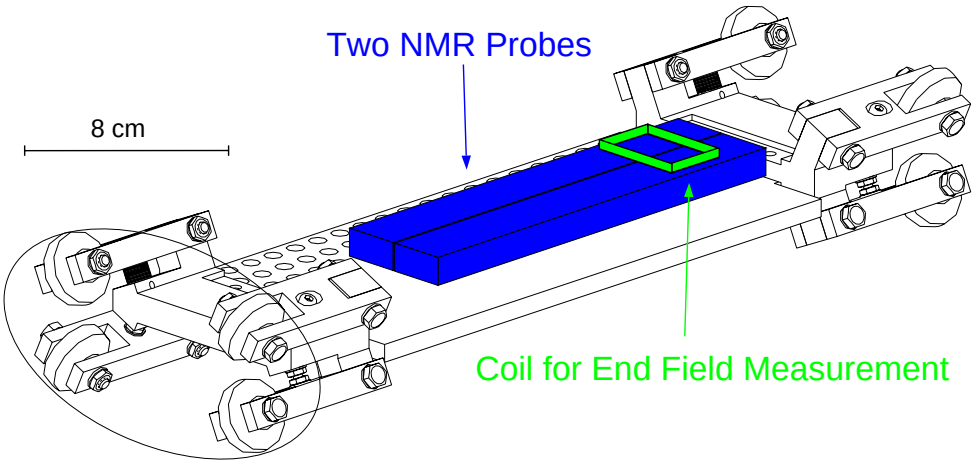

Figure 5.2: The so-called “mole”; a device with the capability to measure the integrated B field with the beam pipe in place.

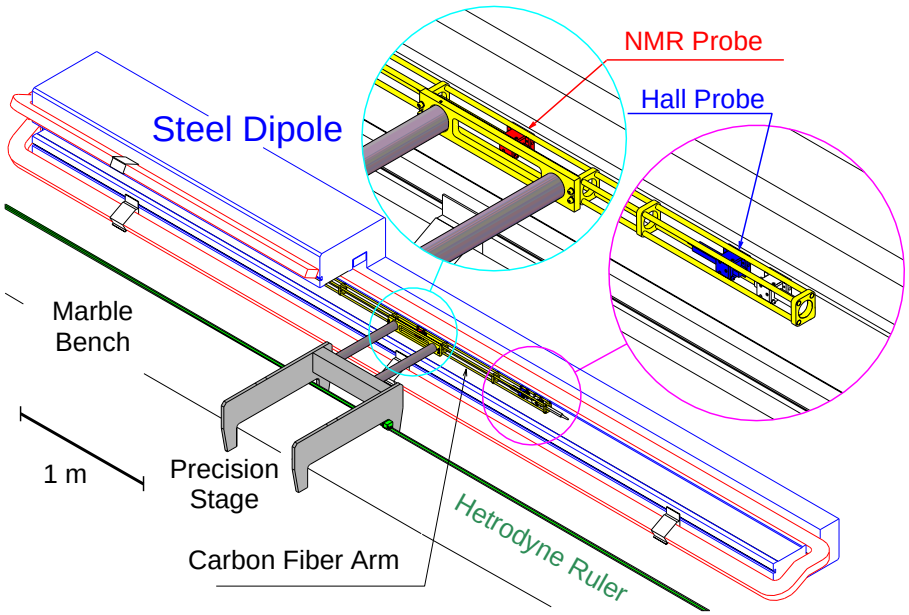

Figure 5.3: The mapping bench which allowed a determination of the integrated magnetic field of the MBI magnet in the laboratory.

The two setups reached the same accuracy on the integral B-field determination. The mole was designed to provide B-field measurements with the vacuum chamber installed and measurements after the transportation of the magnet into the LEP tunnel.

The Results of the Field Mapping Campaign

Fig. 5.4 shows the difference between the measured integrated magnetic field and the field predicted from the NMR probes fixed inside the magnet, as a function of the beam energy. A discrepancy from the linear correlation between both of $\Delta B/B = 3 \times 10^{-5}$ is observed. The circles correspond to the measurement of the integrated magnetic field using the test bench in the laboratory, the squares correspond to a measurement with the mole in the laboratory and the triangles to a measurement with the mole in the tunnel with the magnet in its final position.
As the results agree with each other within the statistical error, neither the insertion of the beam pipe nor the transportation from the laboratory to the tunnel changed the properties of the magnet. As is explained in Chapter 6 the relevant quantity for the energy estimation is the ratio between

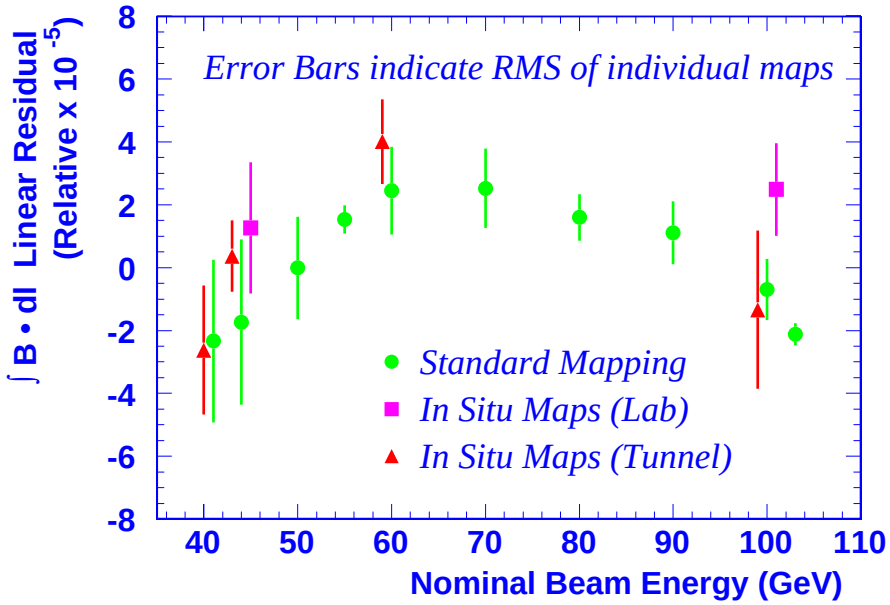

Figure 5.4: Difference between measured and predicted integrated B field for the different measurements which were performed.

the integrated fields at high (here $100\,\mathrm{GeV}$) and at low energies (here $44\,\mathrm{GeV}$). To determine the error in the estimation of this ratio it is convenient to plot the difference between the measured ratio and the predicted ratio Δ against the energy (see Fig. 5.5):

$$\Delta = \left(\frac{\int B^{100} dl}{\int B^{44} dl}\right)_{mapped} - \left(\frac{\int B^{100} dl}{\int B^{44} dl}\right)_{predicted\ by\ NMR} . \tag{5.1}$$

The value of Δ was found to be below 2×10^{-5}.

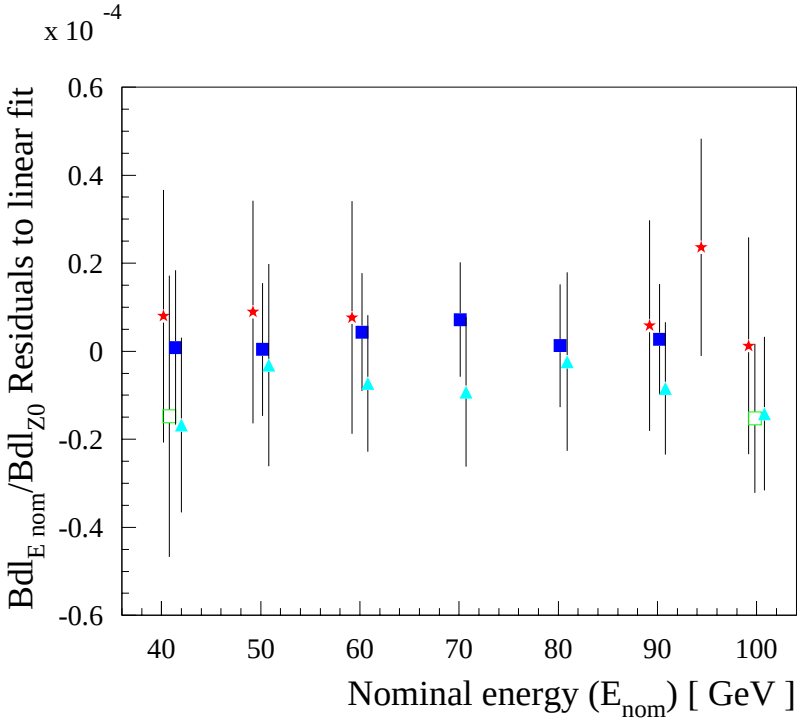

Figure 5.5: Difference between measured and predicted ratio of the integrated field at 100 and at 44 GeV for three different fills. Points of similar nominal energies correspond to the same energy. This shift was implemented for better illustration.

5.2 Beam Position Monitors

5.2.1 Investigation on the Performance of the Beam Position Monitors

The position monitors have to determine the orbit position with a relative accuracy of a few tenth of a micron. This accuracy must be obtained over a dynamic range of about $100\,\mu$m and a beam current variation of a factor of two. The dynamic range is imposed by the reproducibility of the beam position using corrector dipole magnets. This implies a knowledge of the relative gains of the BPMs accurate to a few 10^{-3}. A priori the relative gains of the 6 BPM electronics are only equal to a few 10^{-2}.

Gain Estimation

A measure for the stability of the BPMs independent of beam movements is the "triplet residual" T. As the arms of the spectrometer are free from magnetic fields (continuously monitored by fluxgates), the beam propagates in a straight line. As the BPMs on each side are equidistant, the following condition must be fulfilled:

$$T \;=\; \frac{x_1 \;+ x_3}{2} \;-\; x_2 \;=\; 0\,, \tag{5.2}$$

where x_i is the beam position at pickup number i.
This means that the mean of the two outer BPM readings (1,3) must be equal to the reading of the inner BPM (2). This is true for the two cases of an equal beam displacement in all BPMs and a rotation as sketched in Fig. 5.6 (left). As every other beam movement can be considered as a superposition of these two movements, Eq. 5.2 is always fulfilled. A more geometrical approach is sketched in Fig. 5.6 (right). As the beam propagates along a straight line, the angle of the two filled triangles must be equal:

$$\frac{x_2 - x_1}{L} = \frac{x_3 - x_2}{L} \quad \Rightarrow \quad \frac{x_3 + x_1}{2} - x_2 = 0\,. \tag{5.3}$$

As mentioned earlier, it is necessary to correct for the slightly different gains g_i and offsets o_i of

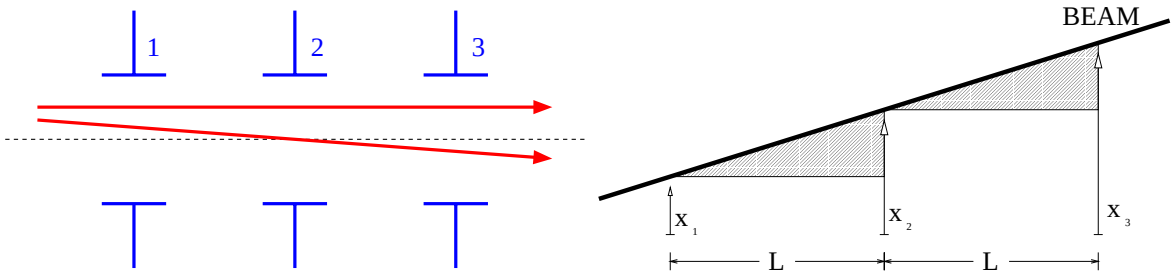

Figure 5.6: Left: Beam movements in one arm. Right: Geometrical derivation of the triplet residual.

the BPM electronics i. Ignoring higher order effects (described later in this section) the measured beam position b_i can be expressed as follows:

$$b_i \;= g_i x_i \;+\; o_i\,. \tag{5.4}$$

Inserting Eq. 5.4 into the equation of the residual (Eq. 5.2) results in:

$$\frac{b_1}{2}\frac{g_2}{g_1} + \frac{b_3}{2}\frac{g_2}{g_3} - b_2 = \frac{o_1}{2}\frac{g_2}{g_1} + \frac{o_3}{2}\frac{g_2}{g_3} - o_2 \,. \tag{5.5}$$

One can now calculate the difference between the formula for two generations of readings ($b_i^{(j)}$ and $b_i^{(j+1)}$):

$$d_1 \frac{g_2}{2g_1} + d_3 \frac{g_2}{2g_3} - d_2 = 0 \,, \tag{5.6}$$

where $d_i = b_i^{(j)} - b_i^{(j-1)}$.

Using the difference between readings leads to cancellation of the offset term (see Eq. 5.6) under the assumption that the offsets are time independent. This assumption is fulfilled to the required accuracy which can be estimated from the RMS of the triplet residual of 245 nm in Fig. 5.7. Eq. 5.6 contains only the gains and the BPM readings. Different procedures based on this equation were designed to get the relative gains g_2/g_1, g_2/g_3 and the equivalent for the other arm of the spectrometer. One procedure is to minimise the RMS of the distribution of the triplet residual by varying the gains. The second and very instructive approach is to plot d_1, d_2, d_3 into a three dimensional graph. The variable d_1 is plotted on the x-axis, d_3 on the y-axis and d_2 on the z-axis. Eq. 5.6 represents the equation of a plane with zero offset in this three dimensional space. Therefore all measured beam positions should be found in this plane. The relative gains can be deduced from the slopes of the plane which is fitted to the data. For equal gains ($g_1 = g_2 = g_3$) such a plane is plotted in Fig. 5.8. Starting from this diagram it is convenient to move the beam through the spectrometer in a way that the plane is best defined. The procedure resulting from this approach is to perform so-called offsets (shift the beam parallel to the orbit: $\Delta x_1 = \Delta x_2 = \Delta x_3$) and angles (rotate the beam with respect to the central BPM: $\Delta x_2 = 0, \Delta x_1 = -\Delta x_3$). In the top plot of Fig. 5.7 the three BPM position signals from one arm of the spectrometer are plotted for such a procedure, where the beam was traversing the arm at three different angles (between 0 and 20 min.) and after that at three different offsets (between 20 and 37 min.). Big position changes introduce relatively slow transitions due to the 0.1 Hz low pass filters in the electronics. Therefore a cut was introduced: if successive readings differ by more than 175 nm, the readings are not taken into account. The movements plotted in Fig. 5.7 result in two orthogonal lines in the space spanned by the BPM readings d_1, d_2 and d_3 as plotted in Fig. 5.9 (left). The residuals to the fitted plane are plotted in Fig. 5.9 (right). The plot shows no indication of a systematic error in the procedure.

In the central and bottom plot of Fig. 5.7 the distribution of the triplet residual after applying the corrected gains is shown. Its standard deviation was found to be 245 nm. Note that during this time the beam moved over a range of 1.2 mm. The relative gains were found to be constant up to 10^{-3} before and after the acceleration to high energies and identical up to 10^{-4} for the different procedures.

To avoid errors due to nonlinear responses of the BPMs (Sec. 5.2.2), a constraint for the procedure is that the beam stays within the central region of the BPMs. One effect of an off-centred beam can be seen in the automatic gain control signal (AGC), which is perturbed by excursions of the beam bigger than 1 mm. An example for this can be seen in Fig. 5.14 (top).

As the quantity triplet residual is calculated from 3 BPM readings, the statistical errors on the individual BPMs contribute as follows:

$$T = \frac{b_1 + b_3}{2} - b_2 \;\Rightarrow\; (\Delta T)^2 = (\frac{\Delta b_1}{2})^2 + (\Delta b_2)^2 + (\frac{\Delta b_3}{2})^2 \,. \tag{5.7}$$

With the assumption that the errors on the BPM readings (b_i) are uncorrelated and have the same magnitude, one can simplify Eq. 5.7:

$$\Delta T = \sqrt{\frac{3}{2}}\,\Delta b\,. \tag{5.8}$$

This means that the statistical error on the triplet residual ΔT of $245\,\text{nm}$ corresponds to an error on the single BPMs Δb_i of $200\,\text{nm}$.

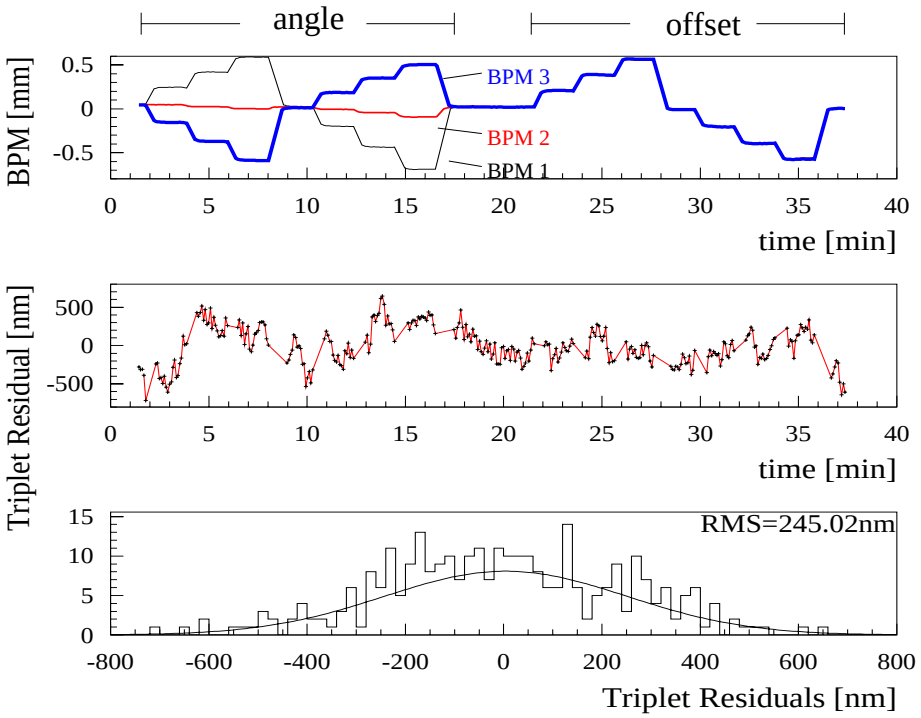

Figure 5.7: Top: Signals of the position monitors versus time. Middle: Triplet Residual (Eq. 5.6) versus time. Bottom: Distribution of the Triplet Residual.

Besides the relative gains the absolute gains should be known as well. Therefore the beam was sent through the spectrometer at different x positions. The readings from the spectrometer BPMs were compared with the position given by the standard LEP beam orbit monitors (BOMs), which are attached to the adjacent quadrupole magnets. This measure implies the reasonable assumption that the corrector magnets have the capability to shift the beam through all six BPMs in the same way as through the BOMs. In Fig. 5.10 the resulting gain of such a comparison for two beam displacements in x and one in y were plotted into a histogram.
The gain was found to be $(2.51 \pm 0.08)\,\mu$m/mV for the x and $(2.31 \pm 0.03)\,\mu$m/mV for the y signal.

Another method to estimate the absolute gain for the x signal is based on a change of the RF accelerating frequency, which alters the transverse position x of the beam in a defined way according to Eq. 2.10. The squares in Fig. 5.11 (left) correspond to a BPM signal averaged over 17 readings ($4\,\text{min}\,26\,\text{sec}$) at two RF frequencies before and after a change of $36\,\text{Hz}$. This change in signal was compared with the shift expected from Eq. 2.10. The resulting gains for all six BPMs can be seen in Fig. 5.11 (right).

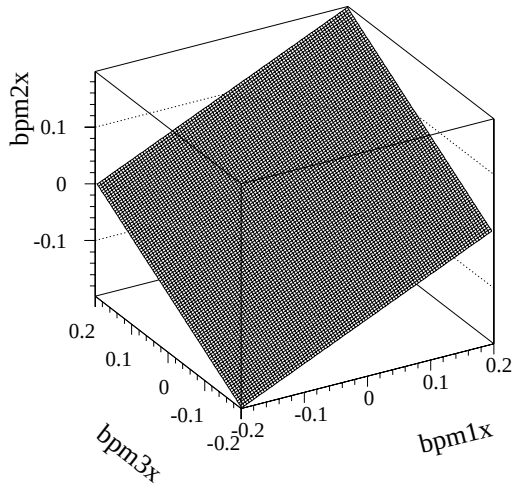

Figure 5.8: Plane of allowed combinations of BPM_1, BPM_2 and BPM_3 readings.

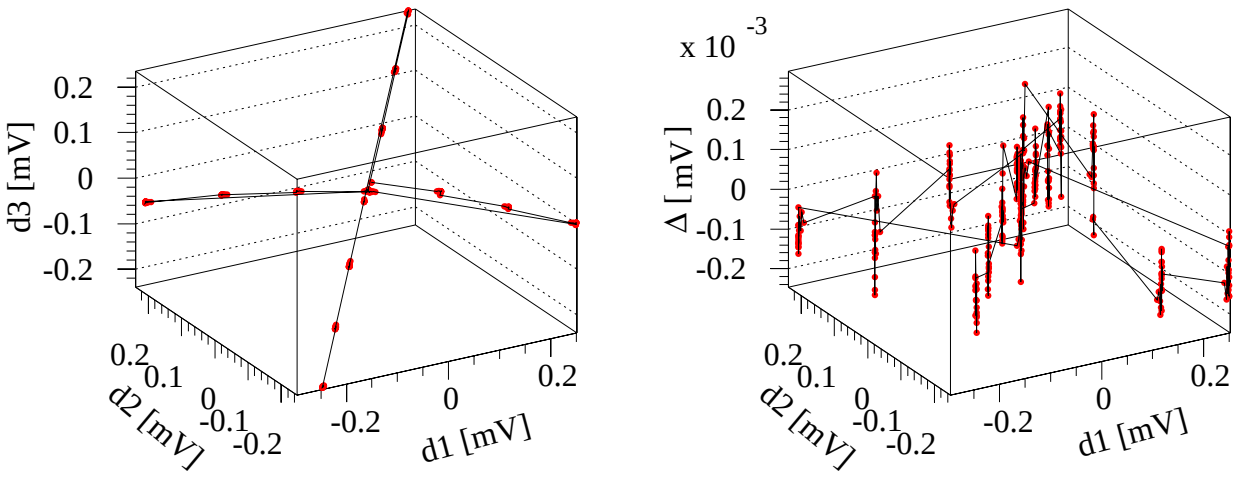

Figure 5.9: Left: The beam movements plotted in Fig. 5.7 in the d_1, d_2 and d_3 space. Right: Residuals to the fitted plane plotted against d_1 and d_2.

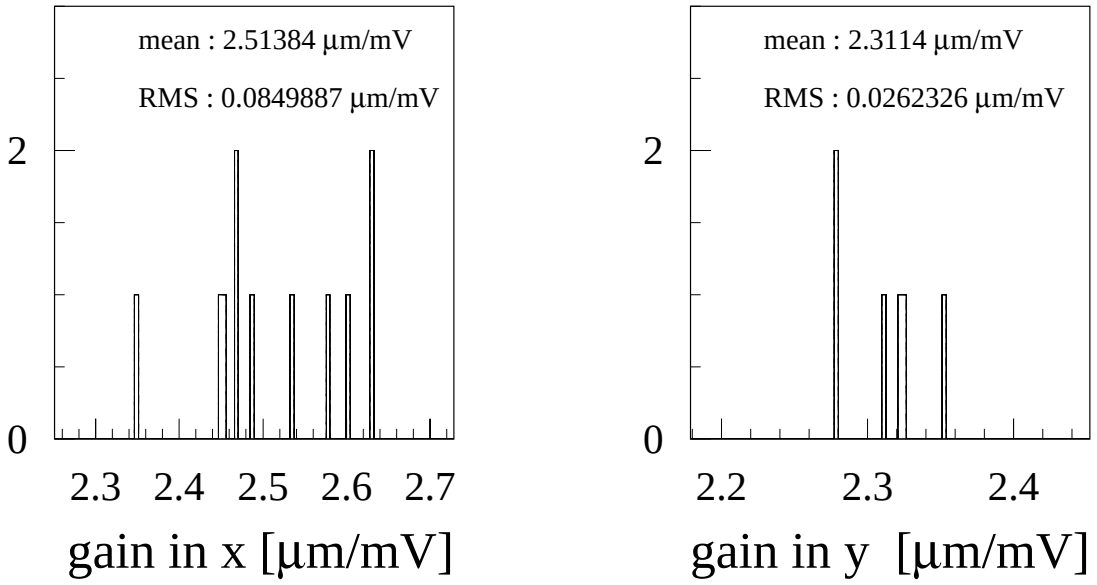

Figure 5.10: The gain estimated from the ratio of the BOM reading in μm and BPM in mV for displacements in x (left plot) and y (right plot).

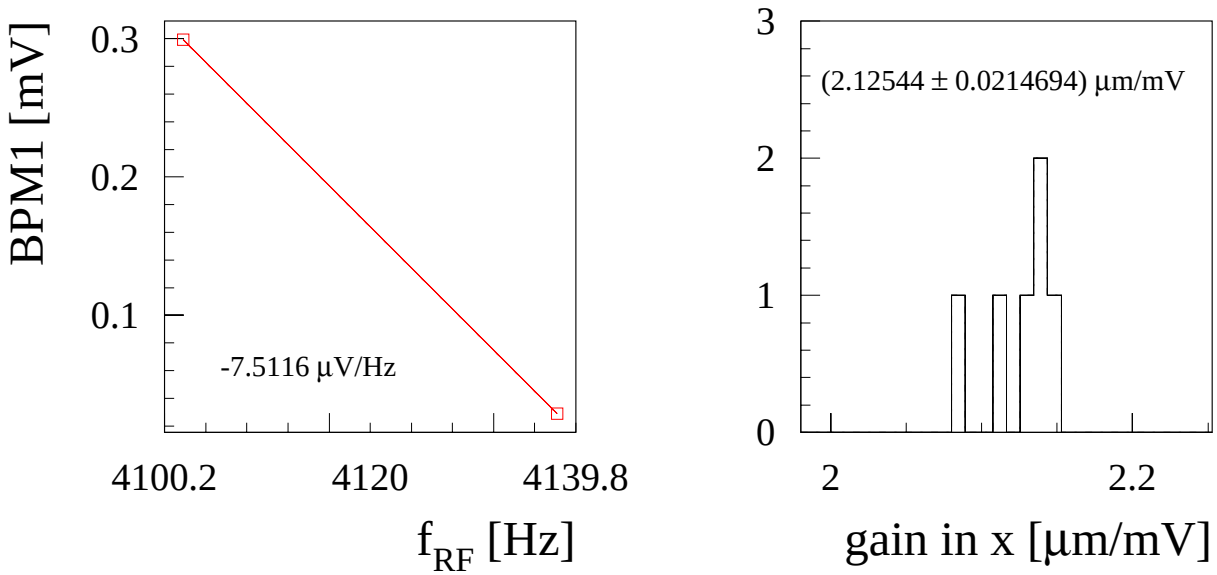

Figure 5.11: Left: Averaged beam position before and after a change in the RF frequency plotted against the frequency. Right: Resulting gain from comparing read signal and expected movement.

There is a significant deviation of unknown origin between the gain estimated from the adjacent LEP BOMs $(2.514 \pm 0.085)\,\mu$m/mV and the ones from an RF accelerating frequency change $(2.125 \pm 0.021)\,\mu$m/mV.

Another approach to estimate the absolute gains was to move the BPM itself during the operation of LEP and compare the excursions of the triplet residual (independent of beam motions) with the reading of the WPS. The BPMs were moved by heating up their aluminium support with resistors supplied with a voltage (see Fig. 5.12). The fundamental problem of this procedure is that the thermal conductivity of the aluminium heats up the BPM itself by $8\,^{o}$C during a movement of $60\,\mu$m. This obviously leads to distortions in the beam position measurement.

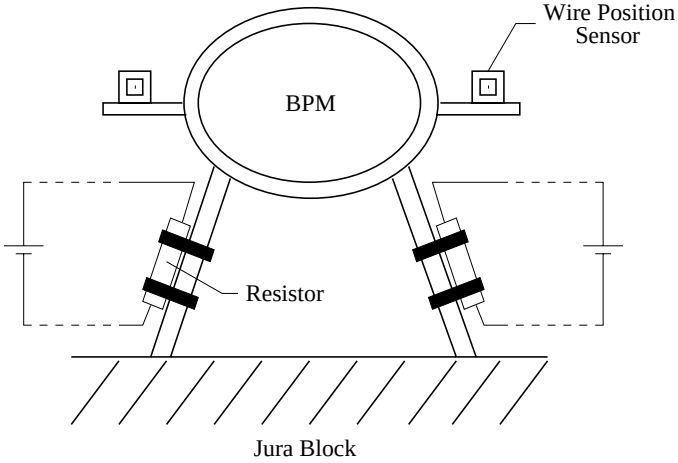

Figure 5.12: Systematic setup with heaters mounted on the BPM supports.

Automatic Gain Control Signal (AGC)

The AGC varies the gain of the electronics such that the sum of the signals from the electrodes (sum signal) of each beam position monitor (BPM) is constant (see Sec. 4.2.2 for more details). The BPM electronics provide an AGC voltage, which is proportional to the gain.

Calculation of the theoretical behaviour of the AGC signal during beam movements is interesting, because deviations to the observed signal could allow searching for undesired contributions to the signal from the synchrotron light: Such contributions would lead to an increase of the sum signals and thus can be detected in the AGC voltage. Furthermore the AGC signal might provide the opportunity to find the geometric centre of the BPMs.
The AGC signal should be proportional to the sum of all button signals, and thus could be calculated from Eq. 4.1 by integrating over the surface of the electrodes. For simplicity, point electrodes are assumed in the following equation. Furthermore the beam pipe is assumed to be round:

$$AGC \propto \frac{R^2 - x^2}{x^2 + R^2 - \sqrt{2}Rx} + \frac{R^2 - x^2}{x^2 + R^2 + \sqrt{2}Rx}\,.$$

This dependence of the AGC signal on the beam position x is plotted in Fig. 5.13. A beam pipe radius of 9 cm has been used.

To determine the geometrical centre of the BPM, the effect plotted in Fig. 5.13 could in principle be used, as the AGC signal is symmetrical with respect to the centre of the vacuum pipe. Unfortunately the size of the effect is too small.

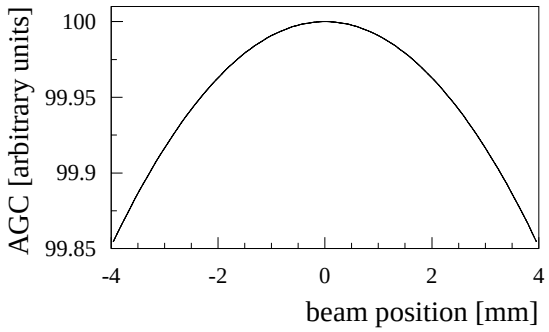

Figure 5.13: AGC Signal plotted against an x displacement around the centre of the pick up.

The top plot of Fig. 5.14 shows the beam position and the bottom plot the AGC signal against time. One can see that the response of the AGC signal is bigger, the further the beam is off the centre (corresponding to the $y = 0$ in the top plot). This is an indication that the response of the BPM is disturbed for an off centred beam.

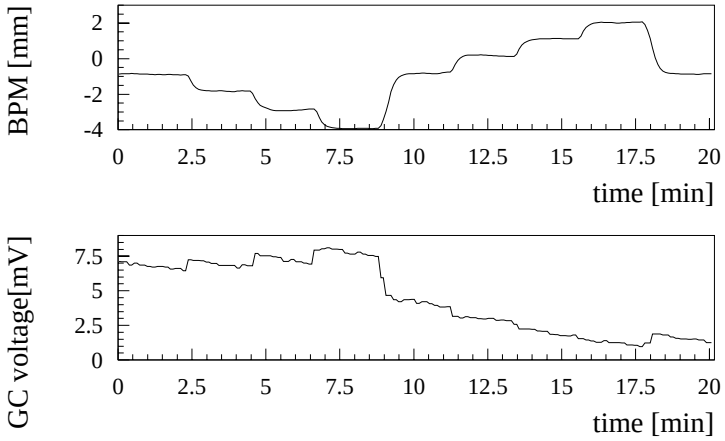

Figure 5.14: Top: Beam position versus time. Bottom: AGC signal versus time. Automatic gain control compensates the decrease of the signal due to the steady loss of current in LEP. The reference for this signal is the sum of all four buttons.

5.2.2 Higher Order Effects

As the BPMs are used in the sub micron regime, it is necessary to study their response carefully. According to [39], for a round beam pipe with radius a and point electrodes the correlations between the true beam positions x and y and the response of the BPMs X_{BPM} and Y_{BPM} are expressed by the following formula:

$$X_{BPM} \propto x \left\{ 1 - \left(3\frac{\sigma_x^2 - \sigma_y^2}{a^2} + \frac{x^2 - 3y^2}{a^2} \right) \right\} ,$$
$$Y_{BPM} \propto y \left\{ 1 + \left(3\frac{\sigma_x^2 - \sigma_y^2}{a^2} + \frac{3x^2 - y^2}{a^2} \right) \right\} . \quad (5.9)$$

σ_x and σ_y are the horizontal and vertical sizes of the beam. The beam positions x and y are measured from the centre of the BPM.

The signal $X_{BPM},\ Y_{BPM}$ is not only proportional to the beam position but contains as well a term proportional to its cube and a term depending on the beam size. Those corrections make it necessary to keep the beam in the central region of the BPM, as otherwise beam size variations affect the position measurement.

Effect of the Beam Size on the Position Measurement

According to Eq. 5.9 the difference in the horizontal and vertical size of the beam has an effect on the position measurement of the BPMs.
The beam size σ is correlated with the betatron function β and emittance ϵ approximately as follows:

$$\sigma(s) \approx \sqrt{\beta(s)}\sqrt{\epsilon} , \quad (5.10)$$

where s is the position around the storage ring.

The emittance is proportional to the phase space area of the beam and is thus under the assumption of a conservative system, due to Liouville's theorem, a constant of the motion.

The betatron function reflects exterior forces from focusing magnets and is highly dependent on the particular arrangement of quadrupole magnets and their excitation. It is calculated for LEP using software called MAD (Methodical Accelerator Design, available at CERN). Fig. 5.15 shows the size of the betatron function at the BPMs in the spectrometer, which determines the beam size along the spectrometer.

Strictly speaking Eq. 5.9 is not valid for the BPMs of the spectrometer, as it presumes a round beam pipe. Therefore the deviations in the response due to the beam size were simulated. The effect of this error on the angle determination according to the different beam sizes at the different BPMs (Fig. 5.15) was estimated. It was found that the real and the observed trajectory are tilted with respect to each other as sketched in Fig. 5.16, but that the angle is hardly affected [32]. In Fig. 5.17 the resulting relative error on the angle estimation due to the beam size variations along the spectrometer is plotted against the position of the beam with respect to the geometrical centre of the BPM.
The result of this analysis is that the beam size does not have any severe effects on the energy estimation as long as the beam passes all BPMs through their geometrical centre within $\pm\,1$ mm.

Nonlinear Responses of the BPMs

To understand the response of the standard beam orbit measurement system in LEP a series of measurements was performed. An antenna fed with an Rf signal was moved through the BPM using stepping motors to simulate the beam [40]. Fig. 5.18 shows the position of the antenna in

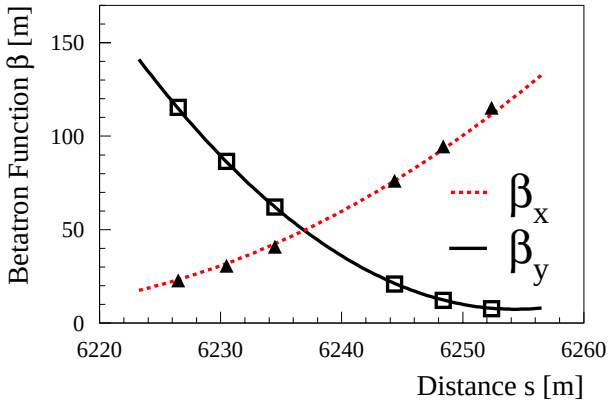

Figure 5.15: The progression of the beta function for the 102/90 Optics along the spectrometer. The triangles and squares correspond to the position of the BPMs. With typical horizontal (vertical) emittances of $\epsilon_x = 30\,\text{nm}$ ($\epsilon_y = 1\,\text{nm}$), the beam size varies according to Eq 5.10 between 0.77 mm and 1.8 mm (70 μm and 340 μm).

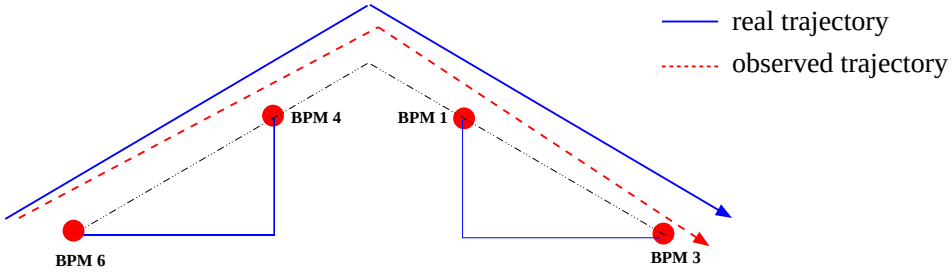

Figure 5.16: The effect of the different beam sizes at the BPMs on the trajectory and angle determination.

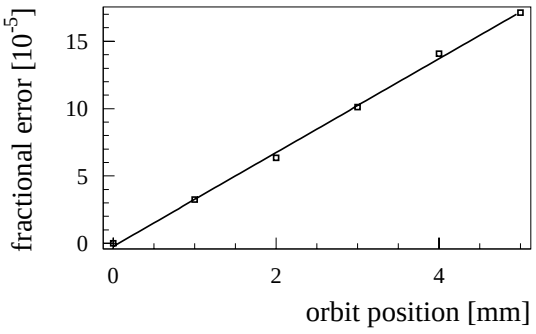

Figure 5.17: Relative error on the angle estimation plotted against the orbit position with respect to the geometrical centre.

the BPM plotted on the x and y axis and the output of the BPM for the x coordinate on the z-axis. These data were found to agree with the simulation program at the two percent level [32]. The

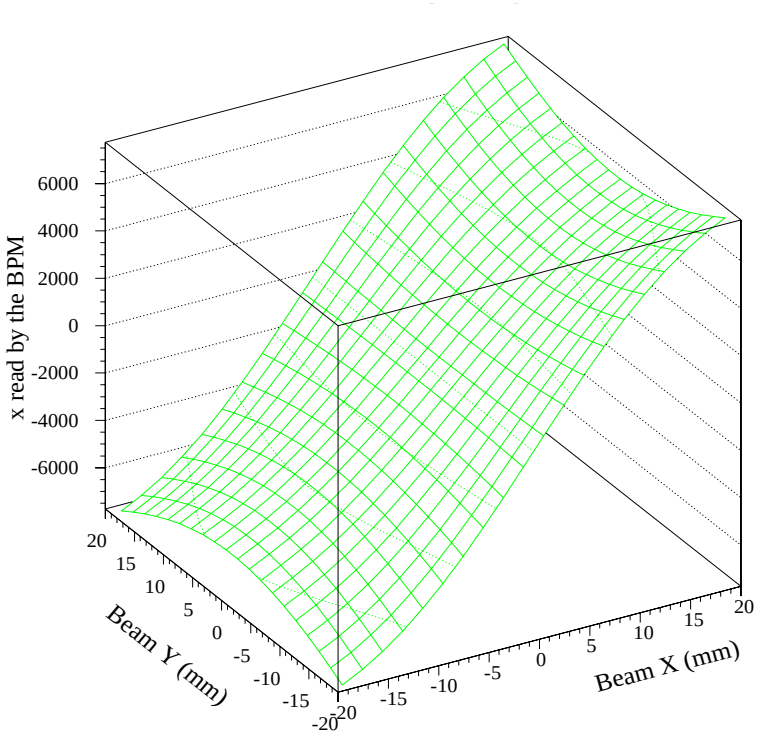

Figure 5.18: The horizontal beam position given by the BPM plotted on the z-axis against the x and y position of a wire with an electric pulse which is simulating a beam.

effect of the nonlinear response of the BPMs on the angle estimate was simulated. It was found that the alignment should be accurate to $300\,\mu$m [32].

Eq. 5.9 in principle reveals an opportunity to study the nonlinear term by for example moving the beam in the x direction and observing the y signal:

$$Y_{bpm} \propto C(\sigma_x, \sigma_y, y) + y\,\frac{x^2}{a^2}\,. \tag{5.11}$$

With this method the geometrical centre of the beam position monitor could be found by plotting Y_{bpm} against x. Attempts to fit a polynomial of second order failed since the range of the transversal movements of the beam is constrained to 2 mm and thus the effects are too small to be precisely determined ($y/a^2 < 6.25 \times 10^{-4}$). Other problems are potential electronic crosstalk and orbit drifts (even under stable beam conditions, the RMS of random beam movements was found to be $10\,\mu$m). Furthermore a possible tilt between the frame of coordinates of the closed orbit bumps and the observed BPM affect Eq. 5.11. Further data analyses are ongoing, especially studies on the advantages gained by mounting one or more BPM on stepping motors and thus making them remotely movable.

Besides these geometrical effects a centred beam reduces the errors of the electronic amplifier because similar signals are induced on all pickup electrodes. This has the advantage that the transfer function of the amplifier is only used over a small range.

5.3 Wire Position Sensor

5.3.1 Determination of Wire Sensor Ratings

Fig. 5.19 shows the setup of one BPM station with the BPM in the centre flanked by the two copper synchrotron light absorbers. The wire, its stretching weight and the position sensors attached to the BPM can be seen. For reasons of stability the whole setup is mounted on a limestone block which is grouted to the floor of the tunnel.
A basic test to check the behaviour of the sensors is to change the set point of the water temperature regulation system for the BPMs. A temperature increase ΔT leads to an expansion of the BPMs Δl, which is measured by the wire position system. This test was performed on several occasions for all BPMs. The expansion of the BPMs determined from the WPS signals can be compared with the expansion coefficient of aluminium α, from which the BPMs are made :

$$\Delta l = l\ \Delta T\ \alpha\ . \tag{5.12}$$

Fig. 5.20 shows the results of such an experiment; the top plot shows the introduced temperature change $\Delta T\ =\ 10^o$C, the lower the resulting expansion. Taking into account the distance between the wires $\Delta l\ =\ 30$ cm and the expansion coefficient $\alpha\ =\ 2.4\ \times\ 10^{-5}\ 1/$K this should result in an expansion of $69\ \mu$m, which agrees with the measurement. This test was performed to check the

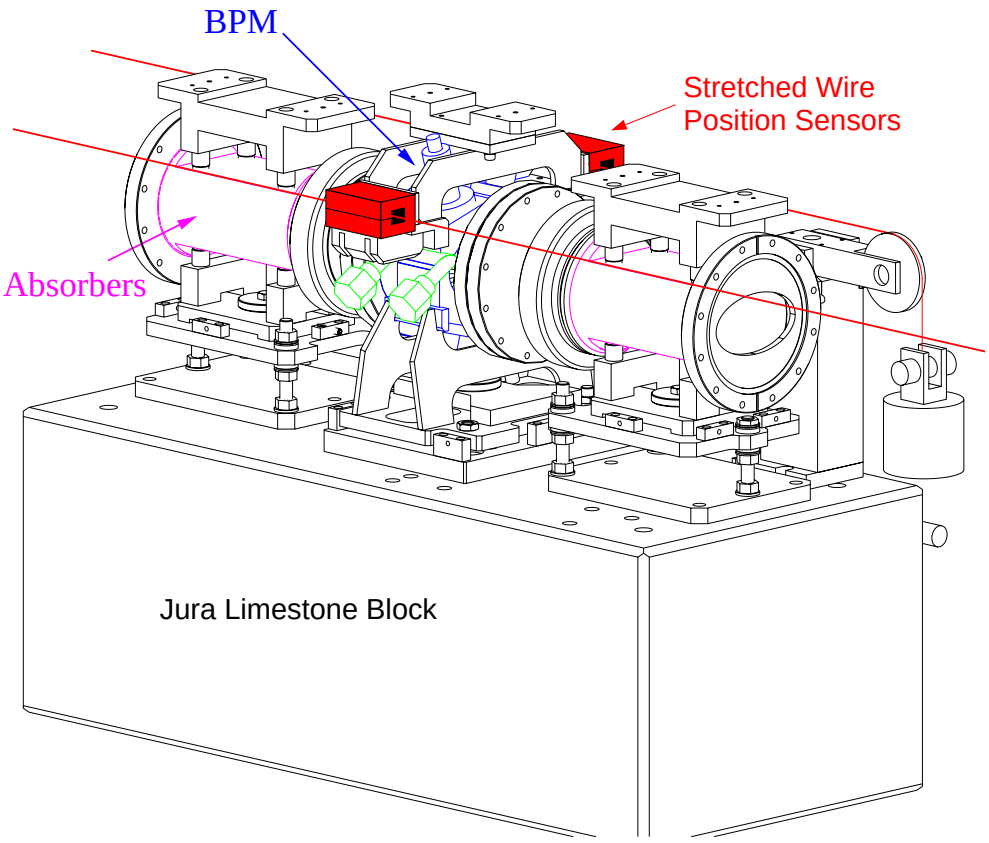

Figure 5.19: One of the BPM stations with its wire system.

whole wire position sensor system.
An upper limit of the resolution of the wire position system can be determined by the differences

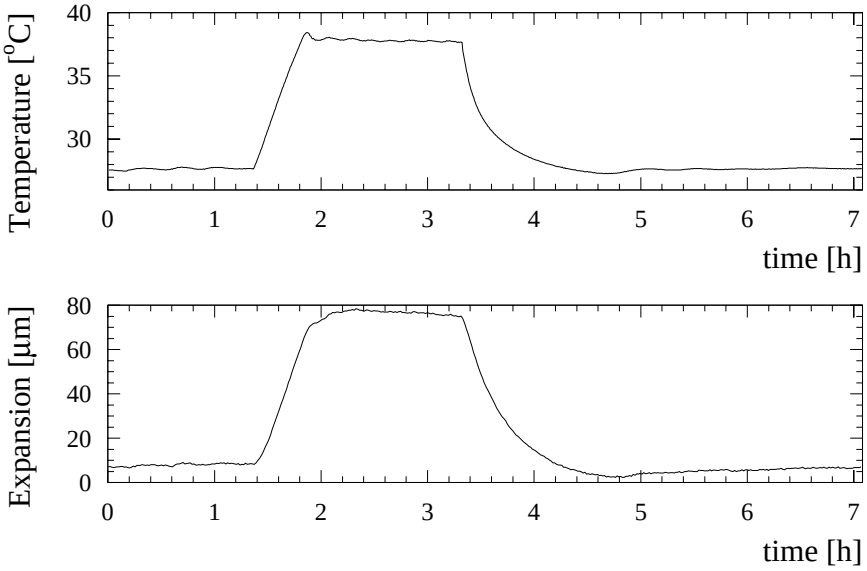

Figure 5.20: Top: Temperature of the BPMs against time, Bottom: Expansion of the BPM measured by the WPS against time.

between successive readings of the WPS. If the wire does not move in such a $12\,\mathrm{s}$ period, this difference provides the resolution. The distribution of the difference between successive readings

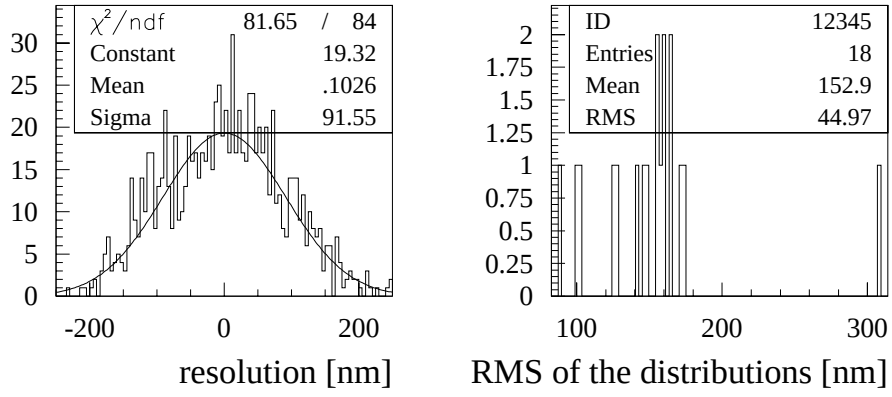

Figure 5.21: Left: Distribution of the difference between successive readings of one WPS over 17 h. Right: The standard deviation of these distributions for all 18 Sensors.

was found to be Gaussian (see Fig. 5.21, left), with a mean RMS of $(153 \pm 11)\,\mathrm{nm}$ (see Fig. 5.21, right). This plot shows the RMS of the differences between successive readings of all 18 WPS. The resolution of all sensors is better than the accuracy required.

5.3.2 Calibration of wire sensors

To determine the absolute accuracy of one WPS, a test stand as sketched in Fig. 5.22 was constructed to move the sensor head with respect to a fixed wire employing stepping motors. The measurement of the WPS is compared with that of the displacement measuring interferometer (described in the next paragraph), which determines displacements of the WPS. This test stand made us aware of the impact of small environmental variation on measurements in the micrometer regime. If the distance between wire and interferometer is altered, this is interpreted as a gain drift of the WPS and thus has to be avoided. Therefore this distance was fixed by a construction made from carbon fibre (temperature coefficient of $\alpha = -5 \times 10^{-7}$). The resolution of the laser

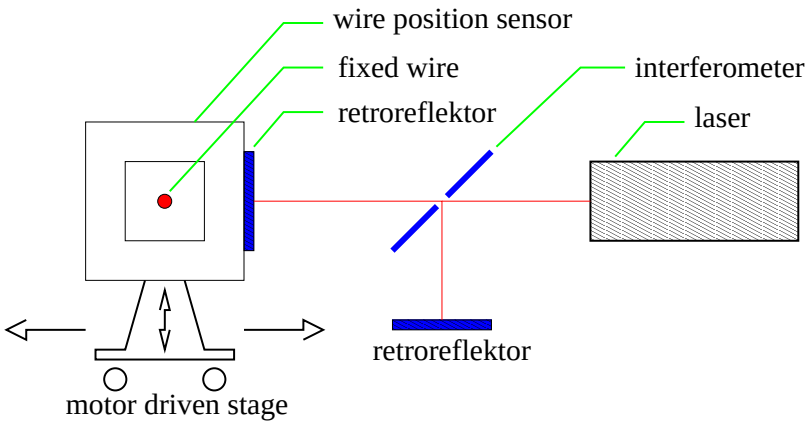

Figure 5.22: Test stand to verify the absolute accuracy and stability of the used WPS.

interferometer and the WPS was estimated by plotting the difference between successive readings into a histogram (Fig. 5.23) and was found to be of the order of 20 nm for the laser interferometer and 52 nm for the WPS. The bin width corresponds to the limited number of digits on the voltmeter for the laser.

The gain of the WPS was estimated as follows: The sensor was shifted such that the wire was moved in 100 steps within the centre (± 0.5 mm) of the aperture of the sensor. The gain results from the slope of the linear fit to the correlation between the WPS reading and the position measurement of the interferometer. This procedure took approximately 20 min. To test the stability of the response characteristics this gain estimation was repeated 99 times. The results are plotted in Fig. 5.24. A relative stability of the gains of 5×10^{-4} was found.

Position monitoring with an Interferometer

The helium-neon laser source [41] employed emits light with a well known and stable wavelength $\lambda = 632.8$ nm. By applying a magnetic field to the laser tube, the energy levels of the helium-neon are split according to the spin of the electrons, due to the Zeeman effect. Therefore the emitted laser light consists of two frequencies (F_1 with right circular polarisation and F_2 with left circular polarisation). The intensities are tuned to be equal for both frequencies. The beam passes a $\lambda/4$ plate which converts the right and left circular polarisation of the light to linear horizontal and linear vertical polarisation respectively. A first splitter deviates about $20\,\%$ of the light to a reference detector. This photo-detector measures the reference frequency $\Delta F = F_1 - F_2$ which is of the order of 2 MHz. The main light beam is transmitted to the interferometer, where a polarising

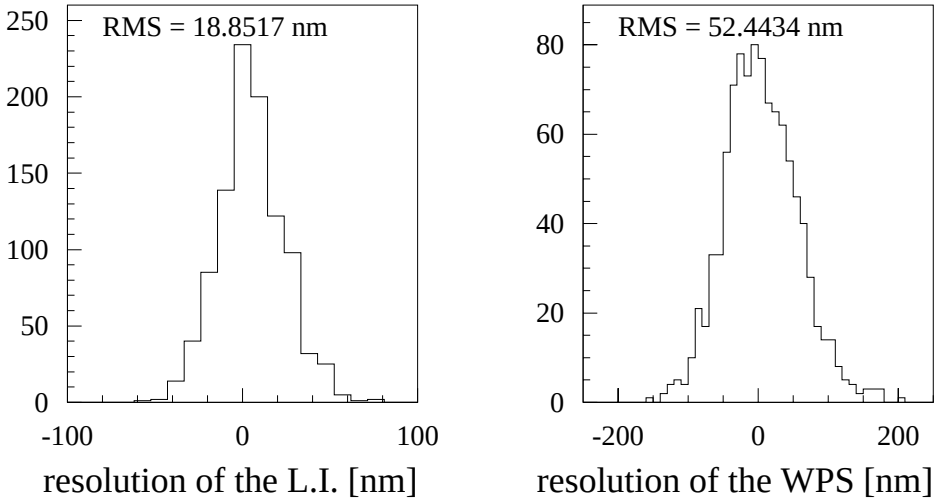

Figure 5.23: The difference between successive readings of the laser interferometer (left) and the WPS (right) give an estimation of the upper limit of their resolution.

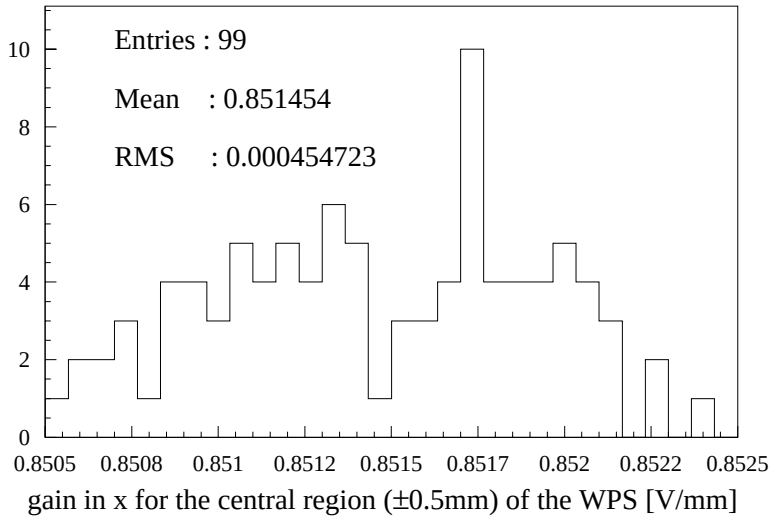

Figure 5.24: Stability of the WPS response.

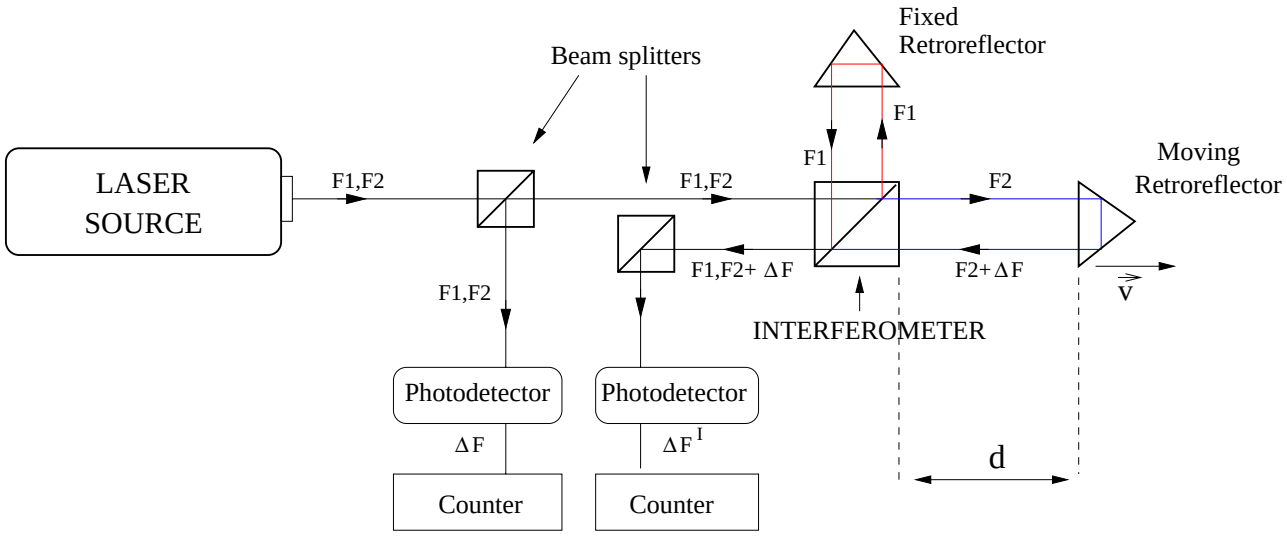

Figure 5.25: Schematic drawing of the employed laser interferometer.

beam splitter allows one frequency component (F_2) to pass whilst the other one (F_1) is deflected by 90 degrees. The component F_1 is reflected by a fixed retroreflector and is thus used as a reference. When the moving reflector travels with a speed v with respect to the interferometer the frequency F_2 is shifted and becomes F_2^I according to the Doppler effect:

$$F_2^I = F_2\left(1+\frac{v}{c}\right) = F_2 + F_2\frac{v}{c}\,. \tag{5.13}$$

Both components are recombined at the interferometer and travel to a photo-detector, which analyses the frequencies and outputs their difference:

$$\Delta F^I = F_1 - F_2^I = F_1 - F_2 - F_2\frac{v}{c}\,. \tag{5.14}$$

The reference ΔF and the Doppler shifted signals ΔF^I are converted into logic pulses and sent to two different counters. Integration of both signals over the same time interval Δt followed by subtraction provides the relative displacement $\Delta L_{\Delta t}$ of the retroreflector. This displacement depends only on the difference between ΔF and ΔF^I and the beam light wavelength in the surrounding medium λ [41]:

$$L_{\Delta t} = \frac{c}{F_2}(\Delta F^I - \Delta F) = \lambda(\Delta F^I - \Delta F)\,. \tag{5.15}$$

The required wavelength in air λ_{air} can be calculated from the well known wavelength of the light in vacuum λ_{vac} and the refractive index of air n_{air} which is temperature, pressure and humidity dependent:

$$\lambda_{air} \;=\; \frac{\lambda_{vac}}{n_{air}}\,. \tag{5.16}$$

The correction coefficients [41] read:

- 1ppm/^{o}C
- 1ppm/2.8 mm Hg

- 1ppm/90 % change of humidity

The instrument measures the position with a resolution of 10 nm [41].

An additional error on the position measurement could be introduced if the laser beam axis and the direction of movement are not parallel.
Any lateral displacement s during a longitudinal displacement r of the reflector introduces an error on the position measurement. This cosine error Δ is the difference between the dashed

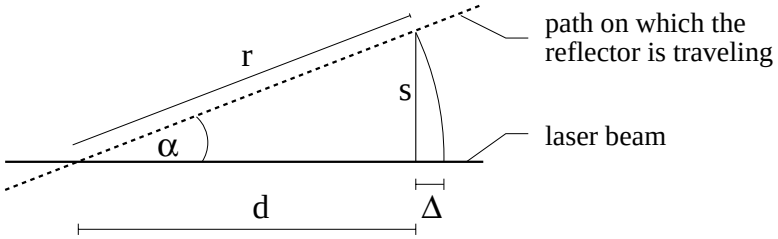

d : Dynamic range over which
the reflector is moved

Figure 5.26: Graphical approach to the cosine error.

hypotenuse r (actual displacement of interest) and the base of the triangle d (measured distance) seen in Fig. 5.26. It can be identified if the spot of the returning beam on the reflector is seen to shift laterally while the reflector is moving longitudinally. The error Δ can be calculated neglecting terms with higher order than α^2 :

$$\Delta = \frac{s^2}{2r} \,, \tag{5.17}$$

where s is the lateral displacement of the returning beam spot and r the corresponding longitudinal displacement of the reflector.

In the case of the test stand for the WPS, r is roughly 1 mm and s is invisibly small (< 0.2 mm). This leads to an error Δ of $10\,\mu$m or a relative systematic error of 10^{-2}. To minimise this error, an adjustment with a longer lever arm $r = 75$ mm was performed. Thus the relative error was reduced to 3.6×10^{-6}.

5.3.3 Study of systematic Measurement Errors of the WPS

The Synchrotron Light Effects

To study the systematic errors on the wire position system a search for correlations between measured position and other quantities was carried out.

In the plots of Fig. 5.27, the LEP current (top) and the signal from one sensor (bottom) are plotted against time. The LEP filling pattern is clearly seen in the raw signal of the WPS: At t_1=4 h leptons were injected into LEP; the energy was ramped at t_2=4.5 h; between t_2=4.5 h and t_3=8.5 h the beams were colliding and at t_3=8.5 h the beams were dumped. During a beam dump and the particle acceleration, there are fast position changes in the signal (so-called “jumps”) with a height of approximately $4\,\mu$m.
During particle acceleration the energy deposition from the beams due to synchrotron light

increases from almost 0 to about 700 W/m for a beam current of 10 mA. This seems to affect the sensor significantly. The particle acceleration and the beam dump correspond to the appearance and disappearance of synchrotron light. There is a correlation between the height of these position changes and the position of the wire in the sensor (see Fig. 5.28). In the situation where the wire is in the centre of the WPS, no instantaneous position changes were observed. To understand this systematic effect, the material of the wire and the support for the electrodes were changed. Furthermore the measurement conditions were varied without significant improvement. The correlation was also still observed with the wire fixed temporarily to the frame of the sensor (Fig. 5.29). The jumps occurred even though the wire itself was stationary, which means that the effect is an artefact arising within the sensor itself and is not related to a wire movement.
Assuming that the fast position changes arise from charges produced by the radiation, which are collected by the electrodes, it was attempted to reduce this effect by gluing kapton tape on the electrodes. However the jumps were not significantly reduced.
On one sensor the glue which attaches the electrodes to the stainless steel support structure was changed. In Fig. 5.29 the circles with the note "new glue" correspond to this sensor. It can be seen that the modifications did not change the characteristics of the jumps. The same can be said for the sensor which was mounted on a different support made from $Al\ O_2$. To investigate the energy dependence of the wire position sensor signal, during one particular fill, the particle acceleration was interrupted and LEP stayed for 10 min each at six different energies between 22 and 92 GeV. The measured wire position changes during the increase of the energy by $10\,\mu$m. The amount of displacement expected from the temperature increase of the BPM support was subtracted from the movements and the result plotted against beam energy. The data were fitted with a polynomial of fourth order (see Fig. 5.30), because the total power of the radiated synchrotron light increases with the fourth power of the particle energy (see Eq. 2.15). The fit supports the hypothesis that the unexpected movements are correlated with the synchrotron radiation of the beam. To investigate on this a DC voltage of 19 V was applied to one of the alignment wires and the current flowing through this wire to ground measured during the acceleration time. This current was also found to increase with the LEP beam energy to the fourth power.

For the operation periods of LEP all sensors were aligned in such a way that the wire was within $150\,\mu$m to the centre. This made the "jumps" in Fig. 5.27 smaller than $0.5\,\mu$m. Furthermore, a centred wire gives a very linear response from the WPS as shown in Fig. 5.31, where the response of the WPS (z-axis) is plotted against the x and y position of the wire in the sensor. The data plotted in those figures were provided by the manufacturer (Fogale), who tests each of their sensors individually, by moving a wire in steps of 1 mm through the sensor with stepping motors. The position given by the stepping motors is plotted on x and y, the reading of the sensor (x in the left figure; y in the right figure) is plotted on the z-axis. From Fig. 5.31 one can see that there is a small amount of crosstalk between the x and y position reading (cushion shape) and small nonlinearities, when the wire is far (> 2 mm) away from the centre.

Assuming that the correlation of the sensor signals with the LEP beam is due to synchrotron radiation, the sensors were shielded with 2 cm of lead. This measure was successful on those sensors where space considerations allowed adequate shielding (see Fig. 5.32). Those sensors which could not be shielded entirely still show jumps in their signal of around $1.5\,\mu$ m. These jumps are, however, no longer correlated in size with the wire position as can be seen in Fig. 5.33, where each square corresponds to the size of a "jump" (y-axis) and the position of the wire in the sensor (x-axis). The solid line is a fit to these data, the dashed line is the same fit for the 1998

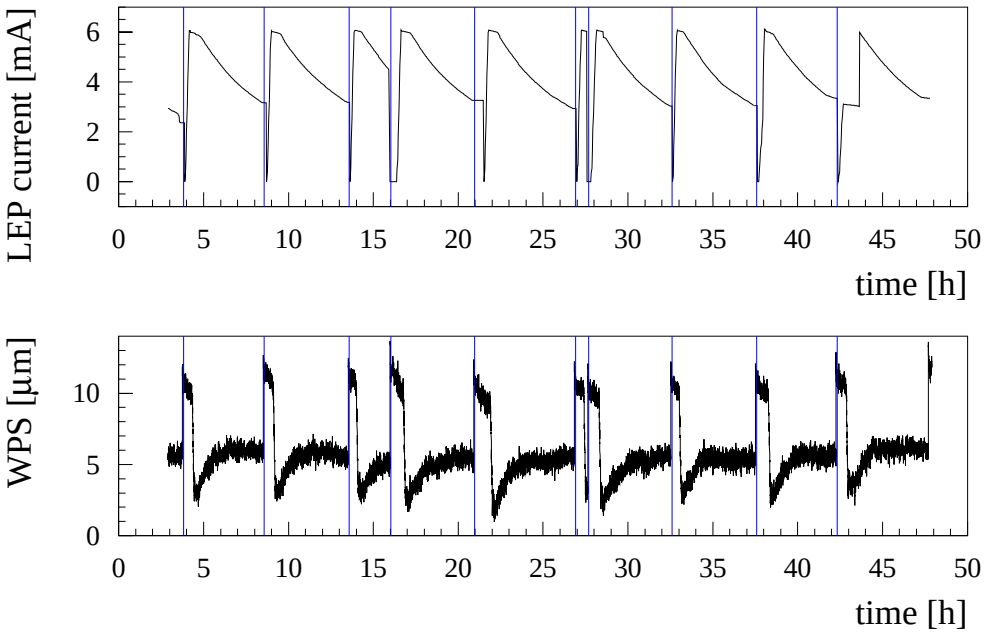

Figure 5.27: LEP total beam current versus time (top) and wire position readings versus time (bottom).

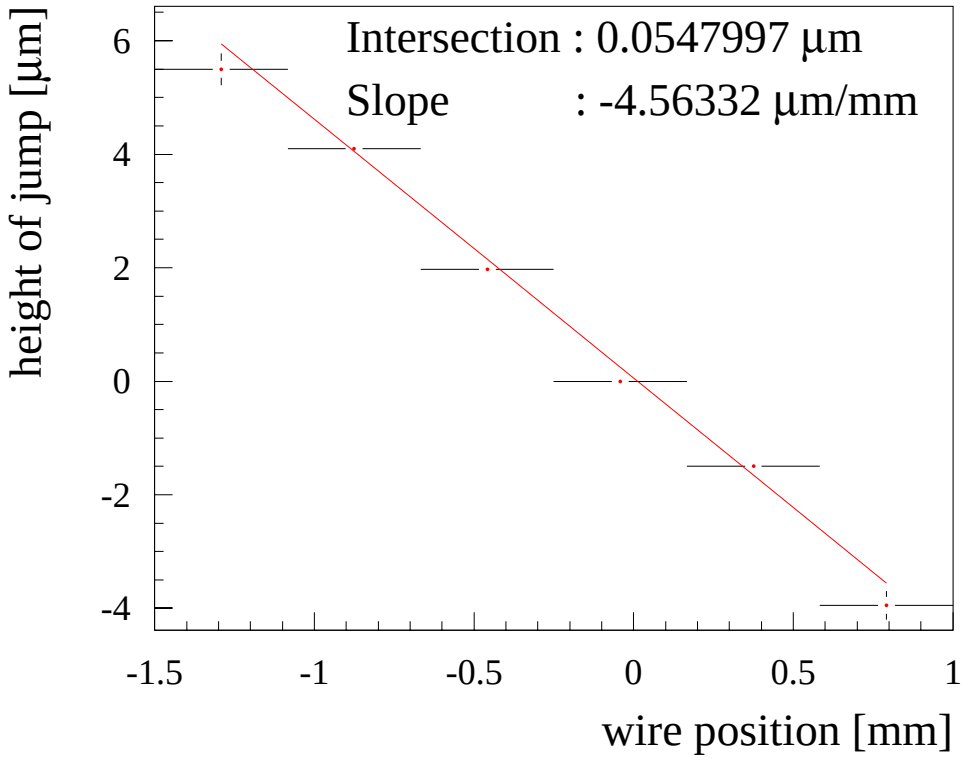

Figure 5.28: Correlation between the height of the jump in the WPS signal occurring during a beam dump (y-axis) and the position of the wire (x-axis). This plot contains data from all 18 sensors over five days.

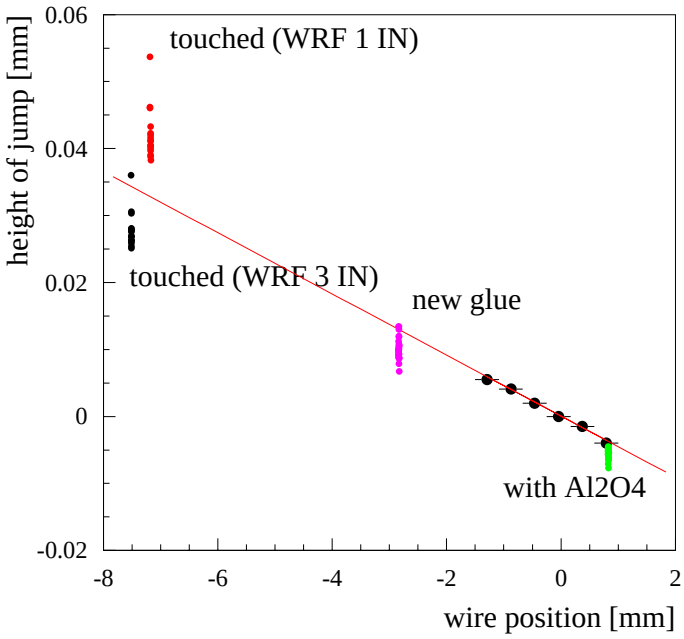

Figure 5.29: The height of the jumps plotted against the position of the wire for sensors which received special treatment plotted on top of Fig. 5.28. The data labeled “touched” were taken by a sensor while the wire was touching the frame of the sensor head and thus the wire was stationary. The data “new glue” were taken by a sensor, on which the glue was changed. The data “with Al2O4” were taken by a sensor on which the mount was changed.

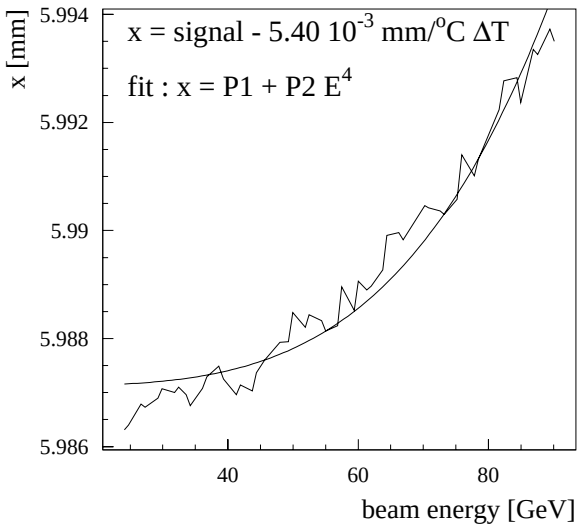

Figure 5.30: Normalised WPS signal against beam energy.

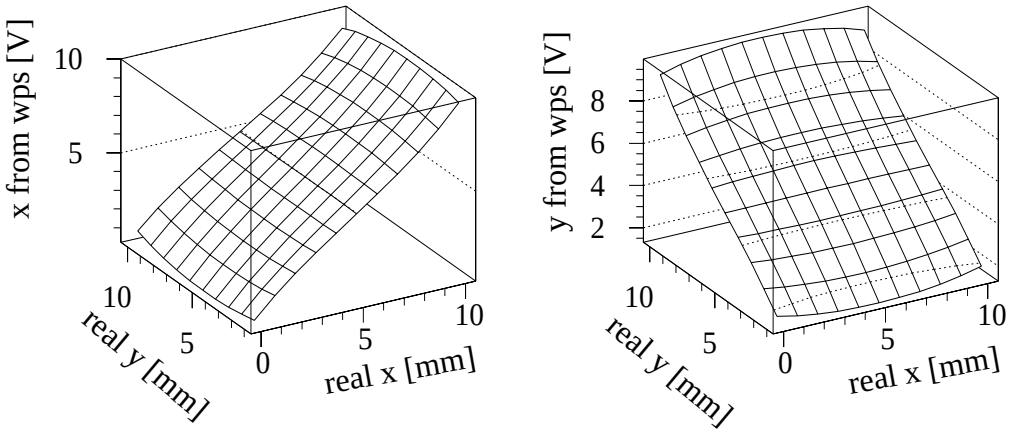

Figure 5.31: Response of the wire sensor in x (left plot) and y (right plot) plotted against x- and y- position of the wire.

run, where no shielding was applied. It was considered that the behaviour of the sensors might

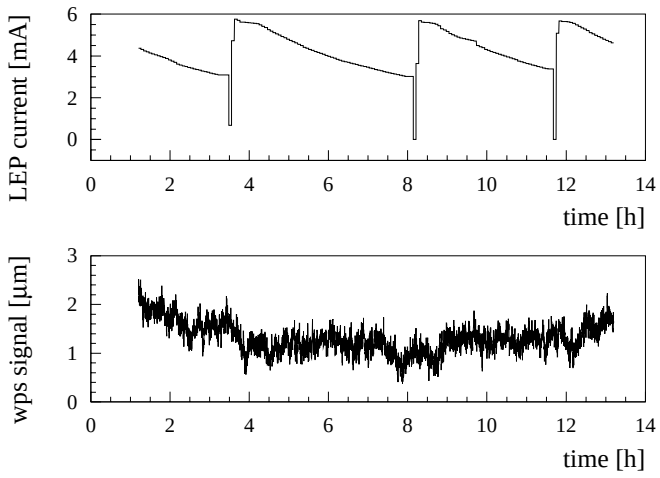

Figure 5.32: Top: LEP beam current over 12 hours. Bottom: Signal of a well shielded sensor over the same period of time.

be improved by collecting the free charges with electrodes made from copper sheet mounted at the openings of the sensor head. Fig. 5.34 shows the position of these bias plates on the sensor head. Such a solution was attempted with a DC voltage applied to the electrodes and the alignment wire. However this did not alleviate the undesirable correlation of the sensor readings with the LEP current: In Fig. 5.35 the top plot shows the “jumps” before, the bottom plot after the bias voltage was applied. To test the effect of the air in the sensor, another type of sensor with a cross section as sketched in Fig. 5.36 was brought into the LEP tunnel. With this sensor connected to a vacuum pump, it is possible to measure the capacitance between two plates (electrode and target), with and without air between them. The jumps occurring during the beam dump are reduced by a

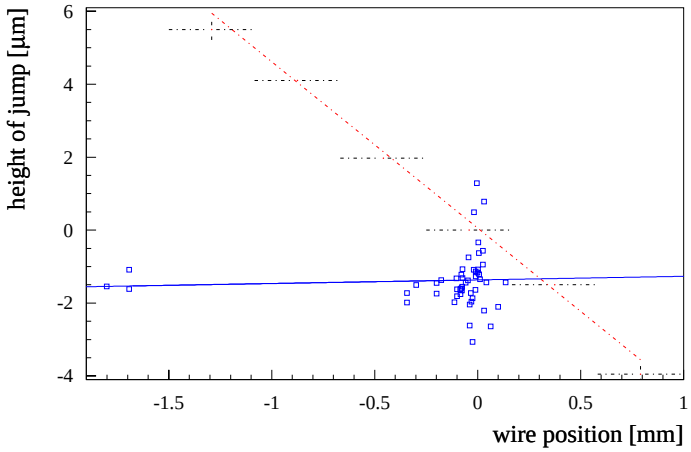

Figure 5.33: Height of the jumps against the position of the wire after the sensors were shielded plotted on top of Fig. 5.28.

factor of 7 when the sensor is put under vacuum, as can be seen in Fig. 5.37, in which the signal of the sensor is plotted versus time. The bars in the top part of the plot indicate when LEP was operating and the arrows above the plot indicate when the sensor was evacuated.
The size of the signal while the sensor is under vacuum is similar to the situation where LEP is running and there is air between the electrodes. Changes in the signal can only be explained by variations of the dielectric properties of the medium between the plates.

Explanation of the systematic effect on the WPS

The correlation between the size of the instantaneous position changes and the position of the wire indicates that the explanation must be related to the sensor head. A direct influence (such as an attraction of the wire) from the magnets can be excluded, as the magnets are not turned off immediately after a beam dump and the "jumps" occured as well with a fixed wire.

The synchrotron light coming from the beams ionises the air surrounding and within the sensor head. This leads to the creation of free charges. Furthermore the N_2 and O_2 molecules are split (see Sec. 2.3.2). This results in a decrease of the dielectric constant ϵ_r ($= 1 + \delta, \delta = 5.94\ 10^{-4}$ for dry air), like observed in Fig. 5.37. One can write an equation for the signal P of the sensor, where x is the distance, C the capacitance between sensor and target and S the surface of the electrodes:

$$P \propto C = \frac{\epsilon_o \epsilon_r S}{x} = \frac{\epsilon_o S}{x} + \delta \frac{\epsilon_o S}{x} . \tag{5.18}$$

While the sensor is under vacuum or LEP is running, the second term in Eq. 5.18 is zero respectively close to zero (δ=0).

The effect of the synchrotron light on the dielectric constant of air could be estimated by calculating the ratio between the signal from the sensor, with and without air inside it, according to Eq. 5.18:

$$P_{vac} \propto \frac{\epsilon_o S}{x} , \tag{5.19}$$

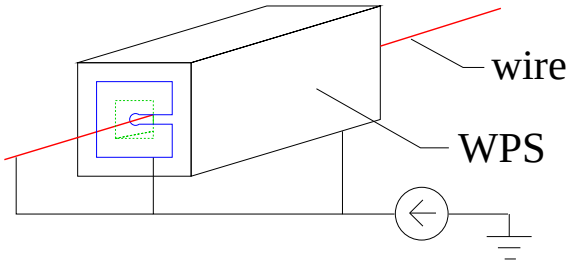

Figure 5.34: Top: Modification done on one sensor to suppress the undesired fast position changes.

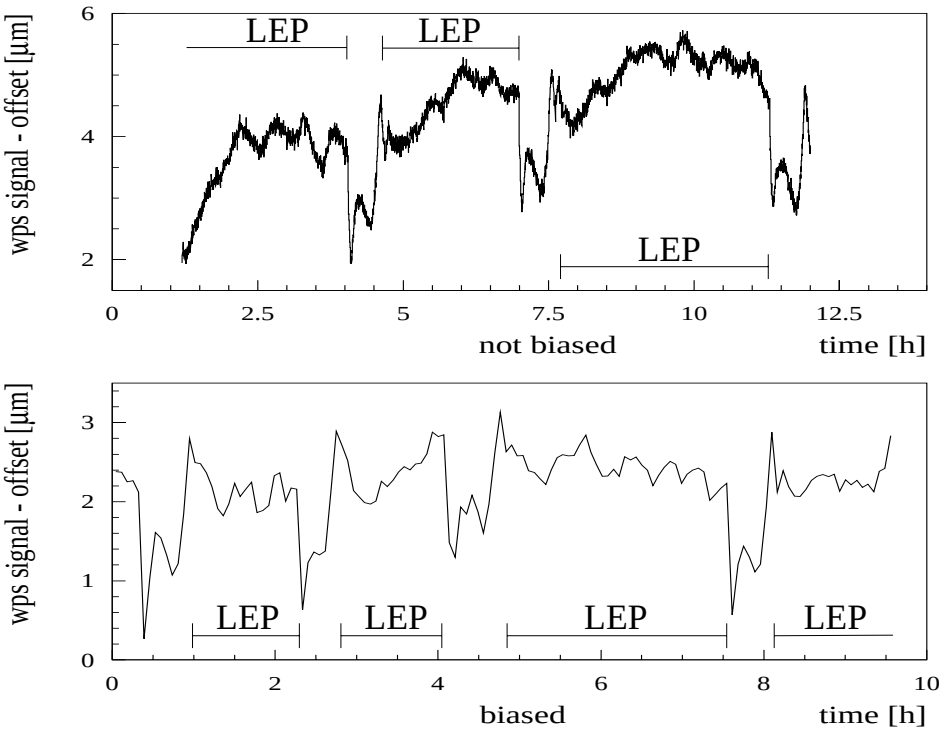

Figure 5.35: Signal from the WPS with (bottom) and without (top) the copper plates.

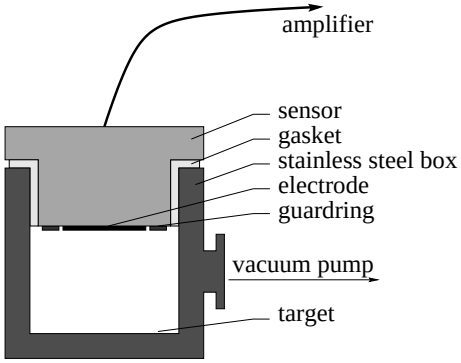

Figure 5.36: Cross section of a capacitive distance measuring sensor.

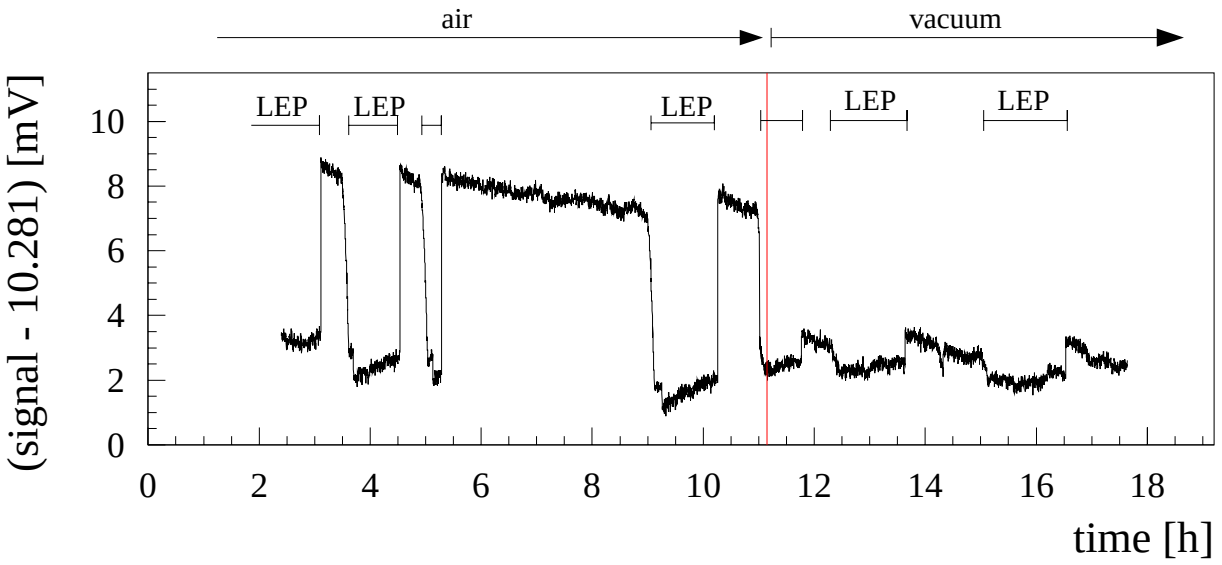

Figure 5.37: The signal from the sensor (inversely proportional to the distance), after offset subtraction, against time.

$$P_{air} \propto \frac{\epsilon_o S}{x} + \delta_{air}\frac{\epsilon_o S}{x} . \tag{5.20}$$

Thus:

$$\frac{P_{air}}{P_{vac}} = n_{air} = 1 + \delta_{air} . \tag{5.21}$$

According to Fig. 5.37 this would lead to a value for δ in air of 4.86×10^{-4}, which is to be compared with a value of 5.94×10^{-4} from the literature [18]. During LEP operation and with an air filled sensor a δ of -9.72×10^{-5} results.
The literature and the measured value for δ_{air} differ by $18\,\%$. This is considered as a good result for the simple setup. During LEP operation and with air in the sensor, a small difference from the vacuum condition is still observed ($\delta = -9.72 \times 10^{-5}$), indicating additional unexplained effects influencing the measurement.

Eq. 5.18 could be used for parametrising the observed change of the wire position signal. To measure the wire position (see Fig.5.38) the measured capacitance between wire and each electrode are subtracted. The electric field lines are symmetrical when the wire is in the centre (Fig. 5.38 a). The WPS signal can be written as follows:

$$P \propto \frac{1}{C_1} - \frac{1}{C_2} = \frac{x}{\epsilon\epsilon_r S} = \frac{x}{\epsilon S}\left(\frac{1}{1+\delta}\right) = \frac{x}{\epsilon S} - \delta\frac{x}{\epsilon S} + O(\delta^2) , \tag{5.22}$$

where C_i is the capacitance between the wire and the ith electrode and x the position of the wire with respect to the centre of the sensor.
The second term in this parametrisation explains the linear correlation between jump height and wire position plotted in Fig. 5.28. While LEP is running, this term is almost zero ($\delta \approx 0$) and the size of the jump during the beam dump is proportional to x.

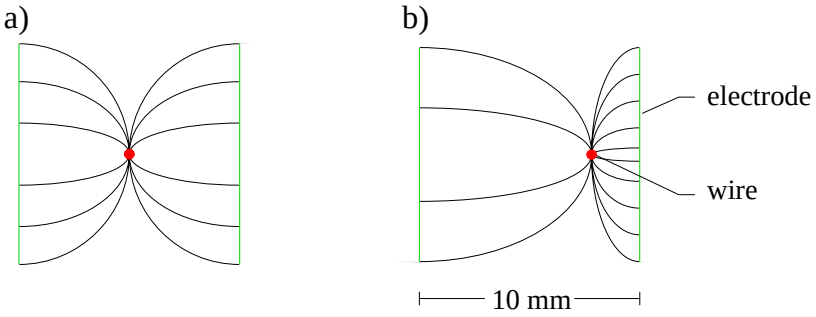

Figure 5.38: Electric field inside the sensor for a centred wire (left) and an off-centre wire (right).

The asymmetry of a factor of 10 between the radiation dose in the horizontal plane inside and outside the LEP ring (Fig. 2.11) was not correlated with bigger effects on the sensors on one side. This could be explained by a fast diffusion of the produced ions or saturation. This agrees with the fact that the revolution frequency of $11\,\mathrm{kHz}$, which is the fundamental frequency of photon production, was not observed in the fast Fourier transformation of the WPS signal.

It is not clear how the low ion pair concentration rate of $4.8 \times 10^{-10}\,\mathrm{s}^{-1}$ (Sec. 2.3.3) could affect the dielectric properties of the air so severely:

The dielectric property of a material is a macroscopic effect arising either from orientation of molecules with a permanent dipole moment $\vec{p}$ (orientation polarisation) or creation of a dipole moment $\vec{p}$ by an electric field pulling the electrons and nucleus of a molecule in opposite directions. In both cases, the macroscopic polarisation $\vec{P}$ results from the differential dipole moment $d\vec{p}$ per volume dV:

$$\vec{P} = \frac{d\vec{p}}{dV} \,. \tag{5.23}$$

The polarisation $\vec{P}$ is correlated with the dielectric constant ϵ_r as follows:

$$\vec{P} = \frac{\epsilon_r - 1}{\epsilon_r}\, \epsilon_0\, \vec{E} \,, \tag{5.24}$$

where $\vec{E}$ is the applied electric field.
During LEP operation the dielectric constant of the air is reduced to approximately 1.0 and thus according to Eq. 5.24 the polarisation is also decreased.
According to Eq. 5.23 the polarisation per unit volume results from the integral or sum over all dipole moments in this volume. A significant decrease of this sum cannot be caused by a small fraction ($\approx 10^{-10}$) of the molecules losing their dipole moment.

An additional effect which changes the dielectric properties of the air is based on the fact that the free electrons have a drift velocity which is 10^3 times higher than that of the ions [17]. This results in a net current flowing between the electrodes in the sensor head which weakens the field and thus changes the measured capacitance.

Modifications for 2000

For next year it is foreseen to improve the shielding on those position sensors which still show jumps. Another idea is to flush the sensor head with Helium ($\epsilon_r = 1 + 6.6 \times 10^{-5}$ compared

with air $\epsilon_r = 1 + 5.9 \times 10^{-4}$).
A good solution would be to use the sensors under vacuum, however this solution is considered to be impractical for the spectrometer.

Chapter 6

Results

6.1 Implementation of the Wire Positioning System

The WPS signals were used to measure the movements of the BPM blocks with respect to each other. Only during one calibration run (19^{th} of September, fill 6371) were significant movements observed. The expansion ϵ and the horizontal movement x of the BPM perpendicular to the direction of beam propagation as function of time are shown in Fig. 6.2 and Fig. 6.3 respectively. The numbering convention of the BPMs is illustrated in Fig. 6.1. Unfortunately one of the two sensors attached to BPM 6 was not working during this period. In Fig. 6.4 the temperature T of the BPMs is shown as a function of time. Correlations between expansion, centre movements and temperature variation are not evident. The beam position measurement was corrected for these movements.

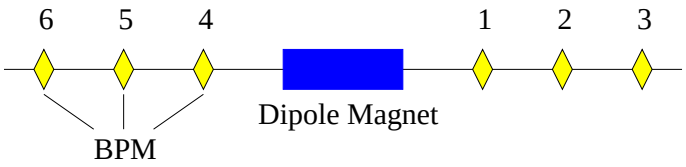

Figure 6.1: Sketch of the spectrometer setup illustrating the nomenclature of the beam position monitors.

6.2 Energy

Table 6.1 gives an overview about the energy calibrations performed by the spectrometer in the 1999 LEP run. Three steps were performed to prove the reliability of the spectrometer and estimate the beam energy:

- Observation of the correlation between the bending angle and the accelerating frequency (Eq. 6.3) to ensure the correct function of the BPMs.

- Comparison of the size of the energy shift during an acceleration in the range between 41 and 60 GeV given by the spectrometer and by the RDP method. This is an assessment test for the spectrometer.

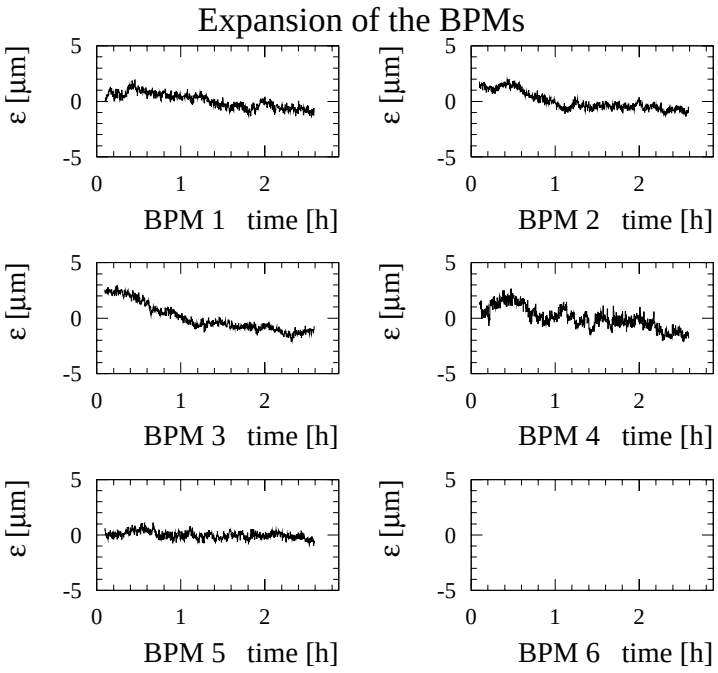

Figure 6.2: The expansion of the beam position monitors plotted versus time during a period of energy calibration.

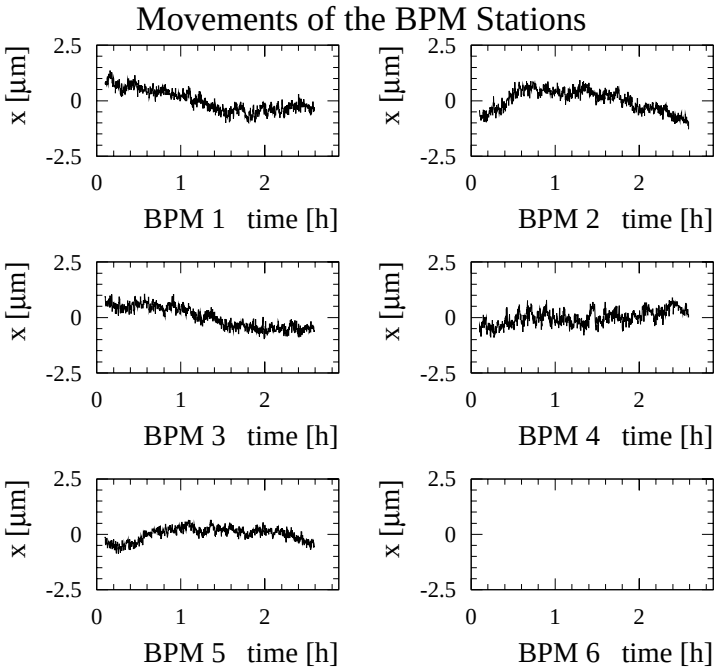

Figure 6.3: The centre position of the beam position monitors plotted versus time.

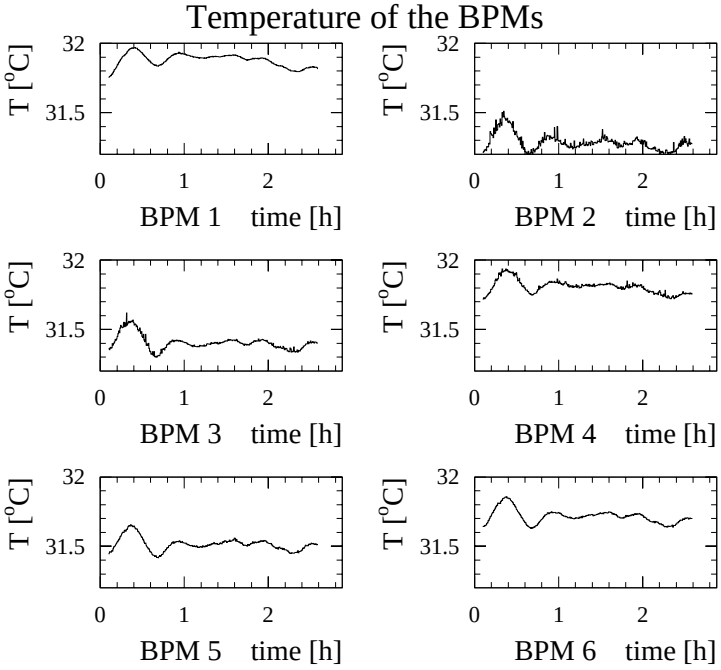

Figure 6.4: Temperature of the beam position monitors plotted versus time.

date	fill no.	calibrated energy [GeV]	high energy [GeV]
09/09/99	6302	41 45 50 55	
20/09/99	6371	41 45 50	
25/09/99	6397	45 50	70 92
27/09/99	6404	41 45 50 55	
29/09/99	6432	45 50	90
10/10/99	6509	41 50 60	92
27/10/99	6627	45	92

Table 6.1: Energy calibrations in the 1999 LEP run.

- Estimation of the energy in the range of $90\,\mathrm{GeV}$ with the spectrometer and with the energy model. This test is a cross check of the energy model (Sec. 3.2), which is the major task of the spectrometer.

In the following sections the results of these experiments are described.

6.2.1 Energy variations with a constant Bending Field

A test of spectrometer angle resolution and reproducibility is done by changing the beam energy in well known steps without changing the magnetic field of the analysing magnet. Variation of the accelerating frequency causes an energy, beam position and beam size change. The energy changes are given by:

$$\frac{\Delta E}{E} = -\frac{1}{\alpha_c}\,\frac{\Delta f_{RF}}{f_{RF}}\,. \tag{6.1}$$

According to Eq. A.6 for $\int_{MBI} Bds = const.$:

$$\frac{\Delta E}{E} = -\frac{\Delta\Theta}{\Theta}\,. \tag{6.2}$$

The relative angle change reads:

$$\frac{\Delta\Theta}{\Theta} = \frac{1}{\alpha_c}\,\frac{\Delta f_{RF}}{f_{RF}}\,. \tag{6.3}$$

With a nominal accelerating frequency of $f_0 = 352 \times 10^6$ Hz and a momentum compaction factor of 3.56×10^{-4} (1.56×10^{-4}) for the 60/60 (102/90) beam optics this results in a relative angle change of 0.8×10^{-5} / Hz (1.8×10^{-5} / Hz).

Fig. 6.5 shows the relative angle changes $\Delta\Theta/\Theta$ plotted versus the change in the RF accelerating frequency Δf_{RF} for the 102/90 optics. The deviations of the angle from the linear correlation illustrated in the bottom plot of Fig. 6.5 are well below 10^{-4}.

A problem of this procedure might be the observed effect of the RF frequency on the beam size (see Fig. 6.6), introducing an error on the beam position measurement (see Eq. 5.9). The beam size can be measured by beam size monitors (BEUV), which are CCD cameras observing the ultraviolet part of the synchrotron light emitted by the beam into a narrow cone. Thus an image of the beam cross section is taken. The light is observed in a bending magnet close to a point where the beta function β has a maximum, to detect the largest possible vertical beam dimension.

The observed beam size variations are of the order of $100\,\mu$m during the RF frequency variations. This change results according to Eq. 5.9 in an error on the beam angle determination of 6×10^{-6}, which is negligible.

6.2.2 Comparison of the Spectrometer and RDP Energy Measurements

As the error on the RDP measurement is negligible, this comparison allows an estimation of the accuracy of the energy determination by the spectrometer. During the 1999 LEP run, there were 11 particle accelerations in the energy range of 41 to $60\,\mathrm{GeV}$. In Fig. 6.7 (top) the difference between spectrometer and RDP energy measurement is plotted as function of energy. For both instruments the difference between successive values in energy is compared and the result is plotted at the higher energy value. The two measurements of the beam energy differences are independent of

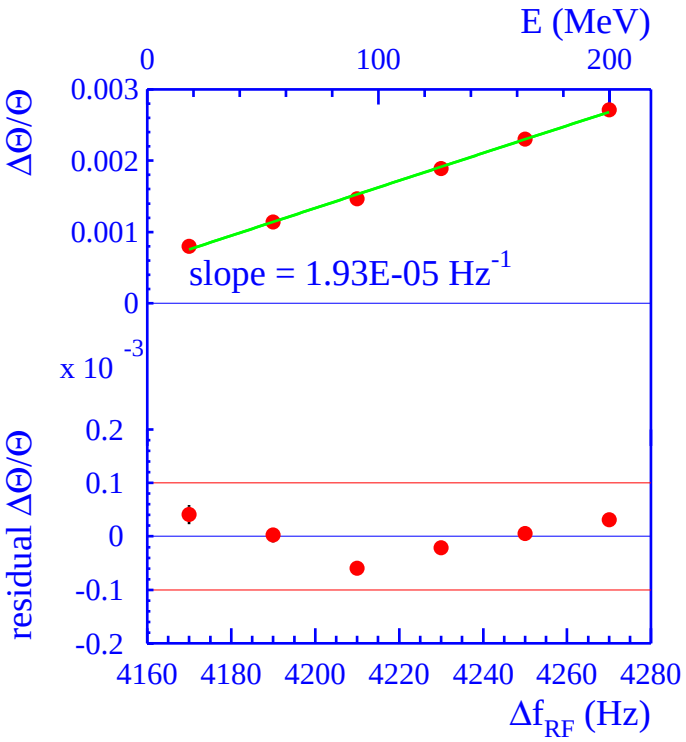

Figure 6.5: Top: Bending angle in the spectrometer magnet plotted against the RF accelerating cavity frequency which translates into an energy scale (Eq. 2.8). Bottom: Residual to the linear fit in the top plot.

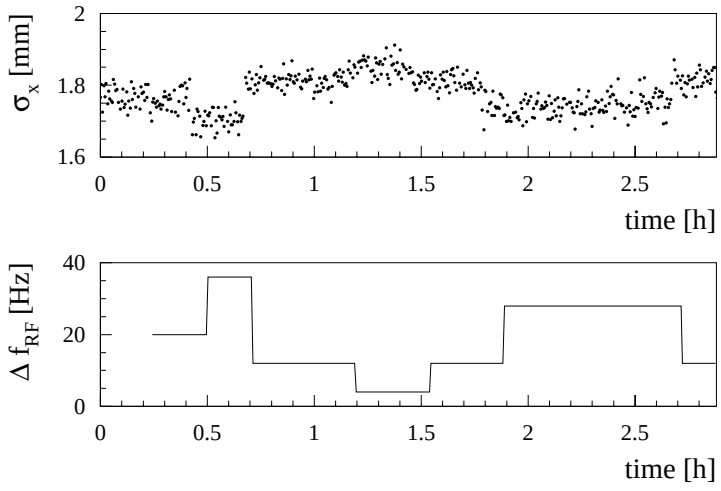

Figure 6.6: Correlation between the horizontal beam size (top plot) and the RF accelerating frequency (bottom plot).

each other. Since the error on the beam energy estimation is only $2\,\text{MeV}$ the variations in Fig. 6.7 (top) are dominated by the errors originating from the spectrometer. The distribution (see Fig. 6.7, bottom) represents the comparison of both methods at all beam energies.

Drawing conclusions from this distribution neglects the scaling of the spectrometer errors with energy. These errors are estimated to be small compared with the total width of the distribution. The mean value is $2.5 \pm 2.4\,\text{MeV}$. This indicates that the energy difference measurements of both methods show no systematic deviation to an accuracy of $2.4\,\text{MeV}$.

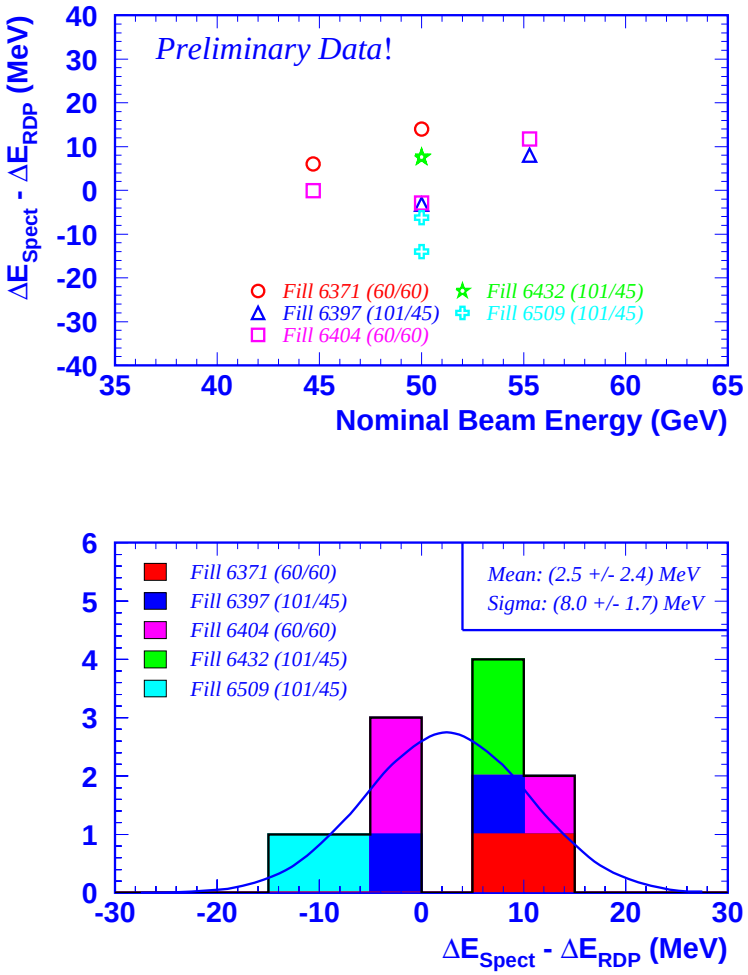

Figure 6.7: Top: Residual between the energy change from 41 GeV measured by the RDP and by the spectrometer plotted against target energy. Bottom: Histogram of this residual.

The spread of $8.0\,\text{MeV}$ has to be compared with the statistical error of $4.3\,\text{MeV}$ expected in this energy range from the error analysis of Sec. 6.3.

6.2.3 Comparison of the Spectrometer and the NMR Model Energy Measurements

In Fig. 6.8 the difference between the beam energy increase estimation by the NMR model and the spectrometer is plotted for three measurements versus energy. The result of the energy difference is plotted at the higher beam energy value. The mean value of the difference of the two methods is 0.3 ± 11 MeV indicating that the modulus of the difference of systematic errors originating from both methods is smaller than 11 MeV. The scatter of the measurements is 14.7 ± 6.0 MeV. The variations of these measurements will be discussed in the next section.

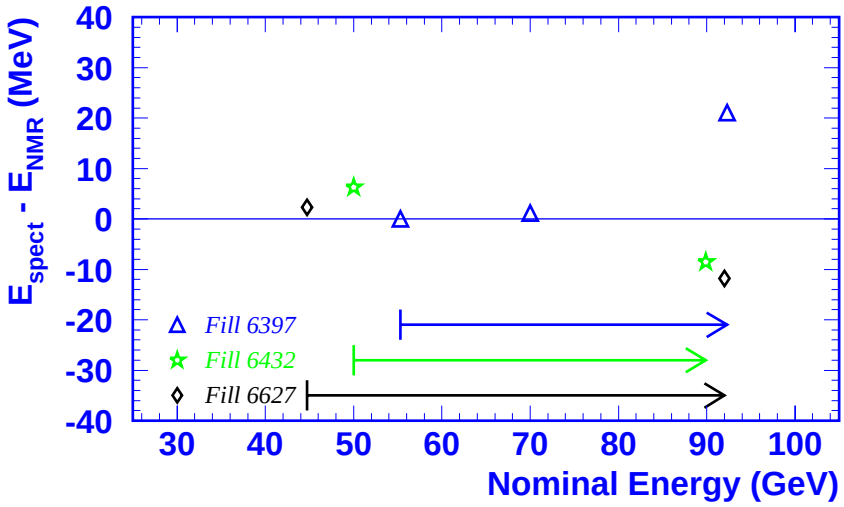

Figure 6.8: Difference between the estimation of the mean energy by the spectrometer and by the NMR model for three accelerations to high energies.

6.3 Error Estimate for the Spectrometer Energy Measurement

An error estimation for the spectrometer is vital to distinguish between expected statistical fluctuations and systematic effects. Furthermore the source of a potential deviation between the energy model prediction and the spectrometer energy estimate has to be identified as being either in the measurement techniques or the LEP energy model.

6.3.1 Statistical Error on the Energy Measurement

The local beam energy can be derived from Eq. A.6:

$$E_{beam} = cq \frac{\int_{MBI} B(s)ds}{\Theta} . \tag{6.4}$$

In the following the superscript h or l indicate if the variable was measured at high energies ($\approx 100\,\text{GeV}$) or low energies (41–$60\,\text{GeV}$).
The spectrometer determines the energy E^h_{beam}:

$$E^h_{beam} = \frac{b^h}{b^l}\,\frac{\Theta^l}{\Theta^h}\,E^l_{beam}\,, \tag{6.5}$$

where $b = \int B(s)ds$.
The ratio of the bending angles Θ^l/Θ^h is measured with the BPMs, the energy E^l is estimated employing the RDP and the ratio of the bending fields b^h/b^l is derived from the NMR probes inside the analysing magnet (see Sec. 5.1.1). As all these variables are measured with different independent devices, their errors are uncorrelated and the error propagation formula reads:

$$\frac{\Delta E^h_{beam}}{E^h_{beam}} = \sqrt{\left(\frac{\Delta\frac{\Theta^l}{\Theta^h}}{\frac{\Theta^l}{\Theta^h}}\right)^2 + \left(\frac{\Delta\frac{b^h}{b^l}}{\frac{b^h}{b^l}}\right)^2 + \left(\frac{\Delta E^l_{beam}}{E^l_{beam}}\right)^2}\,. \tag{6.6}$$

As sketched in Fig. 6.9, the deflection angle Θ can be split up into the two angles ($\alpha\,;\,\beta$) on either

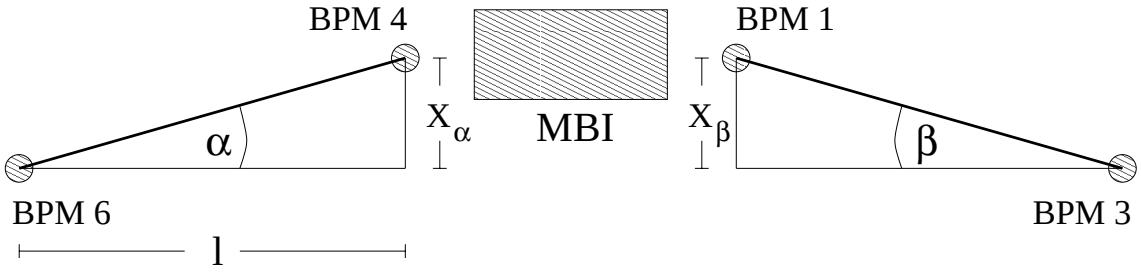

Figure 6.9: Sketch of the principle of angle estimation.

side of the magnet. Those angles depend on the x_α, x_β and the constant distance between the pickups l:

$$\Theta = \alpha + \beta = \frac{x_\alpha}{l} + \frac{x_\beta}{l} \tag{6.7}$$

$$\Rightarrow \frac{\Theta^h}{\Theta^l} = \frac{x^h_\alpha + x^h_\beta}{x^l_\alpha + x^l_\beta}\,. \tag{6.8}$$

As it is not known to what extend the errors on the measurements of the beam positions are correlated, the two extreme cases of no correlation and 100% correlation were analysed. It is believed, that the correlation is small, as the BPMs are mounted on individual limestone blocks and thus should be independent of each other. Eq. 6.8 results in the following error on the ratio of the angles:

- Assuming that the errors are uncorrelated:

$$\left(\frac{\Delta\frac{\Theta^h}{\Theta^l}}{\frac{\Theta^h}{\Theta^l}}\right)^2_{uncorr} = \left(\frac{\Delta x^h_\alpha}{x^h_\alpha}\right)^2 + \left(\frac{\Delta x^h_\beta}{x^h_\beta}\right)^2 + \left(\frac{\Delta x^l_\alpha}{x^l_\alpha}\right)^2 + \left(\frac{\Delta x^l_\beta}{x^l_\beta}\right)^2\,. \tag{6.9}$$

- Assuming that the errors are 100% correlated:

$$\left(\frac{\Delta\frac{\Theta^h}{\Theta^l}}{\frac{\Theta^h}{\Theta^l}}\right)_{corr} = \left|\frac{\Delta x^h_\alpha}{x^h_\alpha}\right| + \left|\frac{\Delta x^h_\beta}{x^h_\beta}\right| + \left|\frac{\Delta x^l_\alpha}{x^l_\alpha}\right| + \left|\frac{\Delta x^l_\beta}{x^l_\beta}\right| . \tag{6.10}$$

As the errors on the beam position measurements do not scale with energy ($\Delta x^h = \Delta x^l$) and can be assumed to be the same for both sides ($\Delta x_\alpha = \Delta x_\beta$) the following simplification can be made:

$$\left(\frac{\Delta\frac{\Theta^h}{\Theta^l}}{\frac{\Theta^h}{\Theta^l}}\right)_{uncorr} = 2\,\frac{\Delta x_\alpha}{x_\alpha} , \tag{6.11}$$

respectively:

$$\left(\frac{\Delta\frac{\Theta^h}{\Theta^l}}{\frac{\Theta^h}{\Theta^l}}\right)_{corr} = 4\,\frac{\Delta x_\alpha}{x_\alpha} . \tag{6.12}$$

The error on the angle can be reduced to an error on x_α. x_α consists of three contributions: The reading of two BPMs x_{BPM_i} and a nominal part ($x_n = 15\,\text{mm}$). The latter take into account the alignment of the pickup blocks along the nominal orbit; the error on x_n can be neglected as it is shown in the next paragraph:

$$x_\alpha = x_n + x_{BPM_4} - x_{BPM_6} \tag{6.13}$$

$$\Rightarrow \quad (\Delta x_\alpha)_{uncorr} = \sqrt{2}\,\Delta x_{BPM} \tag{6.14}$$

$$and \quad (\Delta x_\alpha)_{corr} = 2\,\Delta x_{BPM} . \tag{6.15}$$

Thus Eq. 6.11 can be written as follows:

$$\left(\frac{\Delta\frac{\Theta^h}{\Theta^l}}{\frac{\Theta^h}{\Theta^l}}\right)_{uncorr} = 2\sqrt{2}\,\frac{\Delta x_{BPM}}{x_\alpha} , \tag{6.16}$$

respectively:

$$\left(\frac{\Delta\frac{\Theta^h}{\Theta^l}}{\frac{\Theta^h}{\Theta^l}}\right)_{corr} = 8\,\frac{\Delta x_{BPM}}{x_\alpha} . \tag{6.17}$$

As $x_\alpha \approx x_n = 15\,\text{mm}$ and $\Delta x_{BPM} = 200\,nm$ (see Sec. 5.2) a relative error on the bending angle ratio of 3.8×10^{-5} results for the case of uncorrelated BPM errors. For correlated BPM errors the error on the angle ratio is 1.1×10^{-4}.

The relative error on the integrated field is known from the mapping campaign (Sec. 5.1.1):

$$\frac{\left(\Delta\frac{\left(\int Bds\right)^h}{\left(\int Bds\right)^l}\right)}{\left(\frac{\left(\int Bds\right)^h}{\left(\int Bds\right)^l}\right)} = 3 \times 10^{-5} . \tag{6.18}$$

The error on the low energy (41 – $60\,\text{GeV}$) consists of the error on the RDP method ($\Delta E^l_{beam}/E^l_{beam} = 3 \times 10^{-5}$) and the error on the RF model, which correlates the mean beam energy measurement of the RDP with the local beam energy at the spectrometer. The error on the latter is $3\,\text{MeV}$ at $50\,\text{GeV}$ and $5.5\,\text{MeV}$ at $100\,\text{GeV}$. Both errors are uncorrelated.

E_{beam}	50 GeV		100 GeV	
	correlated BPM readings	uncorrelated	correlated BPM readings	uncorrelated
RDP	1.5 MeV		3.0 MeV	
RF model	3.0 MeV		5.5 MeV	
$\int B\,ds$	1.5 MeV		3.0 MeV	
Θ	5.5 MeV	1.9 MeV	11 MeV	3.8 MeV
total	**6.7 MeV**	**4.3 MeV**	**13 MeV**	**7.9 MeV**

Table 6.2: Errors contributing to the final overall error on the energy determination with the spectrometer at two different energies.

All errors are summarised in Table 6.2 for the beam energies of 50 and 100 GeV. The total error is calculated according to Eq. 6.6.

Systematic Error on the Angle Estimate

The absolute angle measurement in the spectrometer has the following systematic errors:

- The centres of the elliptical apertures of the BPMs are aligned accurate to $\Delta x_n = 250\,\mu$m in the plane perpendicular to the direction of beam propagation.
- The Position of the BPMs along the direction of beam propagation is only accurate within $\Delta l = 200\,\mu$m.
- The electronics may have an offset corresponding to $\Delta x_{BPM} = 200\,\mu$m.

The given values are worst case assumptions.
According to Eq. 6.8 and Eq. 6.14 the angle is calculated as follows:

$$\Theta = \frac{x_n + x_{BPM_4} - x_{BPM_6}}{l} + \frac{x_n + x_{BPM_1} - x_{BPM_3}}{l}\,. \tag{6.19}$$

Assuming equal errors on the BPM readings x_{BPM_i} and a $100\,\%$ correlation of the errors (worst case estimate), the formula for the evolution of the errors reads:

$$\delta\Theta = 4\,\left|\frac{\Delta x_{BPM}}{l}\right| + 2\,\left|\frac{\Delta x_n}{l}\right| + \left|\Theta\frac{\Delta l}{l}\right|\,. \tag{6.20}$$

This systematic error $\delta\Theta$ affects the angle measurement at high energy in the same way as at low energy:

$$\left(\frac{E^h}{E^l}\right)^{spectro} = \frac{b^h}{b^l}\,\frac{\Theta^l + \delta\Theta}{\Theta^h + \delta\Theta}\,. \tag{6.21}$$

The ratio of the energies can be expanded in a Taylor series about small $\delta\Theta$:

$$\left(\frac{E^h}{E^l}\right)^{spectro.} = \frac{b^h}{b^l}\frac{\Theta^l}{\Theta^h} + \frac{b^h}{b^l}\frac{\Theta^h - \Theta^l}{\Theta^h}\frac{\delta\Theta}{\Theta^h} + O\left((\delta\Theta)^2\right)\,. \tag{6.22}$$

The error on the energy is therefore given by:

$$\frac{\Delta\frac{E^h}{E^l}}{\frac{E^h}{E^l}} = \frac{\Theta^h - \Theta^l}{\Theta^h}\frac{\delta\Theta}{\Theta^l} \,. \tag{6.23}$$

Including Eq. 6.20 results in:

$$\frac{\Delta\frac{E^h}{E^l}}{\frac{E^h}{E^l}} = \frac{\Theta^h - \Theta^l}{\Theta^h}\left(4\frac{\Delta x_{BPM}}{l\Theta} + 2\frac{\Delta x_n}{l\Theta} + \frac{\Delta l}{l}\right) \,. \tag{6.24}$$

The term in front of the bracket is less than 4×10^{-4} for the relevant energy measurements. Thus according to the values listed above, Eq. 6.24 provides an error on the energy ratio of 1.7×10^{-5}. Presuming that the errors provided by the alignment group are correct, there is a negligible effect of these systematics on the beam energy measurement.

According to Eq. A.6 the energy loss in the analysing magnet affects the bending angle, to first order, as follows:

$$\delta\Theta \;=\; \frac{1}{2}\,\frac{\Delta E}{E}\Theta \,, \tag{6.25}$$

where $\Delta E > 0$.
These errors affect the energy ratio:

$$\frac{E^h}{E^l} \;=\; \frac{b^h}{b^l}\,\frac{\Theta^l + \delta\Theta^l}{\Theta^h + \delta\Theta^h} \,. \tag{6.26}$$

Expansion in a Taylor series about small $\delta\Theta$ results in:

$$\frac{E^h}{E^l} = \frac{b^h}{b^l}\,\frac{\Theta^l}{\Theta^h} \;-\; \frac{b^h}{b^l}\,\frac{\Theta^l}{\Theta^h}\,\frac{\delta\Theta^h}{\Theta^h} \;+\; \frac{b^h}{b^l}\,\frac{\delta\Theta^l}{\Theta^h} \;+\; O\left(\delta\Theta^2\right) \tag{6.27}$$

The error on the energy is therefore given by:

$$\frac{\frac{E^h}{E^l} \;-\; \frac{b^h}{b^l}\,\frac{\Theta^l}{\Theta^h}}{\frac{b^h}{b^l}\,\frac{\Theta^l}{\Theta^h}} \;=\; \frac{\delta\Theta^l}{\Theta^l} \;-\; \frac{\delta\Theta^h}{\Theta^h} \tag{6.28}$$

With the results of Appendix B and Eq. 6.25, the relative error on the angle $\delta\Theta$ is 2.2×10^{-6} for the low energy and 1.8×10^{-5} for the high energy. Thus the ratio of the energies has a relative systematic error of 1.6×10^{-5}. Eq. 6.28 is less than zero and thus the energy increase is overestimated.

Discussion of expected and measured Errors

For the low energy the measured error of (8.0 ± 1.7) MeV is larger than the expected value of 4.3 MeV. This is an indication that there may be systematic errors which are not yet understood. For the high energy the measured error of (14.7 ± 6.0) MeV agrees with the expected error of 7.9 MeV.

Chapter 7

Conclusion

The LEP energy spectrometer installation was finished in the operation period of 1999. The relative accuracy of the integral magnetic field of the spectrometer magnet was determined to 3×10^{-5}.

The intrinsic systematic errors of the beam position measurement were studied. The relative gains of the beam position monitors were determined with a specially developed beam based method accurate to 10^{-4}. The absolute gains of the orbit monitors were established using two different methods based on the theoretical knowledge of the dispersion function and on the standard orbit monitor calibration.

The wire position monitor system was commissioned and the data used in the spectrometer energy determination. The cause of an important systematic error of the sensors was identified by making several dedicated experiments. The error was found to be caused by the synchrotron light altering the dielectric properties of the air inside the sensor. The observed effects can be described by modelling the electric field configuration inside the sensor, coupled with the properties of the synchrotron light. The problem was suppressed by shielding the wire position sensor body with lead. The reproducibility of the sensor was determined to be $530\,nm$ using a laser interferometer.

The accuracy of the beam energy determination with the spectrometer was compared with the independent method of resonant depolarisation. The difference between both methods is $(2.5 \pm 2.4)\,MeV$ with a statistical difference of $8\,MeV$. The spectrometer energy estimate at high energies was compared with the NMR based technique. The difference is $0.3\,MeV$ with an error of $11\,MeV$. The spread of the measurement is $15\,MeV$. The experimental statistical errors agree with the expectation from the separately measured errors of the constituents and input values.

Chapter 8

Outlook

To improve the performance of the beam position monitors, one or more BPMs will be made movable horizontally with a range of between 1 and $2\,mm$. Based on Eq. 5.9 and the reading of the wire position system it may be possible to reduce the error on the absolute gain and determine the geometric centre of the BPMs. This adjustment would reduce the error caused by the nonlinear response of the BPMs (see Sec. 5.2.2).

Furthermore the BPM electronics and data acquisition chain will be tested for stability during the shut down with a pulse generator simulating the beam signal of the BPM electrodes.

The positions of the adjacent quadrupole magnets are the references for the alignment of the spectrometer components, whereas the LEP beam orbit monitors are the reference for positioning the beam. Therefore it is planned to perform beam based alignment [42], to find the centre of the standard LEP beam orbit monitors with respect to the magnetic centre of the adjacent quadrupole magnets.

Some of the WPS were not sufficiently shielded with lead in the 1999 LEP operation period. This will be improved for the next run.

The spectrometer provides the opportunity to test the RF model predictions (see Fig. 2.1) on the difference in energy of the e^- and e^+ beams. This is possible as the spectrometer can observe either e^- or e^+ and measure their local energies separately.

Operation in the LEP 2000 operation period

The procedure planned for the year 2000 operation is described in the flow diagram in Fig. 8.1. It is planned to position the beam in the centre of all BPMs before and after a ramp. This will allow a zero measurement for the BPMs which means that the reproducibility rather than the accuracy of the BPM reading would be relevant for the error estimation (see Sec. 2.2.2). This aim will be achieved using the following tools:

- The standard LEP corrector magnets can move the beam orthogonal to its direction of propagation.
- With knowledge of α_c a known change in the bending angle could be introduced by changing the RF accelerating frequency (Eq: 6.2).

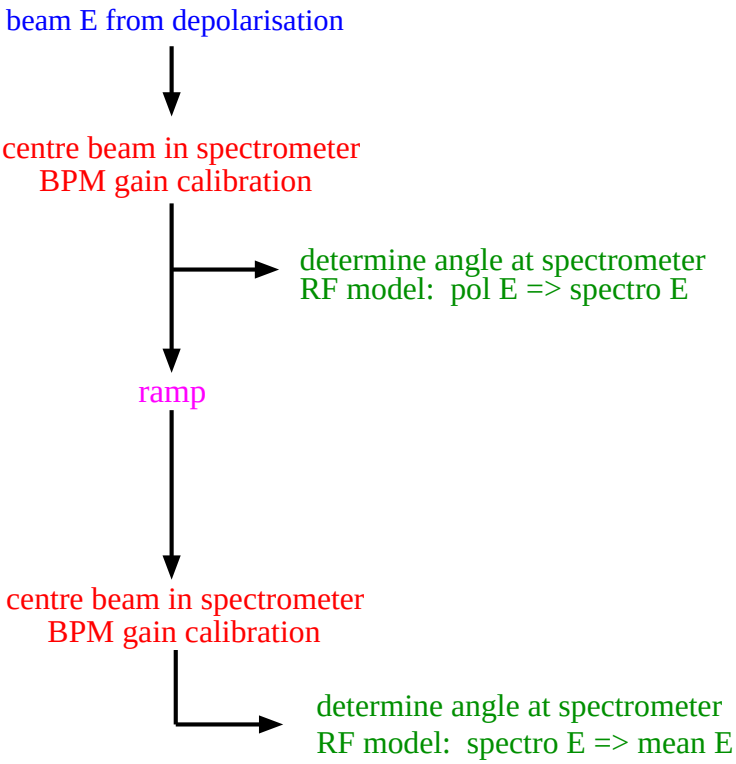

Figure 8.1: Procedure of operating the spectrometer in 2000.

An algorithm which automatically calculates the necessary changes to move the beam back to the centre of the BPMs is planned for the operation period in the year 2000.
Such an algorithm would calculate and execute the necessary RF frequency shift to readjust the bending angle and then readjust the transverse position with the correctors. This would be done in several iterations.
A possible problem of this procedure might be the influence of the RF frequency on the beam size and thus on the BPM reading as described in Chapter 6.

Appendix A

Beam Deflection in the Analysing Magnet

A charge q travelling with speed $\vec{v}$ and the momentum $\vec{p}$ in a magnetic field ($\vec{B}$) encounters a deflection which is quantified by Lorentz Law:

$$\frac{d\vec{p}}{dt} \;=\; \vec{F}_L \;=\; q\,\left(\vec{v}\;\times\vec{B}\right)\;. \tag{A.1}$$

The velocity of the particles circulating in LEP differs from the speed of light in the 8th digit. So we can assume $ds/dt \;=\; \|\vec{v}\| = c$. Furthermore the trajectories ($\uparrow\uparrow \vec{e}_s$) are perpendicular to $\vec{B}$ ($\uparrow\uparrow \vec{e}_y$), where ($\vec{e}_x$, $\vec{e}_y$, $\vec{e}_s$) is a right handed coordinate system and these vectors have unit length:

$$d\vec{p} \;=\; q\;B\;ds\;\vec{e}_x\;. \tag{A.2}$$

For the case of the spectrometer it is necessary to integrate Eq. A.2 over the length of the magnet l, where $\vec{p}$ is the momentum of the particles before and $\vec{p}\prime$ after they have crossed the magnet:

$$\|\vec{p}-\vec{p}\prime\| \;=\; q\;\int_0^l B(s)\;ds\;. \tag{A.3}$$

The bending angle Θ is the angle between $\vec{p}$ and $\vec{p}\prime$. Using the cosine formula, one can derive the following equation:

$$\cos\Theta \;=\; \frac{1}{2pp\prime}\;\left(p^2\;+\;p\prime^2\;-\;\left(\;q\;\int_0^l B(s)\;ds\;\right)^2\right)\;. \tag{A.4}$$

The good approximation $p \simeq \frac{E}{c}$ and $p\prime = \frac{E-\Delta E}{c}$ is used:

$$\cos\Theta \;=\; \frac{1}{2}\left(\frac{E}{E-\Delta E}+1-\frac{\Delta E}{E}-\frac{c^2q^2}{E(E-\Delta E)}\;\left(\int_0^l B(s)\;ds\right)^2\right)\;. \tag{A.5}$$

Working on the assumption that the energy loss in the dipole is small compared to the beam energy ($\Delta E/E \;=\; 3.55\;\times\;10^{-5} \ll 1$ for $100\,GeV$) (see. Appendix B) and that the angle is small ($\Theta \;=\; 3.75\,mrad$) one can simplify Eq. A.5, by means of a Taylor series expansion with respect to $\Delta E/E$ about zero up to the first order:

$$\Theta \;=\; \frac{cq}{E}\;\int_0^l\;B(s)ds\;+\;\frac{1}{2}\;\frac{\Delta E}{E}\;\left(\frac{cq}{E}\;\int_0^l\;B(s)ds\right)\;+\;O\left(\left(\frac{\Delta E}{E}\right)^2\right)\;. \tag{A.6}$$

The impact of the term linear in the energy loss ΔE is discussed in Sec. 6.3.1.

Appendix B

Energy loss in the Analysing Magnet

As the charged particles get deflected in the analysing magnet, they emit synchrotron light and thus lose energy. The energy loss can be calculated as follows: The power of the synchrotron light P_{syn} is quantified by the following equation [6]:

$$P_{syn} = \frac{e^2 c}{6\pi\epsilon_o} \frac{1}{(m_e c^2)^4} \frac{E^4}{\rho^2} , \tag{B.1}$$

where e is the electron charge magnitude, c the speed of light, m_e the electron mass and E the energy of the particle. Eq. B.1 integrated over time leads to the following equation, assuming a constant bending radius ρ:

$$\Delta E_{syn} = \int_0^{\frac{l}{c}} P_{syn}\, dt = \frac{e^2 l}{6\pi\epsilon_o} \frac{1}{(m_e c^2)^4} \frac{E^4}{\rho^2} . \tag{B.2}$$

The bending radius is correlated with the bending angle Θ (angle between incoming and outgoing trajectory) via the length of the magnet l as follows:

$$\sin\frac{\theta}{2} = \frac{l}{2\rho} . \tag{B.3}$$

Thus Eq. B.2 results in:

$$\Delta E_{syn} = \frac{2}{3} \frac{e^2}{l\pi\epsilon_o} \frac{E^4}{(m_e c^2)^4} \sin^2\left(\frac{\Theta}{2}\right) . \tag{B.4}$$

The magnet has a length of $5.57\,m$ and a nominal bending angle of $3.75\,mrad$. An energy loss of $3.55\,MeV$ results for energies of $100\,GeV$, and $222\,keV$ for energies of $50\,GeV$. Thus Eq. B.2 results in:

$$\Delta E_{syn} = \frac{2}{3} \frac{e^2}{l\pi\epsilon_o} \frac{E^4}{(m_e c^2)^4} \sin^2\left(\frac{\Theta}{2}\right) . \tag{B.5}$$

The magnet has a length of $5.57\,m$ and a nominal bending angle of $3.75\,mrad$. An energy loss of $3.55\,MeV$ results for energies of $100\,GeV$, and $222\,keV$ for energies of $50\,GeV$.

Appendix C

The Effect of Dispersion on the Energy Measurement

An assumption used implicitly in the principle of the spectrometer is that the centre of charge of the beam, which is the observed quantity, behaves like a particle with the mean local energy. According to Eq. 2.9 and Eq. 2.2 the energy is linearly distributed along the transverse width of the beam:

$$\Delta x \;=\; D(s)\,\frac{\Delta E}{E_0}\,, \tag{C.1}$$

where E_0 is the mean particle energy and $\Delta E = E - E_0$, s is the curvilinear coordinate and $D(S)$ the dispersion function introduced in Sec. 2.1.
The transverse particle distribution $f(x)$ of the beam and the energy distribution $g(E)$ are to a good approximation Gaussian. f and g are normalised.
The mean transverse particle position $\langle x\rangle$ before passing the magnet is the ideal trajectory:

$$\langle x\rangle_{before} \;=\; \int_{-\infty}^{\infty} x\; f(x)\; dx \;=\; 0\,. \tag{C.2}$$

According to Eq. C.1 the mean position after having crossed the magnet is:

$$\langle x\rangle_{after} \;=\; \int_{-\infty}^{\infty} \left(x + D(s)\frac{\Delta E}{E_0}\right)\; f(x)\; dx\,. \tag{C.3}$$

Using Eq. C.1 and the fact that f is normalised, Eq. C.3 can be simplified:

$$\langle x\rangle_{after} \;=\; \frac{D(s)}{E_0}\;\int_{-\infty}^{\infty} E\; f(x)\; dx \;-\; D(s)\,. \tag{C.4}$$

As f and g are unique functions the following equation is valid [43]:

$$g(E) \;=\; \left|\frac{dx}{dE}\right|\; f(x)\,. \tag{C.5}$$

Therefore the integral in Eq. C.4 is equal to the mean energy E_0 and thus:

$$\langle x\rangle_{after} \;=\; 0\,. \tag{C.6}$$

This means that the dispersion does not affect the centre of charge.

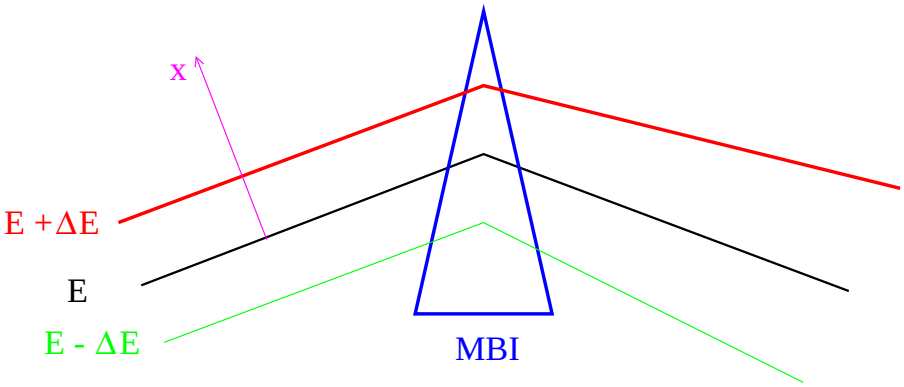

Figure C.1: Three particles on the trajectories corresponding to their energies.

Appendix D

Correlation between Angle & NMR reading

To calculate the mean energy ($\langle E_{beam}\rangle = \langle B_f/\Theta_f\rangle$) at the spectrometer, the mean angle $\langle\Theta_f\rangle$ and the mean magnetic field value $\langle B_f\rangle$ are used:

$$\langle\frac{B_f}{\Theta_f}\rangle = \langle B_f\rangle \cdot \langle\frac{1}{\Theta_f}\rangle \,. \tag{D.1}$$

A condition for this expansion is that B_f and $\frac{1}{\Theta}$ are independent [43]:

$$f(\frac{1}{\Theta_f}, B_f) = g(\frac{1}{\Theta_f}) \cdot h(B_f) \,. \tag{D.2}$$

where $f,\ g,\ h$ are distributions of probability.
An indication for the extent of correlation is the so-called covariance:

$$cov(\frac{1}{\Theta_f}, B_f) \ = \ (\frac{1}{\Theta_f} \ - \ \langle\frac{1}{\Theta_f}\rangle) \cdot (B_f \ - \ \langle B_f\rangle) \,. \tag{D.3}$$

In the case that a special value of $1/\Theta_f$ within the distribution does not convey any information on the value of B_f, the value of the covariance is zero. This corresponds to independent variables.

Fig. D.1 shows the value of the covariance over the period of eight hours. The mean value is constructed by taking the average over the last 80 readings, corresponding to $2\,min\ 18\,sec$ ("sliding window"). Neither the angle nor the $\vec{B}$-field changed in this period of time. The top plot in Fig D.1 illustrates that there is no time dependence, the bottom plot shows the distribution over the same time. As the mean value is small compared with the sigma, the correlation is given by the width (5.7×10^{-3}). The deviations of the Θ and B_{NMR} from their mean value are due to statistical fluctuations.

Therefore the two observables $1/\Theta_f$ and B_f are independent in the sense of Eq. D.3 and hence Eq. D.1 can be applied.

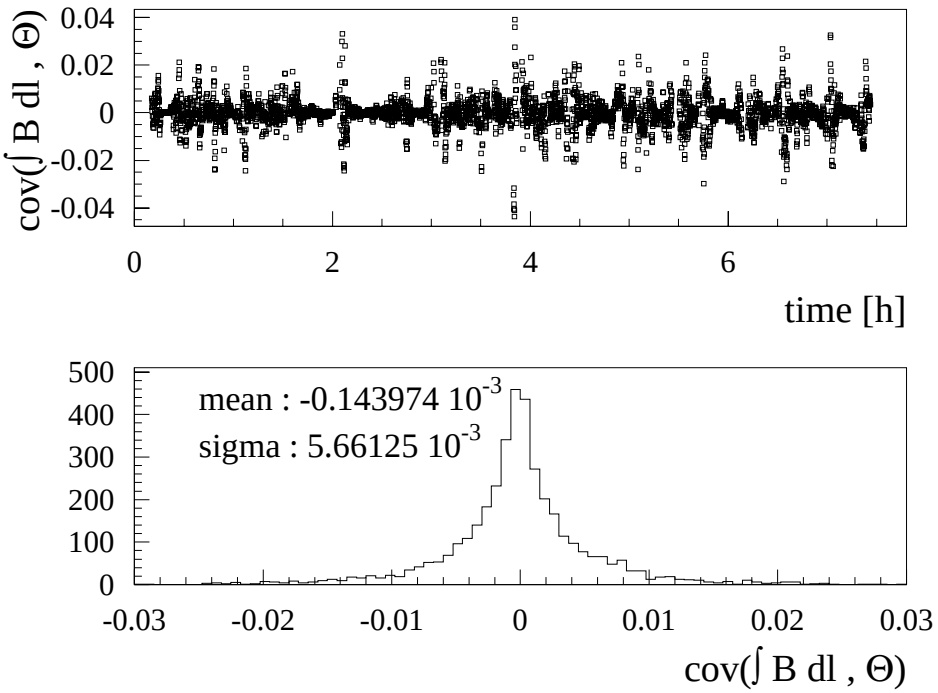

Figure D.1: Top: Covariance plotted against time. Bottom: Distribution of the covariance.

Appendix E

Field inside the Wire Position Sensor

In this appendix the electrostatic problem of a grounded wire between two metallic electrodes at the same potential will be studied.
To calculate the electric potential and field, the following assumptions are made:

- The size of the electrodes is infinite.
- The conductive wire (equipotential surface) is substituted by a line charge (charge per unit length q).

The errors due to these assumptions will be estimated. The potential Φ, which fulfils the Dirichlet condition for the surface of the electrodes $\Phi_{|electrodes} = const.$ can be constructed by an arrangement of image line charges. In an analogous way to Chapter 4.2.2 the image line charges have to be placed according to an algorithm:
The first generation of image charges ($-q$) can be found at the position of the real line charge mirrored with respect to the electrodes. The second generation image line charges (q) are at the position of the first generation charges mirrored with respect to the electrodes as sketched in Fig. E.1. This results in an infinite number of image charges. Knowing the charge distribution one can calculate the electric potential Φ:

$$\begin{aligned}\Phi(x,y) &= \frac{q}{2\pi\epsilon_o}\left(\frac{1}{\sqrt{x^2+(y-y_2)^2}} + \sum_{n=1}^{\infty}\frac{-1}{\sqrt{x^2+(y-2nd+y_2)^2}}\right.\\ &+ \sum_{n=1}^{\infty}\frac{-1}{\sqrt{x^2+(y+2(n-1)d+y_2)^2}} + \sum_{n=1}^{\infty}\frac{1}{\sqrt{x^2+(y-2nd-y_2)^2}}\\ &+ \left.\sum_{n=1}^{\infty}\frac{1}{\sqrt{x^2+(y+2nd-y_2)^2}}\right) .\end{aligned} \tag{E.1}$$

As the wire is a conducting cylinder, the electric potential is constant on its surface. A measure of how well the estimated potential fulfils this condition is the maximum relative potential difference on a cylinder with the wire radius ϵ centred at the position of the line charge $(0, y_2)$. This maximum difference is found between the two opposite sides of the wire which are facing the electrodes:

$$\frac{|\Phi(x,y)_{|x=0,\ y=y_2+\epsilon} - \Phi(x,y)_{|x=0,\ y=y_2-\epsilon}|}{\Phi(x,y)_{|x=0,\ y=y_2+\epsilon}} . \tag{E.2}$$

For the arrangement of the WPS ($d = 10\,mm$, $\epsilon = 0.2\,mm$) and a wire centred within $\pm 1\,mm$ the value of Eq. E.2 is below 3×10^{-3}.

With $\vec{E} = -\nabla\Phi$ the two relevant components of the electric field can be calculated.

The component parallel to the plates:

$$\begin{aligned} E_x &= \frac{-q}{2\pi\epsilon_o}\left(\frac{-x}{(x^2+(y-y_2)^2)^{\frac{3}{2}}} + \sum_{n=1}^{\infty}\frac{x}{(x^2+(y-2nd+y_2)^2)^{\frac{3}{2}}}\right. \\ &+ \sum_{n=1}^{\infty}\frac{x}{(x^2+(y+2(n-1)d+y_2)^2)^{\frac{3}{2}}} + \sum_{n=1}^{\infty}\frac{-x}{(x^2+(y-2nd-y_2)^2)^{\frac{3}{2}}} \\ &+ \left.\sum_{n=1}^{\infty}\frac{-x}{(x^2+(y+2nd-y_2)^2)^{\frac{3}{2}}}\right)\,, \end{aligned} \tag{E.3}$$

and the component perpendicular to the plates:

$$\begin{aligned} E_y &= \frac{-q}{2\pi\epsilon_o}\left(\frac{y_2-y}{(x^2+(y-y_2)^2)^{\frac{3}{2}}} + \sum_{n=1}^{\infty}\frac{y-2nd+y_2}{(x^2+(y-2nd+y_2)^2)^{\frac{3}{2}}}\right. \\ &+ \sum_{n=1}^{\infty}\frac{y+2(n-1)d+y_2}{(x^2+(y+2(n-1)d+y_2)^2)^{\frac{3}{2}}} + \sum_{n=1}^{\infty}\frac{-y+2nd+y_2}{(x^2+(y-2nd-y_2)^2)^{\frac{3}{2}}} \\ &+ \left.\sum_{n=1}^{\infty}\frac{-y-2nd+y_2}{(x^2+(y+2nd-y_2)^2)^{\frac{3}{2}}}\right)\,. \end{aligned} \tag{E.4}$$

The electric potential and field according to Eq. E.1 respectively Eq. E.3 and Eq. E.4 is plotted in Fig. E.2, where only the part between the electrodes is physical. An area around the charge is cut out to avoid infinite potential and field.

The WPS measure the capacitance C_i (per length) between plate i and wire. From these the wire position signal P is calculated:

$$P \propto \frac{1}{C_1} - \frac{1}{C_2} = \frac{U_1}{Q_1} - \frac{U_2}{Q_2}\,. \tag{E.5}$$

Q_i is the charge per unit length introduced on the plate i and U_i is the voltage between this plate and the wire.

$$P \propto \frac{1}{Q_1} - \frac{1}{Q_2}\,. \tag{E.6}$$

Eq. E.5 and Eq. E.6 are only equivalent, if the U_i are

- equal for both plates ($U = U_i$) and
- independent of wire movements y_2.

For the WPS the voltage U is given by the applied voltage source and thus both conditions are fulfilled.
For the approximated potential $\Phi(x, y)$ it can be shown that the first constraint is fulfilled, but the second one is not. To estimate the error, the correlation between U and y_2 is plotted in Fig. E.3, where $y_2 = 5$ corresponds to a centred wire. U is defined as the difference of the value for $\Phi(x, y)$ on the plate and at a point of the wire (ϵ, y_2). U is normalised for the potential difference U_0 between wire and electrodes for a centred wire. The two plots in Fig. E.3 differ in the range of the x axis. The voltage is constant within 4×10^{-3} if the wire position changes by $\pm 1\,mm$ with respect to the centre.

Q_i is proportional to the scalar product of the electric field $\vec{E}_{|plate} = (E_y)_{|plate}\,\vec{e}_y$ at the surface of the electrode and a unit vector $\vec{n}$ normal to the surface integrated over the length of the electrode [7]:

At the lower electrode:

$$\begin{aligned} Q_1 &= \epsilon_0 \int_{electrode\ 1} (E_y)_{|y=0}\,\vec{e}_y \cdot \vec{n}_1\,dx \\ &= \frac{-q}{2\pi}\left(\frac{2}{y_2} + \sum_{n=1}^{\infty}\frac{4}{y_2 - 2nd} + \sum_{n=1}^{\infty}\frac{2}{y_2 + 2(n-1)d} + \sum_{n=1}^{\infty}\frac{2}{y_2 + 2nd}\right), \end{aligned} \tag{E.7}$$

and at the upper electrode:

$$\begin{aligned} Q_2 &= \epsilon_0 \int_{electrode\ 2} (E_y)_{|y=d}\,\vec{e}_y \cdot \vec{n}_2\,dx \\ &= \frac{q}{2\pi}\left(\frac{2}{y_2 - d} + \sum_{n=1}^{\infty}\frac{2}{d - 2nd + y_2} + \sum_{n=1}^{\infty}\frac{4}{2nd - d + y_2}\right. \\ &+ \left.\sum_{n=1}^{\infty}\frac{2}{y_2 - d - 2nd}\right). \end{aligned} \tag{E.8}$$

Note that the orientation of the vectors $\vec{e}_y \uparrow\uparrow \vec{n}_1 \uparrow\downarrow \vec{n}_2$ introduces a sign change in the latter term.
The correlation between P and the position of the wire y_2 resulting from Eq. E.6, Eq. E.7 and Eq. E.8 is plotted in Fig. E.4 (top). The bottom plot shows the residual to a linear correlation. The effects of nonlinearities for a wire centred within $\pm 1\,mm$ are of the order of 3×10^{-2}. As the errors due to the assumptions were estimated to be small against this deviation, it is believed that the model is adequate.

Fig. E.5 shows the results of a measurement performed by the company Fogale, which provides the WPS sensors. The voltage given by the sensor was measured as a function of the wire position given by stepping motors. Qualitatively Fig. E.5 and Fig. E.4 agree with each other. Quantitative comparisons are not possible, as Fogale measured in steps of $1\,mm$ and thus provides only three "points" in the range for which the model is valid.

The test stand described in Sec. 5.3.2 was used to measure the response characteristics of one WPS sensor. The results are plotted in Fig. E.6. The nonlinearities were found to contribute only by a fraction of 4.6×10^{-3} to the position signal. This value has to be compared with the predictions from the model of 3×10^{-2}.

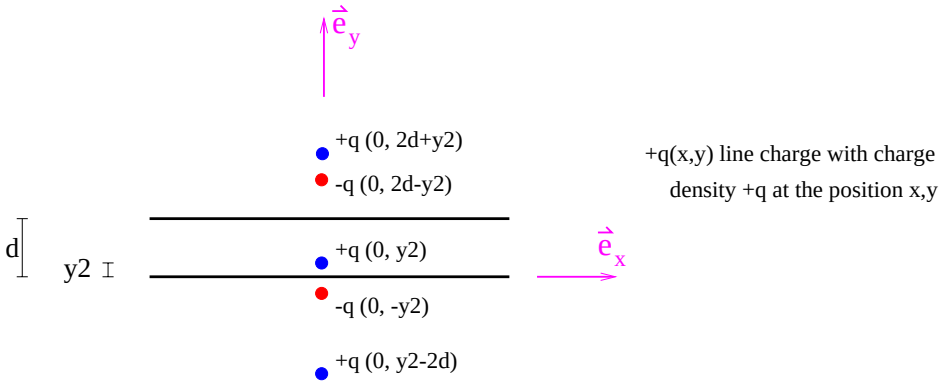

Figure E.1: Construction of image charge to derive the field inside the WPS.

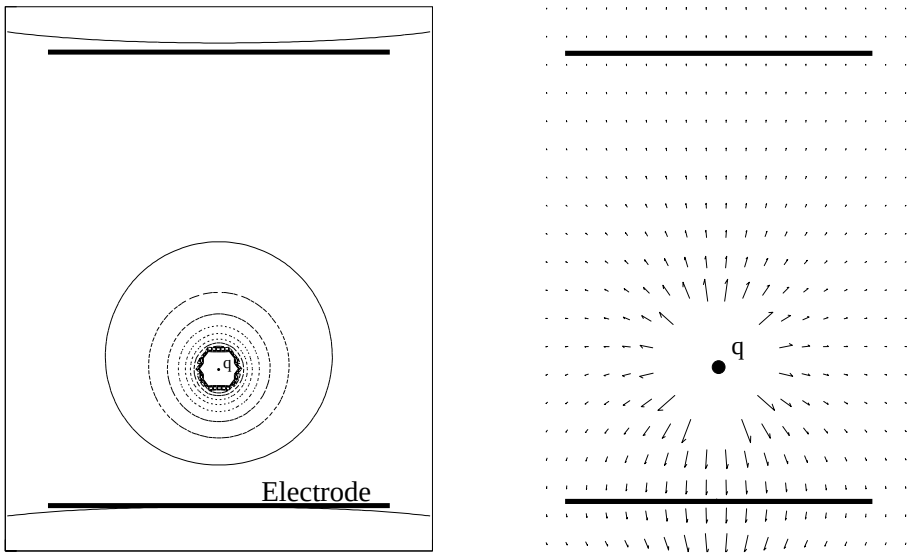

Figure E.2: Left: Electric potential in the WPS. The equipotential lines outside the electrodes are not real. Right: Electric field inside the WPS.

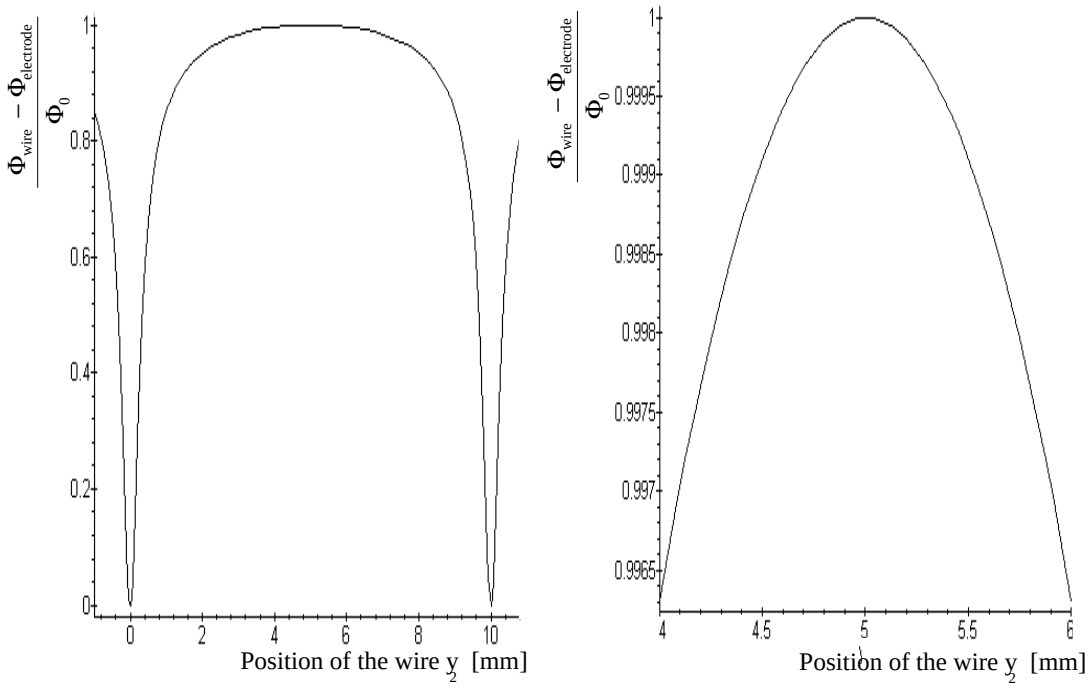

Figure E.3: Normalised voltage between wire and electrodes plotted against wire position in y_2. The two plots differ in the range of the x axis.

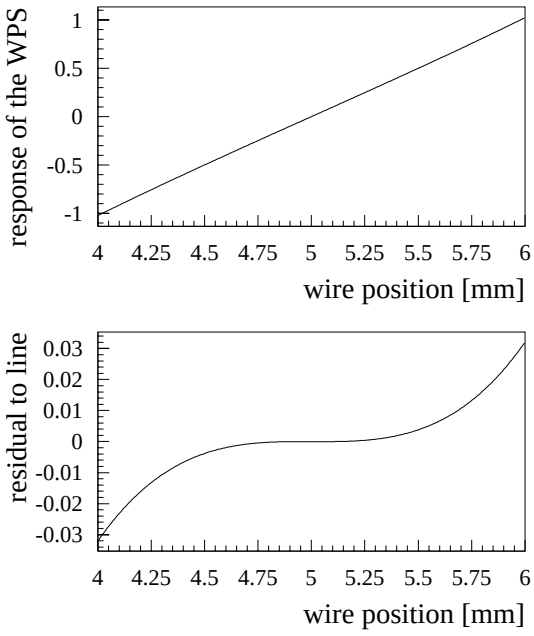

Figure E.4: Top: Predicted response of the wire position sensor versus position of the wire in y_2 as. Bottom: Residual to the linear correlation between response and wire position in y.

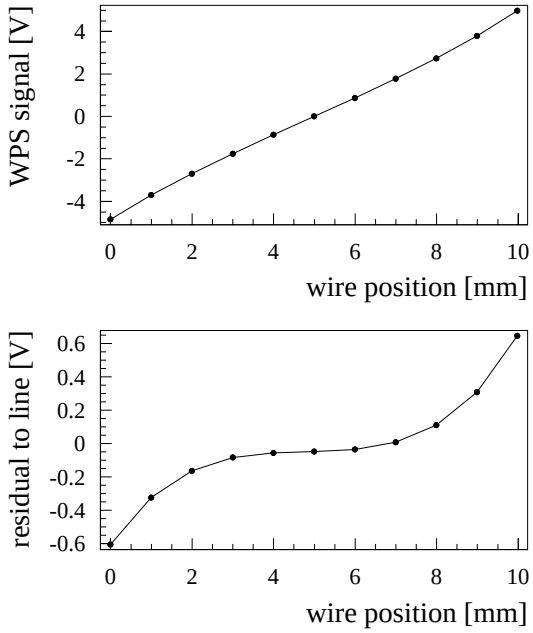

Figure E.5: Response of the wire position sensor versus position of the wire (top) measured by Fogale and the residual to a linear correlation (bottom).

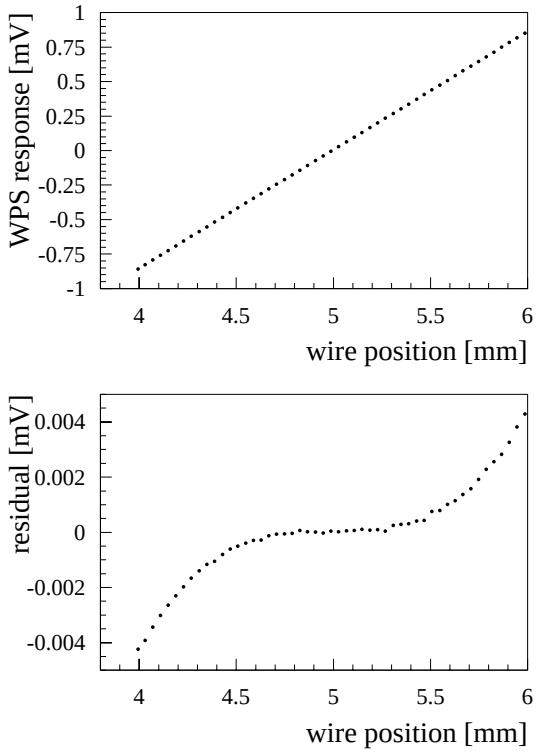

Figure E.6: Response of the WPS measured using a test stand.

Bibliography

[1] S.L. Glashow, Nucl. Phys. 22 (1961) 579; S. Weinberg, Phys. Rev. Lett. 19 (1967) 1264; A. Salam, in: N. Svartholm (Ed.), Elementary Particle Theory, Stockholm, Almquist and Wiksell, 1968, p.367.

[2] Aleph Collaborationm, CERN-PPE/97-164.

[3] Altarelli, G. et al., Workshop on Physics at LEP2, CERN 96-01 ,1996.

[4] LEP design report, CERN-LEP/84-01, June 1984.

[5] L.Arnaudon et al., Effects of terrestrial tides on the LEP beam energy, CERN SL/94-07 BI.

[6] H. Wiedemann, Particle Accelerator Physics I, ISBN 3-540-64671-X,1998.

[7] J. D. Jackson, Classical Electrodynamics, (Wiley, New York, 1962).

[8] H. H. Umstätter, Efficient computation of synchrotron radiation Spectrum, 1981.

[9] Particle Data Group, The European Physical Journal C, 1998.

[10] Documentation of available FORTRAN libraries at CERN: wwwinfo.cern.ch/asdoc/Welcome.html.

[11] O. Gröbner, Studies of Photon induced Desorption using the Synchrotron Radiation of DCI, CERN-ISR-VA/81-31.

[12] www.physics.nist.gov/PhysRefData/XrayMassCoef/cover.html

[13] K. Kleinknecht, Detektoren fuer Teilchenstrahlung.

[14] M. Hoefert et al., Combined influence of humidity and radiation in the LEP tunnel, CERN SL-95-08 (DI).

[15] T. Momose and H. Ishimaru, Radiation damage in Tristan vacuum systems, J. Vac. Sci. Technol. A9, 2149, 1991.

[16] W. Nelson, The Radiation Dose to the Coil Windings and the Production of Nitric Acid and Ozone from PEP Synchrotron Radiation, PEP-109, 1975.

[17] G. F. Knoll, Radiation Detection and Measurement, Second edition, 1989.

[18] Robert C. Weast, CRC Handbook of Chemistry and Physics.

[19] The LEP Energy Working Group, Calibration of centre-of-mass energies at LEP1 for precise measurements of Z properties, CERN-SL/98-012.

[20] M. Geitz, Investigation of Environmental Effects on the LEP Beam Energy, Diploma Thesis, RWTH Aachen, Germany (1996).

[21] M. Sassowsky, Magnetic field calculations for the LEP spectrometer project, SL-Note-99-011 MS.

[22] A. A. Sokolov et. al., On polarisation and spin effects in the theory of synchrotron radiation, Sov. Phys. Dokl., 8:1203, 1964.

[23] V. Bargmann et al., Precession of the polarization of particles moving in a Homogeneous Electromagnetic Field, Phys. Rev. Lett. 10 (1959).

[24] F. Sonnemann, Increase of Spin Polarisation for Energy Calibration at LEP, Diploma Thesis, RWTH Aachen, Germany (1998).

[25] A. A. Sokolov et al., Radiative Polarisation at Ultra-High Energies", Part. Acc. 1979, Vol. 9.

[26] Metrolab Instruments SA, 110 Ch. Du-Pont-Du-Centenaire CH-1228 Geneva (Switzerland).

[27] A.S. Müller, Precision Measurements of the LEP Beam Energy for the Determination of the *W* Boson Mass, to be published.

[28] Bergoz Instrumentation, www.bergoz.com.

[29] K. B. Unser, New Generation Electronics Applied to the Beam Position Monitors, 1996.

[30] C. Bovet et al., Solution d'un probleme électrostatique, MPS/DL Int.65-13, 1965.

[31] R. H. Miller et al., Nonintercepting emittance monitor, SLAC PUB 3186, 1983.

[32] J. Matheson, private conversation.

[33] H. Favre, Cours de mecanique, 1953.

[34] F. Becker, Conséquences des perturbations de la gravité sur l'alignement du CLIC, OPEN-99-244.

[35] C. Gerthsen et al., Physik, 16. edition, 1989.

[36] Keithley DVM 2002

[37] Opera 3D version 7.005, Vector Fields Limited, 24 Bankside, Kidlington, Oxford OX5 1JE, England.

[38] F. Roncarolo, Magnetic field measurements on MB/MBI dipole magnets, to be published.

[39] J. Matheson, Beam Size Effects in Beam Position Monitors for the LEP Spectrometer ,to be published.

[40] J. Borer et al., Algorithmes de Linearisation des Pick-ups.

[41] Hewlett Packard, Laser Measurement System Operator, Operation Manual.

[42] B. Dehning, Beam based Alignment at LEP, to be published.

[43] S. Brandt, Datenanalyse, (BI Wissenschaftsverlag, 1981).

Acknowledgements

I would like to thank Prof. Dr. Albrecht Böhm for his fruitful ideas and the support, which gave me the opportunity to do this diploma work in the encouraging environment of CERN.

Thanks to Prof. Dr. Joachim Mnich for his willingness to be the second proofreader of this thesis.

Dr. Bernd Dehning introduced me at CERN. I enjoyed working with him and felt well supervised and supported during my stay.

I express my apprechiation towards the engagement with which the company Fogale and especially Frédéric Ossart supported us concerning the investigation and tests on the wire position sensors.

Special thanks to Dr. John M. Matheson and Federico Roncarolo for friendly help in all day life's questions at CERN and successful team work.

Thanks to Denis Azzedine, Bruno Breavoine, Gian Paolo Ferri and Antonio Marin for the technical realisation of our ideas.

Thanks to the members of the LEP Energy Working Group for the opportunity of following and learning from their discussions.

I would also like to express my gratitude to the numereous people who aided in either practical work or fruitful discussions, especially Ralph W. Assmann, Mike Hildreth, Giuseppe Mugnai, Massimo Placidi, Eric Torrence, Jörg Wenninger.

Last but not least thanks go to my parents who have supported me throughout my studies.